

ABSTRACT

Title of dissertation: **INFERENCE OF MASS ANOMALIES
IN PLANETARY INTERIORS USING A
BAYESIAN GLOBAL GRAVITY FIELD
INVERSION**

Kristel Izquierdo
Doctor of Philosophy, 2021

Dissertation directed by: **Professor Laurent Montési
Department of Geology**

Knowledge about the interior density distribution of a planetary body can constrain geophysical processes and reveal information about the origin and evolution of the body. Properties of this interior distribution can be inferred by analyzing gravity acceleration data sampled by orbiting satellites. Usually, the gravity data is complemented with additional laser ranging or seismic data in order to reduce the range of possible density models of the interior. However, additional data might not be available and tight prior constraints on model parameters might not be justified. In this case, the flexibility of using non-informative priors and the ability to quantify the non-uniqueness of the gravity inversions are of even greater importance.

In this work, we present a gravity inversion algorithm, **THEBOOGIE**, that samples the posterior distribution of density in the interior of a planet or moon according to Bayes theorem, following a Metropolis-Hastings iterative algorithm. It uses non-informative priors on the number, location, shape and magnitude of density

anomalies. Different samples of the posterior show different density models of the interior consistent with the observed gravity data. Inversions of synthetic gravity data are ran using point masses, spherical caps and Voronoi regions (VRs) to parametrize density anomalies. TheBOOGIe is able to retrieve the lateral location of shallow density anomalies and the shape, depth and magnitude of a mid-mantle anomaly. The uncertainty of the model parameters increases with depth, as expected.

Bouguer gravity data of the Moon obtained by the GRAIL mission was inverted using a VR parametrization. Shallow anomalies related to the SPA basin, crustal dichotomy and near side basins were found in the correct latitude and longitude and a trade-off in their thickness and magnitude. Positive and negative density anomalies were found in the depth range 500-1141 km. The location of deep moonquakes do not have a clear relation to the location of these density anomalies.

INFERENCE OF MASS ANOMALIES IN PLANETARY
INTERIORS USING A BAYESIAN GLOBAL GRAVITY FIELD
INVERSION

by

Kristel Izquierdo

Dissertation submitted to the Faculty of the Graduate School of the
University of Maryland, College Park in partial fulfillment
of the requirements for the degree of
Doctor of Philosophy
2021

Advisory Committee:
Professor Laurent Montési, Chair/Advisor
Professor Vedran Lekić, Co-Advisor
Professor Michael N. Evans
Professor Nicholas C. Schmerr
Professor Maria Cameron

© Copyright by
Kristel Izquierdo
2021

Dedication

Spanish

Dedico esta tesis a mis padres, Armando Izquierdo and Meraris Gonzalez, quienes valoraron mi educación por encima de todo. Esta tesis es el producto de las oportunidades que tuve gracias a su visión y a su sacrificio.

Haber tenido acceso a una educación de calidad fue un privilegio y tengo presentes en mi mente y en mi corazón a todas las personas de Tabasco y de Mexico que injustamente no han tenido acceso a esa y otras oportunidades. Espero que en un futuro, esta injusta distribución de oportunidades cambie y que mas jóvenes tengan acceso a la educación y a la ciencia, independientemente de su género o estado socioeconómico.

English

I dedicate this dissertation to my parents, Armando Izquierdo and Meraris Gonzalez, who valued education above all things. This dissertation is a product of the opportunities I had access to because of my parent's vision and hard work. It is not, unfortunately, a product of the society I grew up in. I hope this changes for future generations. I hope more young men and women in Tabasco and Mexico have access to education and get exposed to science regardless of their gender or socio-economic background.

Acknowledgments

I owe my gratitude to all the people that have contributed to making my PhD a rewarding, unforgettable experience.

My advisors were always available to answer my many questions and concerns about my research projects and life in academia. I benefited a lot from our weekly meetings and possibly more from lunches at Looney's and Thanksgiving dinners.

My friends gifted me many exciting, fun memories I will cherish forever. Exploring San Francisco and New Orleans with my office mates after busy AGU days, especially bar hopping in Bourbon street; having innumerable hotpots, korean barbecues and dimsum with the international "mafia" and celebrating every little and big life event with my fellow latinxs (including I.H.O.P and friends).

Israel has systematically debated every doubt I had about myself over the last five years and has helped me stay grounded in my goal of being a planetary scientist. He has filled my life with support, love and adventures. Our years together had been the best years of my life.

My dogs of course played a very important role supporting my emotional well-being. Limon slept on my lap every single time I had to pull and all-nighter and Flor forced me to go on walks to keep me active even in busy days.

To you all you, thank you.

Table of Contents

Dedication	ii
Acknowledgements	iii
Table of Contents	iv
List of Tables	vii
List of Figures	viii
1 Introduction	1
1.1 Spherical harmonics and models of the topography and gravity of the Moon	2
1.1.1 Topography	3
1.1.2 Gravity	3
1.2 Interior structure of the Moon	4
1.2.1 Crustal features	5
1.2.2 Deep features	8
1.3 Density models of planetary bodies and parametrization choices	12
1.4 Bayesian inference and non-informative priors in gravity inversions	15
1.5 Monte Carlo sampling of a posterior probability distribution	17
1.6 Research goals	19
1.7 Outline of the thesis	19
2 A Bayesian approach to infer interior mass anomalies from the gravity data of celestial bodies	21
2.1 Abstract	21
2.2 Introduction	22
2.3 Inversion technique	24
2.3.1 Bayesian inference	24
2.3.2 Transdimensionality	25
2.3.3 Reversible jump Markov chain Monte Carlo algorithm (rjMCMC)	25
2.3.4 Hierarchical parameter	30
2.4 Validation	31
2.4.1 Point masses as the target mass distribution model	32

2.4.1.1	Fit to input gravity data	33
2.4.1.2	Fit to target density model	36
2.4.2	Spherical caps as the target density model	40
2.4.2.1	Fit to input gravity data	42
2.4.2.2	MCMC set up	44
2.4.2.3	Fit to target mass distribution	44
2.4.2.4	Uncertainty related to point mass parametrization	51
2.5	Discussion	52
2.6	Conclusion	53
3	Spherical caps as parametrization of density anomalies in global gravity inversions	55
3.1	Abstract	55
3.2	Introduction	56
3.3	Gravity inversion method	60
3.3.1	Gravity acceleration of a spherical cap	66
3.4	Validation	67
3.5	Discussion	79
3.6	Conclusion	80
4	Bayesian gravity inversion algorithm for inferring finite size density anomalies in planetary interiors	82
4.1	Abstract	82
4.2	Introduction	83
4.3	Discretization of the interior: Voronoi regions and tesseroïd grid	88
4.4	Selection criteria for density models. Posterior, likelihood and acceptance probabilities	90
4.5	Gravity inversion algorithm	93
4.6	Method validation	96
4.6.1	Target density model and input gravity acceleration data	97
4.6.2	Output density models	102
4.7	Discussion	116
4.8	Conclusions	119
5	Shallow and deep density anomalies of the Moon from a flexible inversion of GRAIL data	120
5.1	Abstract	120
5.2	Introduction	121
5.2.1	Lunar interior anomalies	124
5.2.2	Lunar evolution	127
5.3	Method	129
5.3.1	Parametrization of density anomalies and global grid	130
5.3.2	Prior constraints	131
5.3.3	Ensemble of density models	132
5.3.4	Input GRAIL gravity acceleration data	135

5.4	Results	136
5.4.1	Mean density anomalies and confidence	137
5.4.2	Correlation between density anomalies in the output models	143
5.4.3	Cluster analysis of density anomalies in the mean model	152
5.4.4	Shallow density anomalies	153
5.4.5	Deep density anomalies	158
5.5	Discussion	160
5.6	Conclusions	165
6	Summary and future work	167
6.1	Summary	167
6.2	Future work	170
A	A Bayesian approach to infer interior mass anomalies from the gravity data of celestial bodies	173
A.1	Proposal distributions	173
A.2	Location of anomalies of target model III	174
B	Bayesian gravity inversion algorithm for inferring finite size density anomalies in planetary interiors	177
B.1	Mean density anomaly of the output models at all layers	177
B.2	Kullback-Liebler divergence of the output models at all layers	178
B.3	Standard deviation of the output models at all layers	181
B.4	Standard deviation of the output models divided the mean density anomaly at all layers	181
	Bibliography	185

List of Tables

2.1	Prior distributions of parameters used by the rjMcMC algorithm . . .	32
2.2	Location, number and magnitude of point masses used in Target Models I and II	33
2.3	Location and diameter of lunar basins used to produce the synthetic gravity data	42
3.1	Prior information of model parameters	62
3.2	Parameters of north cap	71
3.3	Parameters of south cap	71
4.1	Depth layers tesseroïd grid	88
4.2	Uniform prior distributions	92
5.1	Prior distribution used in THeBOOGIe	132
A.1	Location of anomalies 1-25 of the target model III	175
A.2	Location of anomalies 26-50 of the target model III	176

List of Figures

1.1	Crustal thickness map of the Moon	7
1.2	Lunar seismic model by Weber et al. 2011	9
1.3	Lunar seismic model by Garcia et al., 2011	10
1.4	Internal structure of the Moon inferred with lunar seismic data. Squares show the location of Apollo seismic stations. Figure reproduced from Khan <i>et al.</i> [1].	12
1.5	Spherical caps	14
1.6	Voronoi regions	14
2.1	Flowchart of the inversion algorithm	27
2.2	Fit of the gravity acceleration produced by output models and the input data	34
2.3	Likelihood plots for three point mass inversions	37
2.4	Comparison of the target mass distribution with the output distribution and associated probabilities	39
2.5	Number of point mass anomalies recovered by the inversion algorithm	41
2.6	Spherical cap schematic	41
2.7	Fit to the input gravity data	43
2.8	Likelihood of models	45
2.9	Comparison of the target density model with the location of the point mass anomalies of the ensemble mean	46
2.10	Schematic of the gravity acceleration produced by different mass distributions	48
2.11	Effect of observation height and noise hyperparameter on retrieval of mass anomalies	49
2.12	Posterior probability of the latitude and longitude of mass anomalies for three inversions	50
2.13	Posterior probability distribution of point mass radius r	51
3.1	Bouguer gravity anomaly of the Moon	58
3.2	Spherical cap	58
3.3	Flowchart of the inversion algorithm	63
3.4	Changes in model parameters	64

3.5	Likelihood	68
3.6	Misfit with input gravity data	69
3.7	Upper view of output density model vs target model	72
3.8	Radial slice of output density model vs target model	74
3.9	Distribution of values of model parameters	75
3.10	Depth, thickness and density values of the ensemble	77
4.1	Voronoi regions and underlying tesseroïd grid	87
4.2	Flowchart of the THeBOOGIe	95
4.3	Target density model and input gravity acceleration data	99
4.4	Natural logarithm of the likelihood per iteration of THeBOOGIe	101
4.5	Mean gravity acceleration data and average misfit	101
4.6	Normalized Kullback-Liebler divergence and standard deviation	102
4.7	Density anomalies of the target model	105
4.8	Mean density anomalies of the ensemble and normalized Kullback-Liebler divergence as a measure of uncertainty	106
4.9	Mean density anomalies of the ensemble and standard deviation as a measure of uncertainty	107
4.10	Mean density without deep feature	108
4.11	Mean density without deep feature and standard deviation as measure of uncertainty	109
4.12	Density and uncertainty slices	113
4.13	Density profiles with deep anomaly	114
4.14	Density profiles without deep anomaly	115
5.1	Bouguer gravity anomaly of the Moon	125
5.2	Crustal thickness map of the Moon	126
5.3	Convergence and fit to the input gravity data	138
5.4	Mean density model with standard deviation	140
5.5	Mean density model with normalized D_{KL}	141
5.6	Distribution of density values in tesseroïds	142
5.7	Correlation of the density values in tesseroïds	145
5.8	Covariance matrix of tesseroïds in layer 1 and 10.	146
5.9	Map of correlation values	148
5.10	Radial correlation	150
5.11	Correlation length	151
5.12	Topography of the Moon, mean density and cluster location.	155
5.13	Density profiles of clusters	156
5.14	Density profiles of tesseroïds at center of basins	157
5.15	Density and clusters at layers 7-9	161
5.16	Density profile of clusters at layers 7-9	162
B.1	Mean density	179
B.2	Kullback-Liebler divergence	180
B.3	Standard deviation	182

B.4 Standard deviation and mean density	184
---	-----

Chapter 1: Introduction

Knowledge about the interior structure of a planetary body can help shed light on its compositional and thermal evolution. Different data sets and geophysical methods can be used to reveal different properties of this interior structure, with each data set and method having different advantages and limitations. Throughout this work, a novel method to invert satellite gravity data is presented. It was developed with the aim of constraining the density distribution within a spherical body based on the gravity data available and of characterizing the non-uniqueness inherent in gravity inversions. This method is applied to the lunar interior but is motivated by the need to extract information from all the available gravity data of any terrestrial planet and smaller bodies in our solar system. As such, it can be applied to planetary bodies other than the Moon.

This chapter first presents the available seismic, gravitational and topographic data of the Moon and introduces a view of the lunar interior as constrained by this data and other methods. Then it describes the theory behind Bayesian inference and Monte Carlo methods applied to gravity inversions and the advantages of this type of inversion for relaxing prior constraints on the interior and characterizing the non-uniqueness of gravity inversions.

1.1 Spherical harmonics and models of the topography and gravity of the Moon

Global topographic and gravitational data of planetary bodies are commonly represented by a sum of spherical harmonic functions. The spherical harmonics are a set of orthogonal basis functions on the surface of a sphere that can be used to represent any real function. Equations 1.1 and 1.2 show how the function $f(\lambda, \phi)$ is represented by a linear combination of spherical harmonics where Y_{lm} is the spherical harmonic function of degree l and order m and λ and ϕ are the latitude and longitude on the surface of the sphere, f_{lm} are the weights or coefficients of the spherical harmonic functions and \bar{P}_{lm} are the normalized Legendre polynomials [2]. The representation of a function on a sphere using spherical harmonics is analog to a 1D function in Cartesian coordinates being represented by a Fourier series.

$$f(\lambda, \phi) = \sum_{l=0}^{\infty} \sum_{m=-l}^l f_{lm} Y_{lm}(\lambda, \phi) \quad (1.1)$$

$$Y_{lm}(\lambda, \phi) = \begin{cases} \bar{P}_{lm}(\sin \lambda) \cos m\phi & m \geq 0 \\ \bar{P}_{l|m|}(\sin \lambda) \cos |m|\phi & m < 0 \end{cases} \quad (1.2)$$

Global topographic and gravitational data are represented by a sum of spherical harmonics up to a maximum degree l , justified by the resolution of the sampling done by an orbiting satellite. The weights or coefficients of the functions f_{lm} are used to link the interior distribution of density in the body to the observed data

using different assumptions about the interior.

1.1.1 Topography

The topography (h) of a planetary body is the distance from a reference sphere to the surface of the body. The Lunar Orbiter Laser Altimeter (LOLA) of the Lunar Reconnaissance Orbiter [3, 4] measures the time it takes for a laser pulse to travel from the instrument to the surface and back to a receptor and calculates the distance assuming the laser pulse travels at the speed of light. It has collected over 6.5 billion measurements of the lunar surface elevation since 2009 which, together with accurate orbit determination, have been used to construct the highest resolution models of the lunar topography [5]. These models are available in gridded map products where interpolation is used to fill places lacking measurements and in spherical harmonic models up to degree $l = 2500$ in the form:

$$h(\lambda, \phi) = \sum_{l=1}^{\infty} \sum_{m=-l}^l h_{lm} Y_{lm}(\lambda, \phi) \quad (1.3)$$

Where h_{lm} are the spherical harmonic coefficients related to topography.

1.1.2 Gravity

Lateral variations of the mass distribution within a planetary body modifies the expected trajectory of orbiting satellites. Regions with a higher density pull the satellite towards the surface with more force than regions with a lower density. With an accurate orbit determination, the gravity acceleration due to the mass

distribution of a body (g) can be measured and mapped across the surface. The Gravity Recovery and Interior Laboratory (GRAIL) mission provided the highest resolution map of the lunar gravity acceleration to date [6]. Two spacecrafts orbited the Moon along the same trajectory and changes in the distance between the two were measured down to a few microns. The data obtained by the GRAIL missions has been used to construct gridded maps of the gravitational acceleration of the Moon and spherical harmonic models up to order $l = 1200$ [7] in the form:

$$g_r(r, \lambda, \phi) = \frac{GM}{r^2} \sum_{l=0}^{\infty} \sum_{m=-l}^l \left(\frac{R}{r}\right)^l (l+1) C_{lm} Y_{lm}(\lambda, \phi) \quad (1.4)$$

Where g_r is the radial component of the total gravitational acceleration (g), G is the gravitational constant, M is the mass of the Moon, r is the radius of the observation point, R is the mean radius of the Moon and C_{lm} are the spherical harmonic coefficients related to gravity.

1.2 Interior structure of the Moon

The existence of some features in the interior of the Moon is widely accepted by the scientific community while the existence of others is debated. Generally, the shallow structure is constrained with greater confidence because of the availability of different types of data, for example: rock samples, gravity, topography and seismic data. Mid-mantle and deeper features are more obscure because of the lack of samples, the reduced sensitivity of surface data and the sparsity of seismic events that can map out the structure at these depths. We present a summary of the

shallow features, specifically crustal thickness and density anomalies constrained by gravity and topography data, and deeper features of the Moon constrained by seismic data.

1.2.1 Crustal features

The Apollo seismic data can constrain the thickness of the lunar crust directly underneath the Apollo stations while the gravity acceleration (g) and topography (h) sampled by satellites can constrain the thickness of the crust globally, although subjected to assumptions on crustal composition and porosity [8]. The gravitational acceleration due to the topography can be removed from the total acceleration of a planetary body in order to analyze the gravity signal produced by the distribution of mass below a reference radius R . The gravitational acceleration due to topography can be expressed in a similar way as equation 1.4 with C_{lm} coefficients relating the distribution of density existing from $R - h$ with the Bouguer correction g_{BA} . When the density ρ of the material from R to h is constant, C_{lm} can be approximated, in the most basic form, by equation 1.5 [9].

$$C_{lm} = \frac{4\pi R^2 \rho h_{lm}}{M(2l + 1)} \quad (1.5)$$

More accurate approximations require the expansion of higher orders of the topography h_{lm}^n in spherical harmonics and the consideration of variations of density in latitude, longitude and depth [9]. Removing the effect of g_{BA} from the total gravity acceleration of the Moon g , results in the Bouguer gravity anomaly g_B which

is the acceleration produced by the distribution of mass below the mean radius of the Moon. The material closest to the reference radius R has a stronger gravity signal than deeper material because the gravity acceleration signal decreases with distance from the source. Most of the signal of the lunar Bouguer gravity field is then produced by material close to the reference radius of $R = 1739$ km.

Figure 1.1 shows the crustal thickness of the Moon as inferred by Wieczorek *et al.* [10] using the Bouguer gravity field obtained from GRAIL data. The crustal thickness is constrained by the estimation of crustal bulk density from high spherical harmonic degrees and estimation of the mantle density and mean crustal thickness from seismic data [11], varying density and thickness until they produce a gravity acceleration matching the lunar Bouguer acceleration. The most prominent features of the crustal thickness map of the Moon are the dichotomy between near and far side crust, with the far side having thicker crust than the near side and the thin crust within basins, especially in the near side basins which have a crustal thickness close to zero.

The lunar crustal dichotomy is observed as a difference in the mean thickness between the near and far side crust and also a difference in composition. The near side crust has a higher concentration of radioactive heat sources in the Procellarum KREEP Terrain and mare basalts. This dichotomy has motivated the development of different thermochemical models of the evolution of each hemisphere. Laneuville *et al.* [12] found that the existence of a layer enriched in heat sources in the near side produced localized melt in the near side consistent with the amount of lunar volcanism expected.

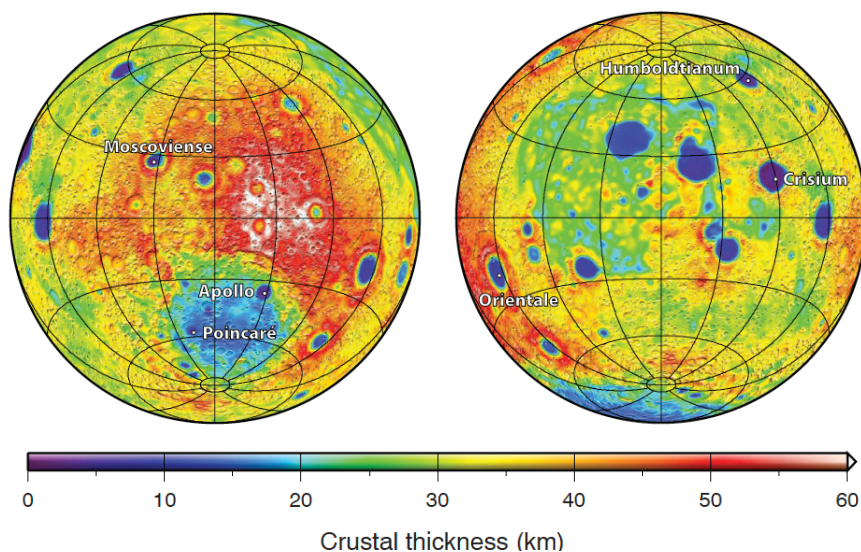


Figure 1.1: Plot of the crustal thickness of the Moon modified from Wieczorek *et al.* [10]. The far side of the Moon (left) has a thicker crust than the near side (right), except for the crust in the South-Pole Aitken basin. The thickness of the crust in the major basins of the near side is close to zero.

Mascons are mass concentrations in a planet or moon with an associated positive Bouguer gravity anomaly. They exist in the Moon, Mars and Mercury. A visco-elastic relaxation model of lunar impacts was developed by Melosh *et al.* [13] to infer the properties of the Moon consistent with gravity data and low crustal thickness in the near side mascons. It was proposed that the impactor removed the crust and exposed mantle material and that the region surrounding the impact craters had a superisostatic state that allowed for very dense material to be supported by the lithosphere, which accounts for the resulting magnitude of the Bouguer gravity anomaly in the center of the basin.

A region of the Moon with thinner crust produces a positive Bouguer gravity

anomaly in the surface because it has more high density mantle material and less low density crustal material than a region with a thicker crust. The estimation of crustal thickness from Bouguer gravity data can be seen as a gravity inversion where density variations or anomalies might exist at the reference depth of the mean crust-mantle interface, if the density of the crust is assumed to be constant. A thinner crust than the reference value is associated with a positive density anomaly since crustal material was expected at a location where there is mantle material. Density anomalies deeper than the reference crust-mantle interface are usually neglected because the gravity signal decreases with increasing distance from the source and their effect in the Bouguer field is smaller than the material above it. It is very important however, to find the properties of density anomalies inside the Moon, deep and shallow ones, since they might change the estimated parameters of the crustal thickness and impose different constraints on evolution models of the Moon.

1.2.2 Deep features

The deep structure of the Moon has been inferred with seismic data and geophysical parameters measured by laser ranging experiments and orbital tracking (mean mass, moment of inertia, tidal numbers, etc). The Apollo lunar seismic network transmitted data to Earth from 1969 to 1977 with seismometers located in a relatively small area on the near side of the Moon [14]. The network recorded more than 12,000 seismic events including unclassified ones, artificial and meteoroid impacts and shallow and deep moonquakes. Because it is harder to smooth out

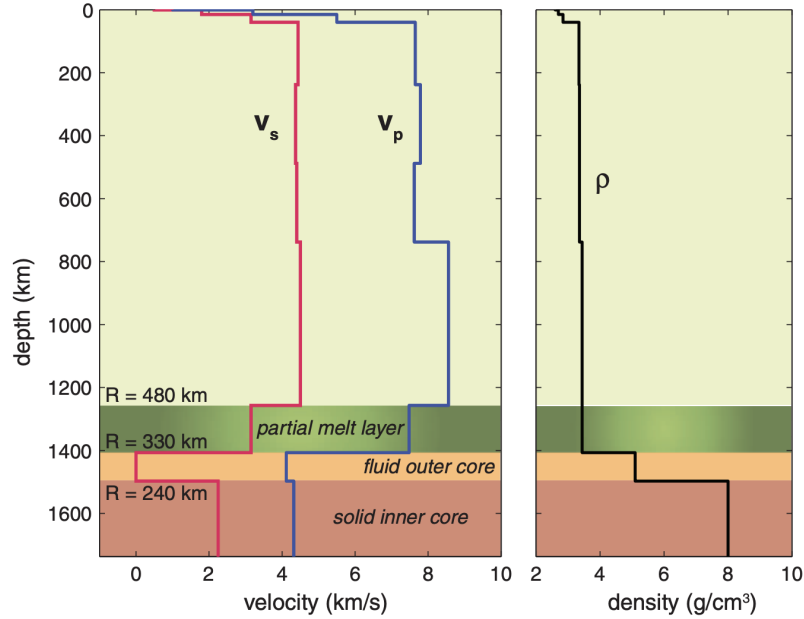


Figure 1.2: Plot of seismic velocities and density profile of the Moon reproduced from Weber *et al.* [15]. A deep partial melt layer is found and the core of the Moon is found to have a radius of 340 km, with a fluid outer core and solid inner core.

inconsistencies between first-arrival readings with fewer data, the interpretation of lunar seismic data is more subjective than the interpretation of Earth data, giving rise to variations between different seismic models of the interior of the Moon. Figures 1.2 and 1.3 show two examples of different profiles of the S and P wave velocities and density in the interior of the Moon.

The deep structure shown in Figure 1.2 was obtained by Weber *et al.* [15] while the structure at depths shallower than 1000 km in the same model was obtained by Gagnepain-Beyneix *et al.* [17]. This model shows velocities and density consistent with measured tidal Love numbers and moment of inertia of the Moon, within uncertainties. A partial melt layer was found at a radius of 480 km and a fluid outer core at 330 with a solid inner core at 240 km.

Figure 1.3 shows velocities and density profiles obtained by Garcia *et al.* [16]

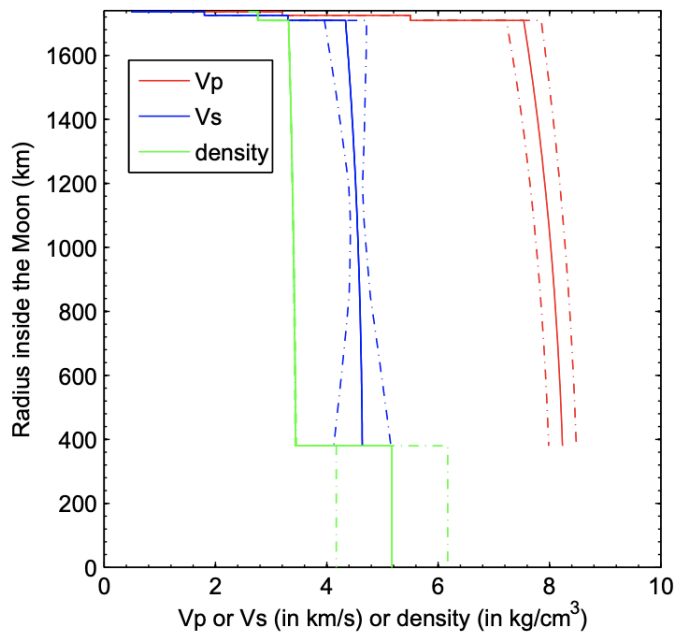


Figure 1.3: Plot of seismic velocities and density profile of the Moon reproduced from Garcia *et al.* [16]. Solid lines show the mean value and dot-dashed lines show the error bars. The deep structure of the Moon is not determined with as much detail as the one shown in Figure 1.2. It is claimed that the paucity of seismic data makes it difficult to constrain a partial melt layer and the structure of the lunar core. The core is found to have a radius of 380 ± 40 km.

with mean values shown by solid lines and error bars by dot-dashed lines. The values are consistent with measured values of mean mass, moment of inertia and tidal Love numbers, within uncertainties. The estimated core radius is 380 ± 40 km and the structure within the core is not constrained. The author claims the paucity of seismic data makes it impossible to constrain it.

These two examples show the large variations between different seismic models of the Moon, particularly, variations in the deep lunar structure below a 1000 km depth. There are also variation between seismic speeds above 1000 km inferred by different research groups because they might use different inversion methods and computational resources available might be different [11, 14, 18, 19, for example].

Figure 1.4 shows the view of the interior of the Moon as constrained by seismic data and geophysical parameters. The squares show the location of Apollo seismic stations on the near side and circles show the location of moonquake clusters. A seismic discontinuity in the range of 500-750 km has been proposed, while a uniform mantle also fits the geophysical data [19, 20]. Deep moonquakes clusters are not uniformly distributed and none has been detected in the region within 40° of the antipode of the Moon [21]. This asymmetrical distribution of moonquake clusters gives rise to two possibilities: seismic rays might be attenuated so they are not observed by the Apollo network or moonquakes might not exist there because of the particular properties of that region. Evidence for a partially molten layer in the lowermost lunar mantle was found by Weber *et al.* [15] constrained by Apollo seismic data and geophysical parameters as mean mass, moment of inertia and tidal Love number. This partially molten layer might attenuate seismic waves coming

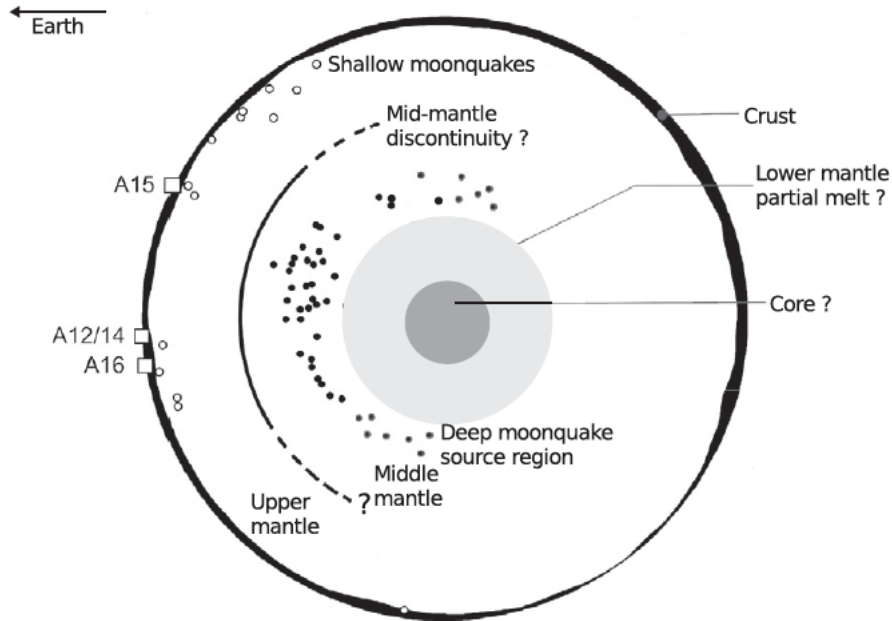


Figure 1.4: Internal structure of the Moon inferred with lunar seismic data. Squares show the location of Apollo seismic stations. Figure reproduced from Khan *et al.* [1].

from far side moonquakes to the seismic stations in the near side of the Moon [1].

1.3 Density models of planetary bodies and parametrization choices

Throughout this work, the term density model is used to refer to a simplification of the continuous 3-D density distribution inside a planetary body and the term parametrization is used to refer to the style of simplification used. In a 1-D density model, for example, the density distribution is parametrized by layers of constant density. The parameters that fully describe the model are the number of layers of density, the depth of the layer interfaces and the density value of each layer. In a 3-D density model, the density distribution might be parametrized by a group of objects with a location defined in 3-D space. In this work, the density distribution in the interior of a sphere is parametrized using three different objects: point masses,

spherical caps and Voronoi regions.

Point masses are points in space with an associated mass and no shape. This parametrization is used to provide information about the location of density anomalies but not its shape or size. The gravity acceleration produced by a group of point masses can be computed very quickly, which makes this parametrization a good option for iterative gravity inversion methods. A density model using this type of parametrization is then described by the number of point masses (n), the location of each point ($\{x\}$, $\{y\}$ and $\{z\}$) and their mass ($\{m\}$), where $\{\}$ are used to describe arrays of $n \times 1$ dimensions. The full advantages and disadvantages of a point mass parametrization, in the context of gravity inversions, are described in Chapter 2.

Spherical caps are the intersection of two concentric spheres and a cone (Figure 1.5). The shape of a positive density anomaly caused by a thinner than average crust below a basin is very well approximated by the shape of a spherical cap. Caps are also versatile since, varying their parameters and locations, other shapes can be approximated too. The parameters that describe density models using a spherical cap parametrization are: density ρ , aperture a , thickness t , depth of outer shell d , longitude ϕ and latitude θ of its center. R is the radius of the planetary interior and r_{max} is the radius of the outer shell of the cap. The inversion of gravity acceleration data using a spherical caps parametrization is described in Chapter 3.

A Voronoi region (VR) is the region that encloses the volume closer to nucleus i than to other nuclei [22]. Figure 1.6 shows six 2-D Voronoi regions dividing the area in the half disk between r_1 and r_2 . All shapes of density anomalies can be parameterized using Voronoi regions, assuming the number or nuclei inside the sphere

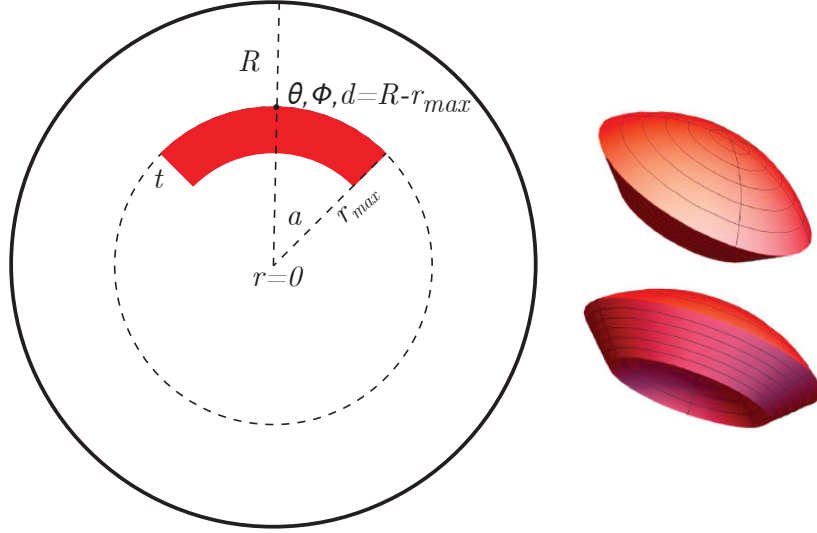


Figure 1.5: 2-D and 3-D representation of a spherical cap. The parameters that define a spherical cap are its density ρ , aperture a , thickness t , depth of outer shell d , longitude ϕ and latitude θ of its center. R is the radius of the planetary interior and r_{max} is the radius of the outer shell of the cap.

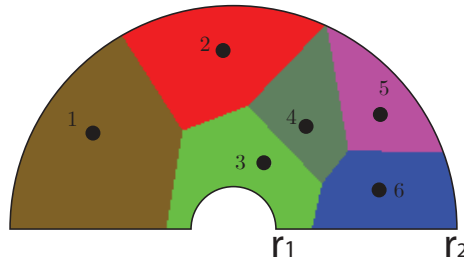


Figure 1.6: Voronoi regions in 2-D. Black dots show the location of nuclei and colors represent a constant value of density within each region.

is large enough. The parameters that describe a density model using a Voronoi parametrization are: the number of VRs (n), the location of each nuclei ($\{x\}$, $\{y\}$ and $\{z\}$) and the density value of each region ($\{\rho\}$). The full advantages and disadvantages of a VR parametrization, in the context of gravity inversions, are described in Chapter 4.

The choice of which parametrization to use is important since some properties of the interior structure of the Moon might be better represented by a layered,

point mass, spherical cap or Voronoi region parametrization. For example, in order to parametrize the lateral variations of crustal thickness in the Moon, a Voronoi parametrization is more adequate than a layered one since the latter can only provide information about the mean thickness. The time and resources spent on computing the gravity acceleration produced by density models vary depending on the parametrization used. The time spent on this computation is specially important in iterative gravity inversions methods where it is performed at each iteration and, in some cases, it is necessary to use thousands or millions of iterations.

1.4 Bayesian inference and non-informative priors in gravity inversions

In order to fully evaluate the likelihood of density anomalies existing within the Moon, a gravity inversion method should not set the location of density anomalies *a priori* and should provide uncertainty information about the density model obtained. Applied to gravity inversions, Bayes' theorem relates the probability distribution that a density model ρ_m is the correct representation of the interior (based on the gravity data of a body $\{g\}$) to the prior knowledge about the interior of the body and the ability of the density model to fit the gravity data.

$$P(\rho_m|\{g\}) = \frac{P(\{g\}|\rho_m)P(\rho_m)}{P(\{g\})} \quad (1.6)$$

Equation 1.6 shows Bayes' theorem where $P(\rho_m|\{g\})$ is called the posterior probability distribution, $P(\{g\}|\rho_m)$ is the likelihood probability distribution, $P(\rho_m)$ is the prior probability distribution and $P(\{g\})$ is usually called the evidence [23]. The density model ρ_m is defined in terms of the parametrization of a real continuous density distribution. For example, using a point mass parametrization, $\rho_m = n, \{x\}, \{y\}, \{z\}, \{m\}$ while a spherical caps one results in $\rho_m = n, \{r_{max}\}, \{\theta\}, \{\phi\}, \{d\}, \{a\}, \{t\}, \{\rho\}$, with each parameter having the same definition as in section 1.3.

Each term in equation 1.6 is a probability distribution function that provides information about how the probability varies with respect to a set of parameters. From the posterior distribution $P(\rho_m|\{g\})$, we can extract the combination of values of $n, \{r_{max}\}, \{\theta\}, \{\phi\}, \{d\}, \{a\}, \{t\}, \{\rho\}$ that produces the most likely density model of the interior based on the gravity data and is limited by the spherical cap parametrization. We can also extract the range of parameter values that produce a 1σ variation of the posterior. Approaching the gravity inversion problem with probability distributions instead of single values for each parameter, allows the retrieval of variation information or uncertainty in the parameters of the density model inferred.

$$P(\rho_m) = P(n)P(\{r_{max}\})P(\{\theta\})P\{\phi\}P(\{d\})P(\{a\})P(\{t\})P(\{\rho\}) \quad (1.7)$$

The prior distribution of the density model ρ_m is the knowledge about its

parameters before data are evaluated. Equation 1.7 shows the expression for the priors of model ρ_m . In the context of gravity inversions, the prior distribution represents the knowledge of the density distribution inside a planetary body before inverting the gravity data. An example of prior information could be that the total mass of the Moon should be 7.346×10^{22} kg as measured by the GRAIL mission [24].

The prior distribution can be adapted to be very informative or non-informative. If there is complete certainty about the location of the center of a spherical cap, for example, the prior distribution of the location ($P(\{\theta\})P\{\phi\})P(\{d\})$) should be a Dirac delta function having a probability equal to infinity at the known location of the cap and zero elsewhere. If there is no information about the location of anomalies in ρ_m , then the prior distribution of the location can be uniform within the limits of a sphere of radius R . Other distributions can be used too in order to represent the prior knowledge we have about the interior. The flexibility of using non-informative prior distributions makes it possible to avoid setting the location of the density anomalies in the Moon *a priori* and, instead, inferring the most likely location and the 1σ variation of that location based on the gravity data.

1.5 Monte Carlo sampling of a posterior probability distribution

Equation 1.8 shows the evaluation of the evidence term in Bayes' theorem as a multi-dimensional integral where the number of dimensions depends on the number of parameters that define the density model. In the case of spherical caps, there are $n \times 7 + 1$ parameters where n is the number of spherical caps inside the sphere.

The posterior has the same dimensions as the evidence term and it might not be a simple distribution with just one maximum. The topography of the posterior might be complex and difficult to characterize by analytic techniques or numerical evaluations of a multi-dimensional integral in a regular grid.

$$P(\{g\}) = \int_{\rho} \int_t \int_a \int_d \int_{\phi} \int_{\theta} \int_{r_{max}} \int_n P(\{g\}|\rho_m)P(\rho_m)dnd\{r_{max}\}d\{\theta\}d\{\phi\}d\{d\}d\{a\}d\{t\}d\{\rho\} \quad (1.8)$$

Monte Carlo methods are commonly employed in the numerical evaluation of integrals in large-dimensional spaces. These types of methods sample a complex probability distribution using different approaches of a random walk [25]. A Monte Carlo method applied to the evaluation of equation 1.6 would obtain a group of density models representative of the posterior probability distribution $P(\rho_m|\{g\})$. From this group of models, the range of model parameters values that are constrained with the gravity acceleration data can be estimated.

The Metropolis-Hastings algorithm [26] is an iterative Monte Carlo method that, at each iteration, samples a density model from the prior distribution, evaluates its likelihood based on how well it fits the gravity acceleration data and assigns a probability of accepting the model based on the ratio of likelihoods between the proposed model and the last accepted model. A proposed model with a higher likelihood has a higher probability of being accepted. The distribution of accepted density models eventually converge to the posterior probability distribution [27]. The group of models obtained at iterations after convergence is achieved, called

the ensemble, is then a representative sample of the density variations that can be constrained with the gravity data. The details of the Metropolis-Hasting algorithm to the inversion of gravity data are found in Chapter 2, 3 and 4 for a point mass, spherical cap and Voronoi parametrization, respectively.

1.6 Research goals

The main objectives of this work are:

- To develop a gravity inversion method that does not require an informative prior distribution on the location of the density anomalies within the Moon and can obtain the variations of the parameters values that can be constrained with the lunar gravity acceleration sampled by the GRAIL data.
- Compare how the interior distribution of density of the Moon and the variations obtained with the novel inversion method differs from the view of the lunar interior accepted by the scientific community.
- Analyze how the inferred interior density model of the Moon relates to possible scenarios of its evolution.

1.7 Outline of the thesis

Chapter 2 introduces a novel gravity inversion method and a point mass parametrization of the density anomalies within a sphere. The method combines the elements described in sections 1.3 and 1.5 in order to use non-informative prior

information about the number of anomalies existing in the interior and the location and mass of each of them.

Chapter 3 describes the differences in the inversion algorithm of Chapter 2 when a spherical cap parametrization is used. The computation time of each iteration is higher and the method requires more iteration before convergence. This increase in computational resources needed is compensated by the ability of the spherical caps to retrieve the shape and size of density anomalies within the sphere, specially the ones related to impact basins.

Chapter 4 describes how the interior density distribution in a sphere can be parametrized by Voronoi regions (VRs) and how the calculation of the gravity field of density models using this parametrization can be made efficient, allowing for a reduction of the computing time when compared with spherical caps. Synthetic gravity data is inverted using this VR algorithm and a the shape and size of a mid-mantle anomaly is inferred correctly.

Chapter 5 describes the inversion of the Bouguer gravity field of the Moon using the novel gravity inversion method with a Voronoi parametrization. Shallow anomalies are compared to the ones related to previous crustal thickness estimations while deep anomalies are related to features inferred with seismic data.

Chapter 6 summarizes the findings of previous chapters and describes the future work that would be needed in order to refine the view of the lunar interior obtained from the gravity inversion of GRAIL data and the future work needed to link the interior features to evolution models of the Moon.

Chapter 2: A Bayesian approach to infer interior mass anomalies from the gravity data of celestial bodies

Published as: Kristel Izquierdo, Vedran Lekić, Laurent G. J. Montési, A Bayesian approach to infer interior mass anomalies from the gravity data of celestial bodies, *Geophysical Journal International*, Volume 220, Issue 3, March 2020, Pages 1687-1699, <https://doi.org/10.1093/gji/ggz544>

2.1 Abstract

We developed a Transdimensional Hierarchical Bayesian (THB) inversion algorithm that provides an ensemble of mass distribution models compatible with the gravitational field of a celestial body. Using this ensemble of models instead of only one, it is possible to quantify the range of interior parameters that produce a good fit to the gravity acceleration data. To represent the interior structure of the planet or moon, we parameterize mass excess or deficits with point masses. We test this method with synthetic data and, in each test, the algorithm is able to find models that fit the gravity data of the body very well. Three of the target or test models used contain only point mass anomalies. When all the point mass anomalies in the target model produce gravity anomalies of similar magnitudes and the signals

from each anomaly are well separated, the algorithm recovers the correct location, number and magnitude of the point mass anomalies. When the gravity acceleration data of a model is produced mostly by a subset of the point mass anomalies in the target model, the algorithm only recovers the dominant anomalies. The fourth target model is composed of spherical caps representing lunar mass concentration (mascons) under major impact basins. The algorithm finds the correct location of the center of the mascons but fails to find their correct outline or shape. Although the inversion results appear less sharp than the ones obtained by classical inversion methods, our THB algorithm provides an objective way to analyze the interior of planetary bodies that includes epistemic uncertainty.

2.2 Introduction

We introduce a Transdimensional Hierchical Bayesian (THB) gravity inversion algorithm and evaluate its performance with a fast forward problem. A point mass is an idealization of a particle that contains all of its mass in a point with zero volume. This idealization allows the use of simple equations to calculate the gravity acceleration produced by particles of this type. In order to test the efficacy of the gravity inversion method while keeping each iteration quick, the algorithm uses a distribution of point masses inside the sphere to fit a given set of gravity acceleration values. The number of point masses is not fixed *a priori* (transdimensional aspect) but instead chosen in light of the data. The location of each point mass could be anywhere between the core-mantle boundary and the surface of the spherical

body. The variance in the data is also estimated as part of the inversion technique (hierarchical aspect). The Bayesian aspect involves the use of Bayes' theorem to assign a probability to each mass distribution model based on how well it fits the gravity data and additional constraints.

In gravity inversions to date, the use of a Transdimensional Bayesian algorithm has been limited to the recovery of 2D local-scale density structures. The shape of a 2D polygon, defined by a fixed density difference and size, a varying number of vertices in the x-y plane and an infinite length in the z-direction, can be recovered [28]. In Titus *et al.*, 2017 [29], the additional parameters of density difference and size of a rectangle containing the polygon were also estimated.

The advantage of our THB method is that it requires fewer prior constraints and explores a larger model space. These two characteristics make it possible to use this method for the inversion of gravity data of bodies that are not well known as well as for the ones from which we have plenty of geological priors.

In Section 2.3, we describe the Bayesian approach to the inference of mass distribution models and the general logic of the algorithm. In Section 2.4, we show the results of inverting several synthetic gravity fields to illustrate the capabilities and limitations of the method. In the first set of tests, the input gravity acceleration data is produced by a distribution of point masses while in the second set, it is produced by spherical caps which are more realistic mass distributions. Section 2.4.2.4 discuss the uncertainty related to using point masses to recover three-dimensional density features.

2.3 Inversion technique

In this section, we describe how Bayes' rule is used to assign probabilities to different mass distributions inside a sphere when the number of parameters is not fixed *a priori*. We also present the reversible jump Markov chain Monte Carlo (rjMcMC) algorithm [30] used to perform THB gravity inversions. We will use brackets $\{\}$ to represent sets of values for one parameter, such as the value of each anomaly in the model $\{m\}$, or the gravity acceleration data, $\{g\}$. Since $\{g\}$ is only informative to the inversion when the effect expected from a sphere of constant density is removed, the terms gravity acceleration data or gravity anomaly might be used to refer to $\{g\}$.

2.3.1 Bayesian inference

Bayes' rule states that the probability P of having an interior mass anomaly with magnitude m given the gravity acceleration values at the surface $\{g\}$ is proportional to the probability of observing $\{g\}$ if the mass anomaly is m multiplied by the probability of the mass anomaly being m according to our current understanding of its possible values: $P(m|\{g\}) \propto P(\{g\}|m)P(m)$. $P(m|\{g\})$ is formally known as the posterior probability function, $P(\{g\}|m)$ as the likelihood and $P(m)$ is the prior.

2.3.2 Transdimensionality

In the classical use of Bayesian inference, the number of mass anomalies n in the model was fixed. In the case described above, it was set to one. Thus m was a scalar. If the number of mass anomalies is not known *a priori*, n can be treated as another parameter to invert from data $\{g\}$. Equation 2.1 shows the updated probability distribution function $P(\{m\}, n|\{g\})$.

$$P(\{m\}, n|\{g\}) \propto P(\{g\}|\{m\}, n)P(\{m\}, n) \quad (2.1)$$

There are now $n+1$ unknowns to be determined. A transdimensional inversion provides the added flexibility of estimating the number of layers in a 2D velocity model using seismic data, for example, or the number of density anomaly objects in a 3D model using gravity data. This flexibility is required because we do not actually have that information when working with real data, since the anomalies lie in the inaccessible interior of the planet.

2.3.3 Reversible jump Markov chain Monte Carlo algorithm (rjM-cMC)

We represent the mass anomalies inside a sphere with point masses. We describe in section 2.4.2.4 how this parametrization performs when the gravity data to invert is produced by finite-sized objects instead of point masses. Using this parametrization, the interior mass distribution model $\{p_m\}$ contains the values

of each parameter describing the mass distribution in the interior of the sphere: $\{p_m\} = \{n, \{m\}, \{x\}, \{y\}, \{z\}, \sigma_g^2\}$ where n is the number of point mass anomalies, $\{m\}$ is the set of values of the mass anomalies in kilograms, $\{x\}$, $\{y\}$ and $\{z\}$ are their Cartesian coordinates in kilometers and σ_g^2 is the variance of the white noise of the gravity acceleration data in $(m/s^2)^2$. The corresponding posterior probability implied by Bayes' theorem in equation 2.2 is:

$$\begin{aligned} P(\{p_m\}|\{g\}) &= P(n, \{m\}, \{x\}, \{y\}, \{z\}, \sigma_g^2|\{g\}) \\ &\propto P(\{g\}|\{p_m\})P(\{p_m\}) \end{aligned} \quad (2.2)$$

with the likelihood $P(\{g\}|\{p_m\})$ given by:

$$P(\{g\}|\{p_m\}) = \frac{1}{\sqrt{2\pi^n(\sigma_g^2)^s}} \exp\left(-\frac{\Phi}{2}\right) \quad (2.3)$$

where s is the number of independent observation points and

$$\Phi = (\{g\} - \{g_M\})^T \frac{1}{\sigma_g^2} (\{g\} - \{g_M\}) \quad (2.4)$$

where $\{g_M\}$ are gravity accelerations predicted by model $\{p_m\}$.

Using the Metropolis-Hastings criteria [31], we construct an algorithm that finds the values n , $\{m\}$, $\{x\}$, $\{y\}$, $\{z\}$, σ_g^2 that best fits the data and additional constraints in an unbiased way. The process to do this is divided in two steps: 1) proposing models from the distribution $q(\{p'_m\}|\{p_m\})$ and 2) accepting models with

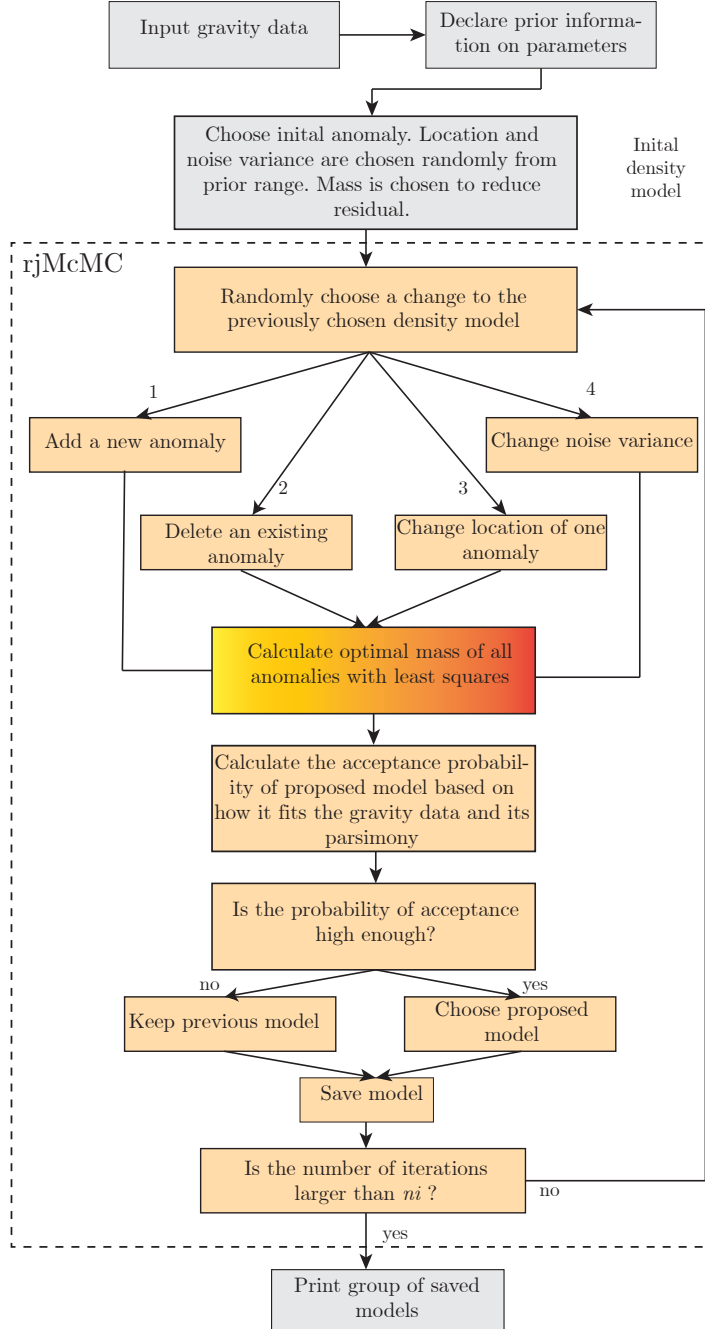


Figure 2.1: Flowchart of the THB gravity inversion algorithm. The initial model is chosen randomly from the prior distribution and subsequent models are obtained from the current model either by changing the position of a randomly-chosen anomaly, by changing the noise variance, or by adding a new or removing an existing anomaly according to the reversible jump Markov chain Monte Carlo (rjMcMC) procedure. Proposed models are accepted or rejected based on their relative likelihood (Equation 6). After a burn-in period, models are saved to the ensemble, which represents a sample of the posterior distribution $P(\{p_m\}|\{g\})$. Note that masses of the anomalies are not explored, but rather inverted for at each step of the algorithm.

the probability given by equation 2.5 .

$$\alpha(\{p'_m\}|\{p_m\}) = \min \left[1, \frac{P(\{p'_m\})P(\{g\}|\{p'_m\}) q(\{p_m\}|\{p'_m\})}{P(\{p_m\})P(\{g\}|\{p_m\}) q(\{p'_m\}|\{p_m\})} \right] \quad (2.5)$$

The expressions for the proposal distributions and derivation are presented in Appendix A.1. When adding a new anomaly, its parameters are taken from the prior distributions which are uniform. When changing the location of an existing anomaly, the new location is selected from a normal distribution with mean at the current location.

Figure 2.1 shows a detailed flowchart of the algorithm. At each step of the rjMCMC, we propose a random new model based on perturbing the existing model. We either remove or change the location of a randomly selected anomaly, or we introduce a new anomaly with a location sampled randomly from the prior, or we perturb the variance describing the noise in the data.

It is important to note that after randomly choosing the location of the anomalies, we compute their corresponding masses by minimizing the difference between the predicted and observed acceleration values. This is possible thanks to the linear relation between the magnitude of a point mass and the acceleration it produces: $\{g\} = D\{m\}$. Here, D is a matrix constructed using the gravitational constant G and inverse of the distances between the point masses and the sampling points, d_{ij} , where i is the index of the mass considered and j is the index of the observation point: $D_{ij} = G/d_{ij}^2$. The optimal value of the point masses are determined in a least squares sense: $\{m_o\} = (D^T C_g^{-1} D)^{-1} D^T C_g^{-1} \{g\}$. Because uncertainty on

the data $\{g\}$ are assumed to be normally distributed, $P(\{g\}|\{p_m\})$ will be represented by a generalized Gaussian with mean $\{m_o\}$ and posterior covariance given by $\tilde{C}_m = (D^t C_g^{-1} D + C_m^{-1})^{-1}$ [25], where C_g is the data covariance matrix ($C_g = \sigma_g^2 I$) and C_m is the prior model covariance matrix. We set C_m to be a diagonal matrix since masses of individual anomalies are not assumed to be correlated *a priori*. The prior model covariance matrix also acts to stabilize the inversion for $\{m\}$ by contributing to the diagonal.

The advantage of solving for the optimal set of mass anomalies $\{m\}$ at each step of the rjMcMC is that doing so reduces by $\{n\}$ the dimensionality of the inverse problem, which dramatically improves the efficiency of the search, as we only have to explore a fraction of the model space. However, this also means that instead of obtaining the likelihoods of randomly generated models at each step of the rjMcMC (which is commonly the case), we only obtain the likelihoods for randomly generated models in which the values $\{m\}$ have been tuned to optimal values $\{m_o\}$ so that:

$$P(\{g\}|\{p_{m_o}\}) = \max_{\{m\}} P(\{g\}|\{p_m\}) \quad (2.6)$$

The presence of tunable parameters means that we cannot simply use the ratio of likelihoods when computing acceptance probabilities in Equation 2.5. Instead, it is necessary to marginalize over the set of tunable parameters $\{m\}$ prior to comparing likelihoods and deciding to accept or reject a proposed model. The marginalization removes the dependence on the tunable parameters:

$$\begin{aligned}
P(\{g\}|n, \{x\}, \{y\}, \{z\}, \sigma_g^2) &= \int_{m_{\min}}^{m_{\max}} P(\{g\}|\{p_m\})P\{m\}d\{m\} \\
&= \frac{\sqrt{(2\pi)^n |\tilde{C}_m|}}{(m_{\max} - m_{\min})^n} P(\{g\}|\{p_{m_o}\}). \tag{2.7}
\end{aligned}$$

Putting this all together, the acceptance probability α used by the algorithm becomes:

$$\alpha = \min \left[1, \left(\frac{\sigma_g^2}{\sigma_g'^2} \right)^s \exp \left(-\frac{\Phi - \Phi'}{2} \right) \sqrt{\frac{|\tilde{C}_{m'}|}{|\tilde{C}_m|}} (m_{\max} - m_{\min})^{n-n'} \right] \tag{2.8}$$

Since the optimal values of the anomalies is obtained by linear inversion, there is not a strict limit on its minimum and maximum possible values (m_{\min} and m_{\max}). We use instead -10^{22} to 10^{22} kg as a sufficiently wide range in equation 2.8.

2.3.4 Hierarchical parameter

As described above, our algorithm treats the uncertainty of the data, parameterized by the variance of the normal distribution describing white noise in the data (σ_g^2), as a parameter to be inferred during the inversion. This formulation is referred to as hierarchical [32]. Since the complexity of the mass distribution models obtained by the algorithm depends on the level of noise in the data, it is important to estimate the noise variance together with the estimation of the values of the model parameters [33]. Inversions of data with higher noise levels should produce

simpler models. Lower noise levels produce more complex models since a greater number of model parameters can be justified when attempting to fit the data. Even when the noise variance is estimated by external methods, like measurement uncertainties from satellite tracking data, estimating the hierarchical noise parameter through the inversion can be important in assessing how well the model can fit the data (epistemic uncertainty). For example, Olugboji *et al.* [34] found that when constructing surface wave phase velocity maps, the hierarchical noise estimates are systematically higher than reported data uncertainties, and attributed the difference to additional uncertainty arising from modeling assumptions. Gao *et al.* [35] details how the parameterization of the model itself can degrade or bias inferences obtained by transdimensional Bayesian inversion; we later discuss how these effects manifest in the hierarchical noise parameter in our inversions. In this work, the level of noise is unknown but it is assumed to have a normal distribution.

2.4 Validation

In order to assess the ability of the proposed method to characterize the mass anomaly distribution within a celestial object, we carry out a suite of validation tests. We construct four different mass distributions by specifying the location and magnitude of mass anomalies inside a sphere with radius R and zero mean density. We call these mass distributions target or true mass distributions. We calculate the gravity acceleration produced by each target distribution and apply a level of white noise to it. The inversion algorithm described in Section 2.3 uses this synthetic

	x	y	z	σ_g^2	n
Min	$-R$	$-R$	$-R$	$10^{-14} \text{ (m/s}^2\text{)}^2$	1
Max	R	R	R	$10^{-10} \text{ (m/s}^2\text{)}^2$	140

Table 2.1: Prior distributions of parameters used by the rjMcMC algorithm. R is the radius of the sphere. The limits of x , y and z are clearly marked by the boundaries of the sphere since anomalies cannot be outside it. The distributions of σ_g^2 and n do not have tangible limits. We instead set them to sufficiently large values so that the posterior distributions for these parameters are not truncated. In other words, the possible ranges of values are wide enough not to bias the search of the rjMcMC.

gravity data as input to obtain a mass distribution ensemble. We then compare the mean of the ensemble with the corresponding target model to see how effectively the algorithm recovered the mass distribution that produced the input gravity data.

The validation tests are divided in two types according to whether the mass anomalies of the target models are point masses or three-dimensional objects. Since the algorithm uses point masses to construct an output mass distribution, the goal is to test how well the algorithm recovers the location and magnitude of anomalies with a perfect parameterization and how it approximates the shape of finite objects with point masses.

2.4.1 Point masses as the target mass distribution model

In the first series of validations tests, the target mass distribution is built using point mass anomalies. It might be expected that the inversion algorithm, which parameterizes mass anomalies as point masses, should be able to recover the distribution perfectly. However, the resolution of the gravity data and the natural attenuation of $1/r^2$ of the gravity acceleration limit the combination of depths and magnitudes it can recover. In addition, the transdimensional aspect of the inversion

Parameter		Target Model I					Target Model II				
		1	2	3	4	5	1	2	3	4	5
Latitude ($^{\circ}$)	θ	31.7	43.9	22.0	15.0	-65.9	-15.2	-15.2	-15.2	-15.2	-15.2
Longitude ($^{\circ}$)	λ	-90	12.8	155.5	-63.3	-168.3	-80.3	-80.3	-80.3	-80.3	-80.3
Radius (R)	r	0.99	0.90	0.80	0.70	0.60	0.99	0.96	0.93	0.90	0.87
Mass (kg)	m	10^{16}	10^{18}	2×10^{18}	5×10^{18}	9×10^{18}	10^{16}	10^{16}	10^{16}	10^{16}	10^{16}

Table 2.2: Location, number and magnitude of point masses used in Target Models I and II.

method is inherently parsimonious, so the output distribution is likely to contain fewer mass anomalies than the target model.

We consider three cases in this category of target models. Target Model I and Target Model II contains five point mass anomalies (Table 2.2). In Target Model I, the deeper anomalies have larger magnitudes than the shallower anomalies and all the anomalies have different latitudes and longitudes. In Target Model II all the mass anomalies have the same latitude, longitude and mass but different depths. Target Model III contains 50 anomalies. Their locations and magnitudes are chosen from an uniform probability (see supplementary material).

The parameters to recover are $\{m\}$, $\{x\}$, $\{y\}$, $\{z\}$, n and σ_g^2 . The prior information given to the algorithm is shown in Table 2.1 with the only additional constraint that anomalies should be located inside the sphere ($x^2 + y^2 + z^2 \leq R^2$). All inversions ran for 1×10^6 steps using only one MCMC chain.

2.4.1.1 Fit to input gravity data

Figure 2.2 shows the input gravity acceleration data used for each validation test and the gravity acceleration data of the mass distribution found by the algorithm. Each dataset contains 2542 acceleration values uniformly sampled across the

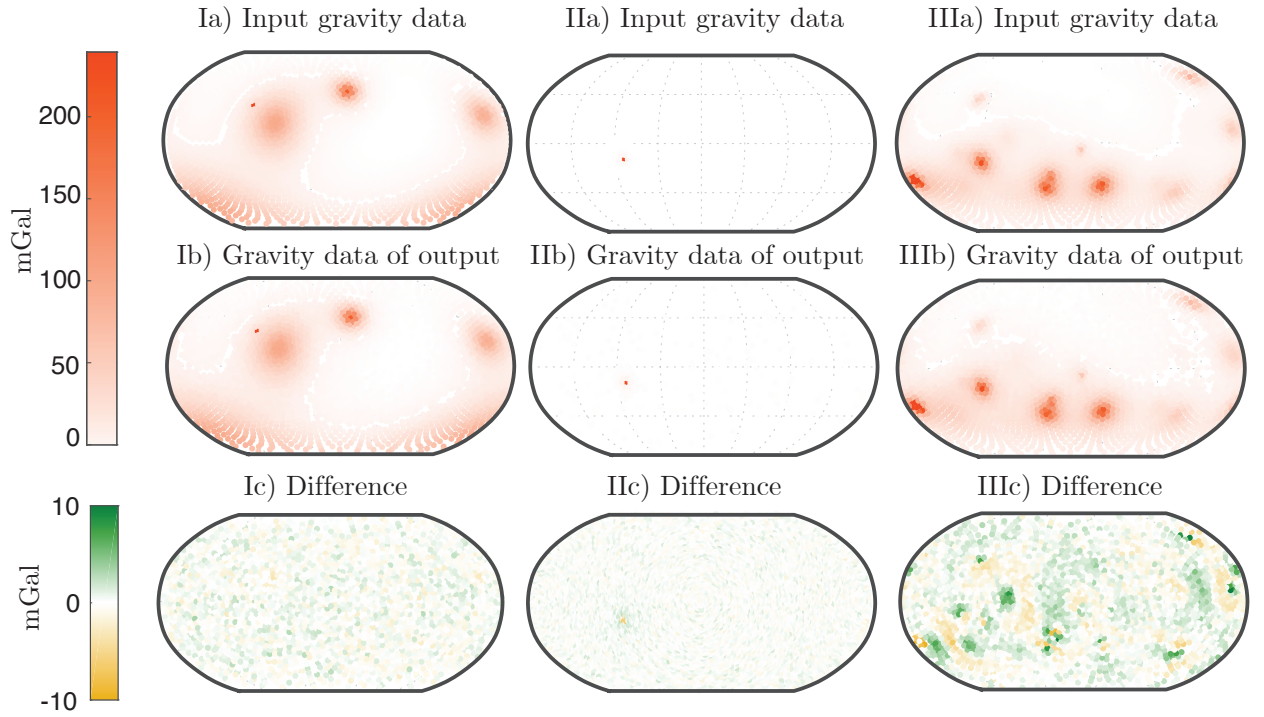


Figure 2.2: Gravity acceleration data used as input in the inversion (a) and gravity acceleration data produced by the output which is the mean of the ensemble of mass distribution models (b). In the three cases shown here, the target model consists of point masses. Target model 1: five point masses with different depths and magnitudes. Target model II: five point masses with the same latitude and longitude but different depths. Target model III: fifty point masses with random locations and magnitudes. The maximum misfit magnitude is 10 mGal in places where the acceleration is 200 mGal or higher, as shown by maps in c), indicating that the algorithm is able to provide satisfactory data fits. Figures III a) and III b) are saturated to 200 mGal to show the gravity signal produced by several point masses. Otherwise the maps are dominated by the signal of one very large and shallow point mass. Table A.1 and A.2 in the supplementary material provide the locations and magnitudes of all 50 point masses.

surface of the sphere. In case I, the gravity signature of each of the five point mass anomalies are clearly distinguished because larger magnitude deeper point masses produce gravity signatures of similar amplitude as the smaller but shallower point masses and because all the point mass anomalies are positioned at different latitude and longitude. At first sight, it would appear that target model II has a gravity anomaly only at one location. That is because the five input masses have the same latitude, longitude and magnitude but different depths. Deeper anomalies with the same magnitude produce a broader and weaker gravity signal than shallower ones. In case III, the gravity data is produced by 50 point mass anomalies with random locations and magnitudes. For visualization, the gravity maps in Figure 2.2 III are saturated at 250 mGal in order to show the gravity signatures of many anomalies. In reality, the shallowest mass anomaly produces a gravity acceleration as strong as 1000 mGal that dominates the gravity map, overpowering the other signals.

In all three cases, our inversion algorithm is able to find a mass distribution that fits the input gravity data. Additionally, the noise of the input gravity accelerations σ_g is recovered to 2% error of the true value. However, the purpose of the inversion is not just to reproduce the input gravity values but to constrain the source. We discuss next the distribution of mass anomalies in the output model and how they compare with the target distribution.

2.4.1.2 Fit to target density model

As gravity inversions are non-unique, fitting the input gravity data does not mean the algorithm has found the correct mass distribution. In this section, we compare the mean of the model ensemble obtained by the algorithm with the known correct mass distribution (target model). In order to do that, we examine the posterior probability distribution of the models, $P(\{p_m\}|\{g\}) = P(n, \{m\}, \{x\}, \{y\}, \{z\}, \sigma_g^2|\{g\})$. Which shows the most likely combination of parameters given the gravity data. This posterior probability is obtained by measuring the frequency of different values of parameters from an ensemble of models obtained by the algorithm. The ensemble only contains models sampled after convergence is achieved. In other words, the sampling starts only after the residual between model prediction and input data (Equation 2.4) no longer changes significantly compared to the variation in the first set of iterations.

The locations of the gravity anomalies in the output acceleration data match those of the input, (Figure 2.2). This shows that density anomalies found by the algorithm are present at the correct latitudes and longitudes. Therefore, we focus on describing the distribution of the parameters that have trade-offs in gravity inversions: the magnitude and depth of anomalies.

Figure 2.4 shows the comparison between the target and output models for test cases I, II and III. In test case I, there is perfect agreement between the mass anomalies in the target model and the inversion result. This shows that the algorithm is able to find the correct distribution of mass anomalies inside the sphere with

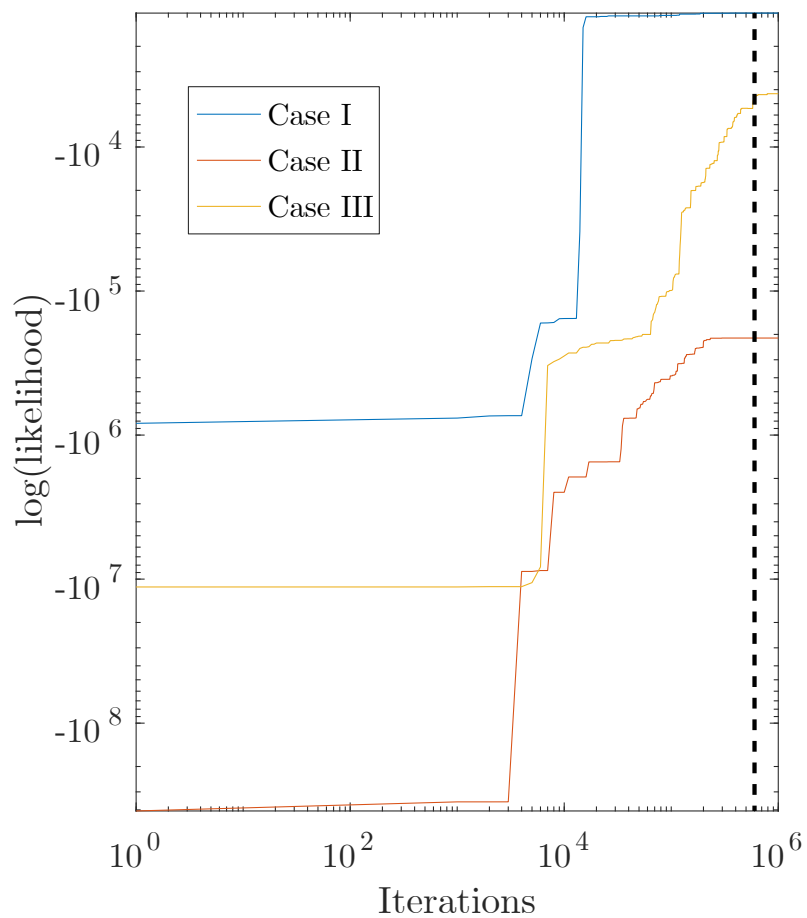


Figure 2.3: Likelihood plots for cases I, II and III. We can see that the likelihood increases with the number of iterations until it reaches a higher value where it stabilizes. The ensembles are composed of models from the 4×10^5 to the 1×10^6 iteration.

non-informative priors for the situations when the gravity signature of the masses are equally dominant. In a more graphical way, this means that we can easily identify the signature of all masses in the gravity map (Figure 2.2 I) . Similarly, perfect matches were obtained for target models with n from 1 to 20 as long as each gravity signature was easily identifiable.

For case II, the algorithm fails to match the correct distribution. Instead, it finds a distribution that fits the gravity data using fewer point mass anomalies. As shown in Figure 2.4 II, the target model has five mass anomalies of the same magnitude (1×10^{16} kg) but different depths. Deeper mass anomalies produce very low magnitude gravitational acceleration compared to the shallower one which causes the fit of the model to the data to be dominated by one shallowest mass. As can be seen in Equation 2.8 in the term $(m_{\max} - m_{\min})^{n-n'}$ where n is the number of point masses, the THB algorithm prefers models with fewer anomalies, which means that it tends to match the gravity signature of the dominant anomalies only. Here the algorithm favors a single anomaly with a larger magnitude in a shallow location instead of the correct location of the five anomalies. The deeper mass anomalies in the target model produce subtle gravity signatures that are considered noise by our inversion algorithm. A lower noise variance (σ_g^2) would enhance the significance of weak features of the input gravity data, and would therefore justify the placement of additional anomalies.

For test case III, something similar to test case II occurs. In Figure 2.4 III, we can see that the mass anomalies located in the upper right triangle of the plot r vs m are preferentially recovered by the algorithm. This means that, again, the

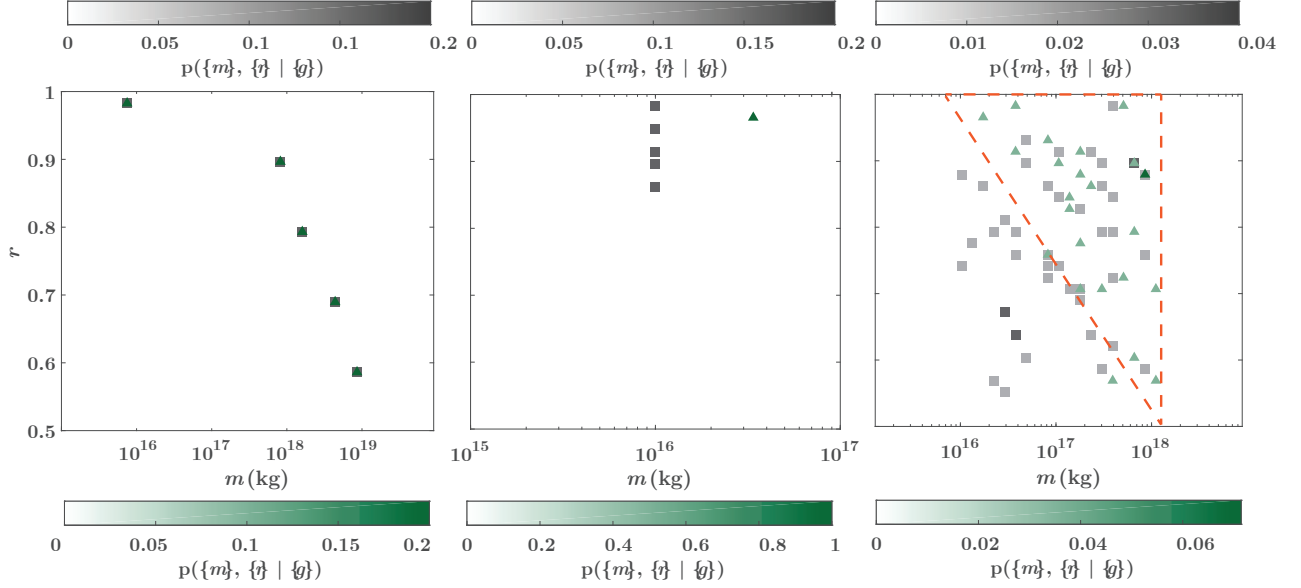


Figure 2.4: Comparison of target mass anomalies (squares) with output mass anomalies (triangles) and associated probability distributions for cases I, II and III. The location of the symbol shows the magnitude of a point mass and its distance from the center of the sphere. The color shows the probability of having a point mass there based on the input gravity acceleration data. In case I there is perfect agreement between the output and target models and between the probability distributions. In case II the inversion favors a single point mass anomaly of larger magnitude than the five point mass anomalies in the target model. The point mass anomalies in output model III have shallower locations or larger magnitudes. The red triangle is included to highlight this fact. Point mass anomalies outside this triangle appear in the target model but not in the output one. This mismatch happens because the algorithm is parsimonious and uses the fewer number of total anomalies possible. Deep and small anomalies do not affect the residual as strongly as shallow and large ones, so the parsimony of the algorithm works against their recovery.

algorithm is less sensitive to the presence of deeper, smaller masses that do not contribute much to the residual. Reflecting its inherent parsimony, the algorithm fits the gravity data with fewer masses than present in the target model. Figure 2.5 shows the number of anomalies recovered by the THB method in comparison with the ones contained in the true or target models of test cases I, II and III.

In summary, the algorithm is able to find mass distribution models that fit the input gravity data and accurately recovers the input noise levels. However, in all

three cases, the inherent parsimony of the method makes it difficult to recover all the anomalies when a subset of them dominate the gravity data and overpower the contributions of smaller and/or deeper masses to the residual. Lower input noise levels would justify the introduction of additional point masses. This behavior is common in all transdimensional inversions where the number of seismic velocity layers or density anomaly objects is not specified *a priori* (e.g., number of layers recovered in transdimensional Bayesian surface wave dispersion) [35]. Although it might be tempting to fix the number of parameters in order to avoid this problem in the tests presented here, that approach is not appropriate for the study of real gravity datasets, where the number of density anomalies is not known *a priori*. Instead, it is important to understand the limitations of transdimensional inversions and interpret the results taking these limitations into account.

2.4.2 Spherical caps as the target density model

As a second set of validation tests, we invert a set of gravitational acceleration values that was produced by three-dimensional objects instead of point masses. It is necessary to see which features of our target three-dimensional objects we can recover using point masses. If necessary, future algorithm development may use a model parameterization with finite sized objects to recover target three-dimensional objects. The objects used here are similar in shape to the expected mass anomalies found under major impact basins on the Moon, called mascons [36]. These objects are represented by spherical caps such as the one shown in Figure 2.6.

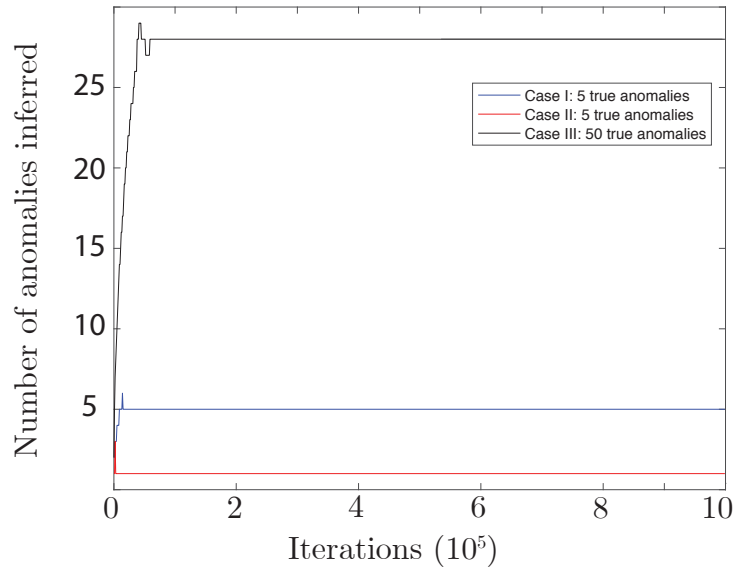


Figure 2.5: Number of anomalies inferred by the THB algorithm. For case I, the correct number of anomalies is found, while for cases II and III, fewer anomalies are recovered. This is a reflection of the parsimony of the algorithm. Since some deep and small anomalies do not substantially affect the residual (defined by equation 2.4), and the algorithm prefers simpler to more complex models (i.e. it is parsimonious), the algorithm does not introduce these masses when fitting the input gravity acceleration data.

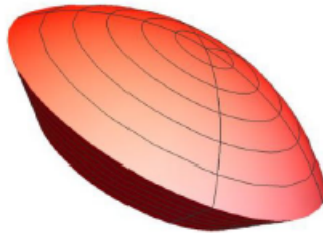


Figure 2.6: Spherical caps used as mass anomaly objects in the target model. They represent the volume inside a spherical shell of certain thickness $R_{\max} - R_{\min}$ limited by a concentric cone of aperture α

Name	Latitude	Longitude	Diameter (km)	Aperture (°)
Imbrium	32.8 N	15.6 W	224	23.21
Nubium	21.3 S	16.6 W	143	14.82
Serenitatis	28 N	17.5 E	141	14.61
Australe	38.9 S	93 E	120	12.44
Crisium	17 N	59.1 E	165	17.10
Humorum	24.4 S	38.6 W	115	11.92
Smythii	1.3 N	87.5 E	145	15.03
Nectaris	15.2 S	25.5 E	100	10.36
Oriente	19.4 S	92.8 W	110	11.40

Table 2.3: Location and diameter of lunar basins used to produce the synthetic gravity data. The density anomaly of these mascons is 300 kg/m^3 .

2.4.2.1 Fit to input gravity data

We use synthetic gravity acceleration data that provides a simpler, idealized view of the lunar gravity field [37]. This radial gravity acceleration map (Figure 2.7a) was obtained by computing the radial gravity acceleration produced by spherical caps with sizes, latitudes and longitudes listed in Table 2.3. The location and size of these caps are similar to those of major basins on the Moon where large mass concentrations, called mascons, were identified [38, 39]. The outer shells of the caps were set to $r = 0.99$ and the inner ones to $r = 0.97$. The black circles in Figure 2.7 show the outline of these caps and the name of basins on which they are based [40]. The 2562 acceleration values of this map and the prior probability distributions in Table 2.1 were the inputs to the inversion. As in the previous test, the prior information was not informative, only limiting the anomalies to be inside the sphere.

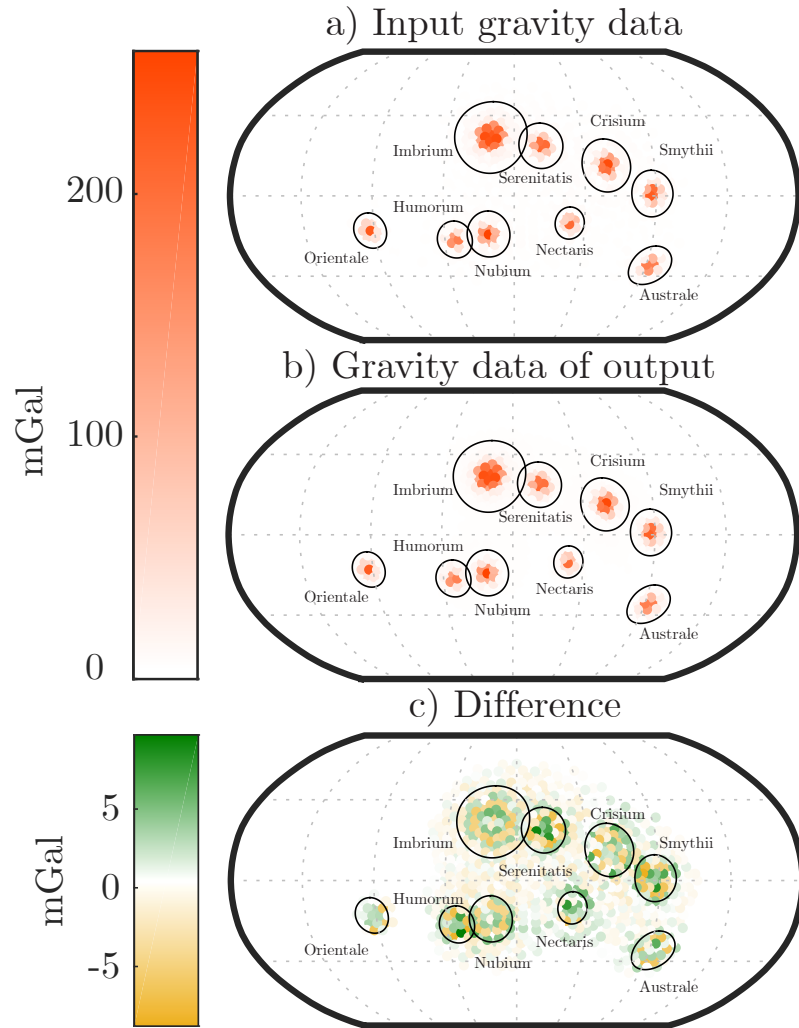


Figure 2.7: Comparison between the gravity data used as input in the inversion (a) and the gravity data produced by the mass distribution model found by the algorithm (b). The maps of differences (c)) show that the error is only 5 mGal in places with a gravity acceleration larger than 200 mGal.

2.4.2.2 McMC set up

One hundred independent Markov chains were run using the gravity acceleration dataset of Figure 2.7 as input. Each of these chains had a different initial mass distribution model $\{p_m\}$ chosen randomly from the prior distribution. Each chain was run for 5×10^6 iterations of the rjMcMC cycle shown in Figure 2.1. Figure 2.8 shows that the likelihood of the density models increases with increasing number of iterations. After 4 million iterations, the value of the likelihood no longer changes significantly and is similar for models of all chains. This is taken as a sign of convergence. The ensemble is obtained by sampling one model every 1000 iterations starting after 4 million iterations. Therefore, the ensemble contains 1000 models from each of the 100 chains. The average gravity data produced by this ensemble matches the input gravity data very well with differences of only ± 2 mGal (Figure 2.7 b).

2.4.2.3 Fit to target mass distribution

The most likely mass distribution found by the algorithm is obtained by breaking down the volume of the sphere in cells and calculating the average mass from the ensemble in each cell at all depths. This follows from the argument that the models contained in the ensemble are sampled with a frequency representative of the posterior probability. Figure 2.9 shows the comparison between the target model and the mean of the ensemble. The output or mean model contains prominent positive masses near the center of the location of target caps, but they are often surrounded

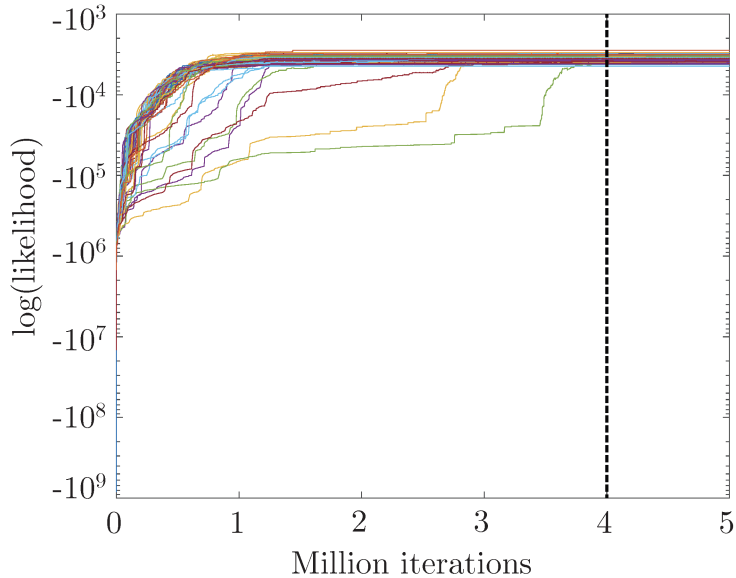


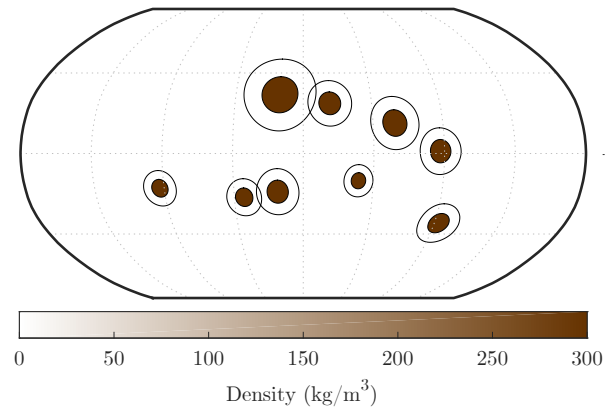
Figure 2.8: Evolution of the likelihood of models found by each of the 100 independent Markov chains. Each point on represents the likelihood of the density model $\{p_m\}$ accepted at each iteration. As the number of iteration increases, all the chains converge to similar likelihood values. Models after 4 million iterations are regarded as having converged and are sampled (one out of every 1000 model) to form the ensemble used to compute the most likely density model.

by a ring of negative masses. This was not expected since the target model contains only positive density anomalies.

The negative mass anomalies that appear in Figure 2.9 could have one of two different origins.

- 1) Parsimony of the algorithm encourages the model to match the gravity signature of spherical caps with fewer masses than would be needed to cover the entire spherical cap. Instead of uniformly distributed positive mass anomalies where there is a positive density in the target model, the algorithm uses negative masses to sharpen a broad positive gravity signal. A schematic of this phenomenon is shown in Figure 2.10. A well-chosen distribution of positive and negative point masses produces a boxcar-shaped anomaly that resemble the expected signal at

a) Target density distribution



b) Output mass distribution

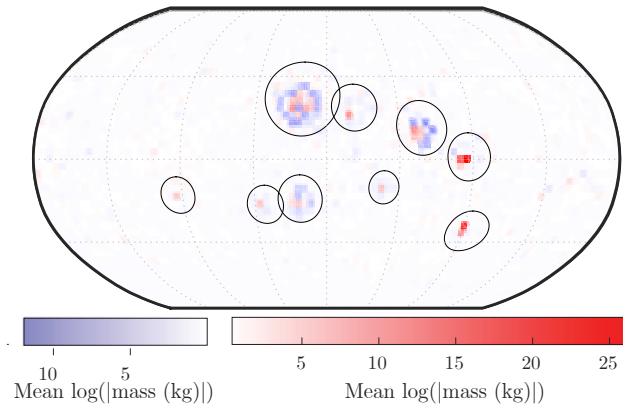


Figure 2.9: Comparison of the target density model (a) with the location of the point mass anomalies of the mean of the ensemble (b). In map b), negative anomalies are plotted using the blue colorbar while positive anomalies the red one. The locations of positive mass anomalies in the output model match the center of the mascons in the target model. However, their outlines are not perfectly circular and most are surrounded by a ring of negative anomalies. The black circles outline the basins that motivated the density anomalies in the target model; they are shown for reference but are not part of the inversion.

the cost of a slightly larger *a posteriori* variance. This interpretation is further supported by a pair of additional synthetic tests we carried out. When inversion is performed on data computed at an elevation of 100 km above the surface, but otherwise identical to those described thus far, the ensemble mass distributions shown in the top panel of Figure 2.11 no longer show the rings of negative mass anomalies. This is because the additional distance suppresses high wavenumber features of the mascon gravity data – those arising from the sharp edges shown in Figure 2.10 – more than the low wavenumber ones corresponding to smooth variations. Similarly, when we increase the maximum allowed value of the noise to 10^{-8} , we allow the inversion to ignore smaller amplitude features, such as those due to the edges; the resulting mass anomalies also no longer show the rings of negative mass, as seen in the bottom panel of Figure 2.11.

- 2) Since models from consecutive iterations differ from each other only in the location or magnitude of a single anomaly, it is possible that the algorithm first finds a large, deep positive mass that improves the residual very much. This mass becomes almost impossible to delete because of its effect on the residual and, instead, later models are improved by adding the negative point masses. In essence, the algorithm remains at a local misfit minimum. However, the stochastic acceptance probability adopted in our algorithm and the presence of 100 independent McMC should prevent this kind of effect from dominating the ensemble solution. Therefore, it is most likely that the imperfect distribution of density anomalies returned by our inversion technique is due to the parsimony inherent to THB

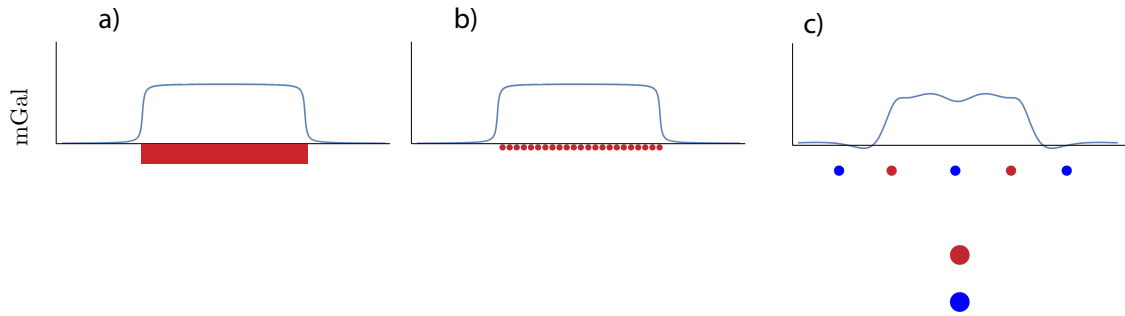


Figure 2.10: Gravity acceleration produced by different mass distributions. The dots show the location of the point mass anomalies, the size indicates relative magnitude of the mass anomaly, and the color indicates whether they represent mass surplus (positive mass anomaly, red) or deficit (negative mass anomaly, blue). The blue line shows the values of the gravitational acceleration produced by the point masses. a) Gravity acceleration produced by the target model which is a density anomaly of finite extent. b) Gravity acceleration due to many positive point masses can match the gravity acceleration produced by the density anomaly shown in (a). c) The gravity acceleration in (a) can be approximated with fewer point masses including both positive and negative ones. An inherently parsimonious algorithm would prefer the simpler model comprising fewer point mass anomalies provided that the fit to the data is sufficiently good. This is our explanation for why parsimony can introduce negative mass anomalies into our ensemble solution.

algorithms.

Another way to compare the inversion result and the target models is to examine the posterior probability distributions computed from the ensemble, which shows the relative frequency of models in the ensemble having certain value of a parameter or a combination of parameters. The credible region of these parameters is calculated as the region where 68% of the posterior probability is located, in a similar fashion than results shown in a 1σ confidence intervals. Figure 2.12 shows the posterior probability of the location of anomalies and their credible region. Peaks of probability match the true location of the center of mascons, which means that the algorithm effectively recovers the value of these parameters. Figure 2.13

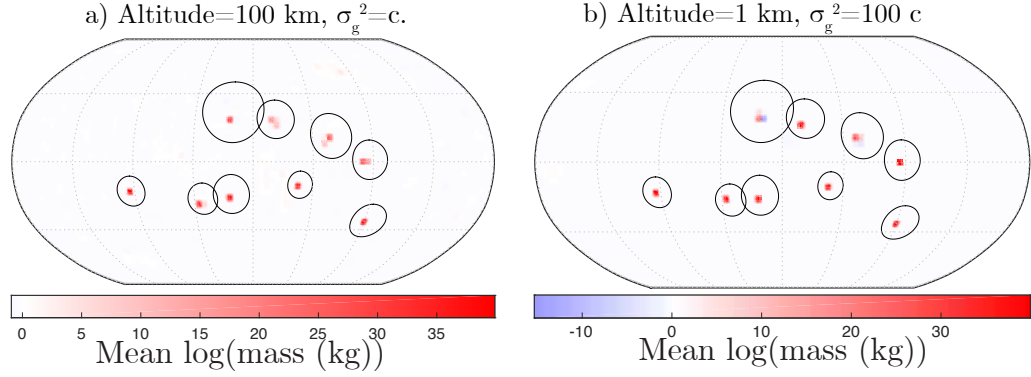


Figure 2.11: Effect of observation height and noise hyperparameter on retrieval of mass anomalies. Same as Figure 2.9 but with (a) synthetic gravity data computed at 100 km elevation above the surface instead of at the surface, and (b) 100 times larger noise variance hyperparameter. Note the disappearance of negative mass rings visible in Figure 2.9

shows the posterior probability distribution of mass anomaly depth, $P(\{r\}|\{g\})$.

The posterior probably features a marked preference for anomalies at very shallow depth, around the correct depths of $0.97 \leq r \leq 0.99$ which are the same limits the spherical caps in the target model have. This distribution extends deeper than this limits, probably again as a result of the parsimony of the algorithm that can adjust the shape of the gravity anomalies by including deeper point masses (Figure 2.10). The credible region is limited by $r \gtrsim 0.87$, which includes the correct value of the target model.

The value of the noise variance is overestimated by the algorithm: $10^{-10} (\text{m/s}^2)^2$ instead of $10^{-11} (\text{m/s}^2)^2$ in the target model. When we repeat the inversion increasing the maximum value of the prior on the noise hyperparameter, the algorithm returns the highest possible value $10^{-8} (\text{m/s}^2)^2$. This implies that the true value of the noise variance is too small to be recovered since it is swamped by the large modeling error of using the point mass parameterization to represent objects of finite

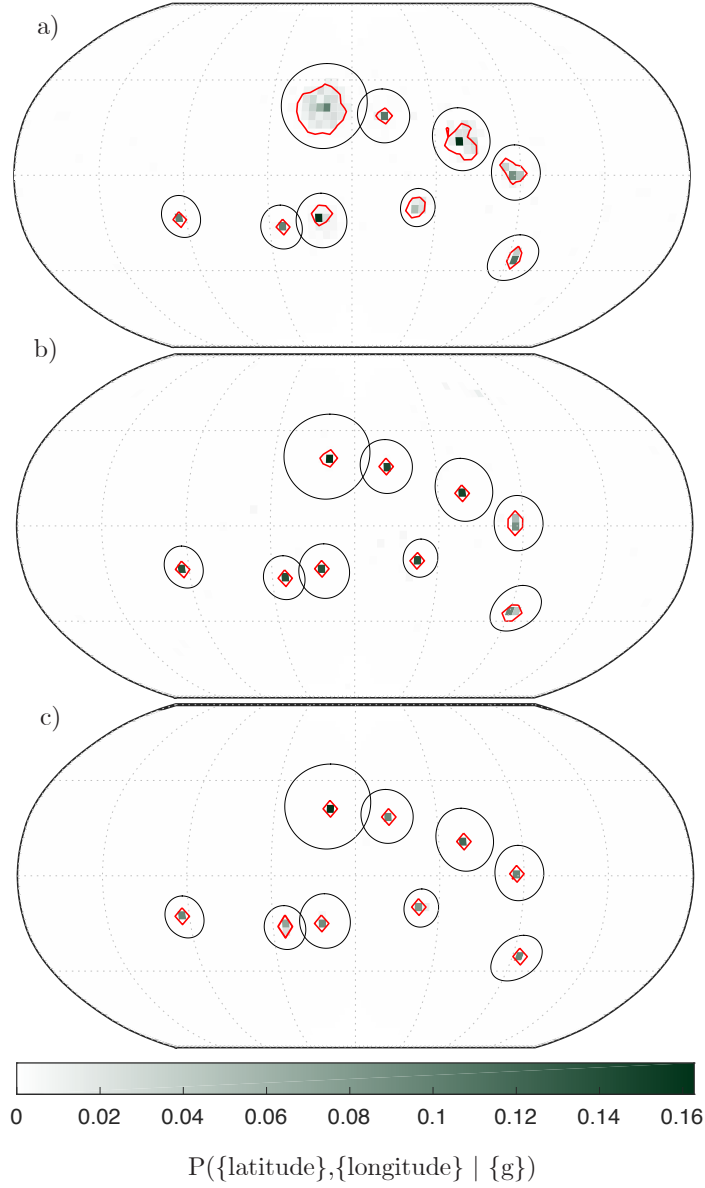


Figure 2.12: Posterior probability of the latitude and longitude of mass anomalies for three inversions: a) standard inversion (Figure 8); b) inversion of the gravity data observed at 100 km height; and c) inversion with large noise hyperparameter allowed. The red contours outline the regions where the 68% probability region is located. The anomalies are fully contained inside the basins where the target mass anomalies are specified (black circles). Recovery of true center positions of the input mascons improves when higher altitude gravity observations are used -since they have longer wavelength gravity variations- and when larger noise hyperparameter values are allowed -since they allow the inversion to neglect fitting the sharp corners of the mascon gravity data. [2.10](#)

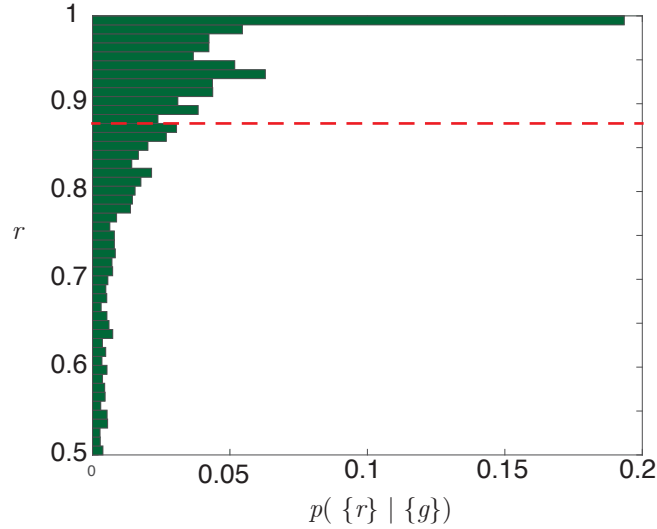


Figure 2.13: Posterior probability distribution of point mass radius r . The mass anomalies in the target density model have $r = 0.99$ for the outer shell and $r = 0.97$ for the inner shell. The most likely r matches the target value and it is contained in the 68 % credible region limited by the red line.

size.

The most likely value of the number of anomalies n is 60 with a range between 50 and 73 contained in the 68% credible interval. Although this lacks physical meaning since the true density model is not made of point masses, this shows an important characteristic of the algorithm. The fact that most models have 60 anomalies, less than maximum number allowed (140), shows that the algorithm is indeed parsimonious, as designed. It matches the true gravity data with fewer number of anomalies than the ones it could use.

2.4.2.4 Uncertainty related to point mass parametrization

In section 2.4.2.3 we described how the output mass distribution model or the mean of the ensemble has patterns of negative and positive rings of point mass anomalies where the spherical caps of the target model are located. This shows

that using point masses in the THB algorithm contributes to the uncertainty in the interpretation of what the actual internal distribution of the mass in a body is. If the output mass distribution model is given by figure 2.10 c), for example, the actual mass distribution of the interior of the body could be the ones shown in figure 2.10 a) or 2.10 c). Additional constraints might help distinguish between them but, in the absence of such constraints, all these possibilities must be considered. Uncertainty on the inversion results is higher than if instructive a priori constraints were used, as in the case where mass anomalies are restricted to a given depth representing, say, the crust-mantle interface. However, in the absence of independent constraints, our approach provides a more complete estimate of the actual uncertainty.

2.5 Discussion

Our validation tests show that while the location of mass anomalies can be readily recovered by the THB method, their detailed shape cannot be confidently estimated when the input gravity data is produced by finite-sized objects. Additionally, we find that the parsimonious nature of the algorithm can cause spurious negative mass anomalies to be introduced into the ensemble solution when the point mass anomaly parameterization is used. There are, nevertheless, important advantages of using our THB method compared to current TB gravity inversion ones [28, 29] since our THB method recovers a global mass distribution model, instead of a local density distribution and it explores a larger model space with many possible combination of magnitude, location and number of anomalies. The global approach is

necessary for the detection of deep anomalies inside celestial bodies since it does not restricts the size of possible density anomalies and provide more flexibility in their location while local inversions imposes prior constraints even when there is not a good argument for them.

The drawbacks of the THB method described in this chapter can be addressed by increasing the complexity of the model parameterization. In particular, we consider finite size objects instead of point masses in chapters 3 and 4. In chapter 3 we describe the modifications of the THB algorithm necessary to use these objects and to make it more efficient in order to balance the increase in time per iteration.

2.6 Conclusion

This study presents a Transdimensional Hierarchical Bayesian algorithm for the inversion of gravity data. This method uses a point mass parameterization, non informative priors, and a larger model space than previous transdimensional Bayesian gravity inversion methods. In order to reduce the number of iterations needed to achieve convergence, an optimization of the magnitude of point masses is applied. A new acceptance probability α that takes into account this optimization is derived.

The performance of the algorithm is assessed through a series of validation inversions which aim to recover a target mass distribution model that contains either point mass anomalies or three-dimensional objects of constant density anomaly.

The algorithm is able to match perfectly the target model in which the gravity

signatures of all point mass anomalies have similar values and are well separated from each other. When the gravity acceleration data is dominated by the signature of fewer point masses than the total number contained in the target model, the algorithm tries to fit only those dominant masses. This is a consequence of parsimony and the transdimensionality of the algorithm. In the second set of inversions, the algorithm finds the correct latitude, longitude and depth of the center of massive spherical caps but fails to find their outline. Instead the model includes a ring of negative masses and some deeper masses to sharpen the gravity data to better match the the input. For all the tests for which the target model is build from point masses, the algorithm finds the correct noise variance. However, if the target model contains finite size objects, like spherical caps, the variance increases during the inversion above the data uncertainty because of the addition of modeling error arising from the use of point masses and the parsimony of the algorithm. A parameterization based on finite size object such as spherical cap may be better able to recover target models that contain three-dimensional density objects.

Chapter 3: Spherical caps as parametrization of density anomalies in global gravity inversions

3.1 Abstract

The shape, magnitude and location of density anomalies below impact basins of the Moon help constrain the present state of compensation of the basin region and properties of the lithosphere at the time of the impact. In order to constrain these density anomalies we build on the gravity inversion algorithm from Izquierdo *et al.* [41] using a spherical cap parametrization of the anomalies. The amount of uplift of the core-mantle boundary, for example, could be constrained by the thickness of the caps and the size by their aperture. With this approach, called THEBOOGIE, we can constrain the density anomalies related to crustal thinning below basins and also anomalies occurring at other locations, without assuming all the gravity signal comes from variations of crustal thickness. It also provides the additional advantage of showing the range of variation of model parameters that fit the data in order to analyze if they can be confidently constrained or not. We construct a target model of two spherical caps and use the gravity acceleration data produced by it as input in the inversion. The results show that the method is able to find

the values of the latitude, longitude and aperture of both caps in the target model very well and with a small uncertainty. The depth, thickness and corresponding density of the caps in the mean model have tradeoffs because of the non-uniqueness of gravity inversions, however, this non-uniqueness is quantified and informs about upper limits of the values of these parameters. The calculation of the gravity field of density models using this parametrization is slow and grows with increasing number of caps. Future improvements to the efficiency of the algorithm are needed before this parametrization can be used in the inversion of realistic planetary gravity fields.

3.2 Introduction

The density distribution within a planetary body is the result of its thermal and compositional evolution. Satellite gravity data is sensitive to the lateral variations of this density distribution and has been used extensively to constrain planetary interiors, specially to infer lateral variations of crustal thickness [9, 10, 42, for example]. The Bouguer gravity data shows the gravity acceleration produced by material below a reference radius, after the signal related to topography is removed [43]. A region with a thinner crust produces a positive Bouguer anomaly because it has more high density mantle material and less low density crustal material than a region with a thicker crust. Figure 3.1 shows the Bouguer gravity field of the Moon obtained by Lemoine *et al.* [44]. Many circular features have a positive Bouguer anomaly. These features are impact basins. Near side basins have a specially large positive Bouguer anomaly, between 500 and 1000 mGal.

The crust at the location of impact basins is generally thinner than its global mean value because the impactor removes surface material of a planetary body at the time of the impact and posterior isostatic compensation makes the crust-mantle interface shallower in the basin region [39]. The amount of mantle uplift underneath an impact basin is an important parameter to constrain because it shows the present state of isostatic compensation of the Moon in the corresponding region. This state of compensation can be related to the past condition of the lithosphere at the location of the basins, for example, how strong the lithosphere was at the time of the impact [45].

Melosh *et al.* [46] modeled the impacts and subsequent evolution of the Freundlich-Sharonov and Humorum basins using different impactor energies, lunar thermal gradients and amounts of volcanic fill. According to this study, the lithosphere of the Moon has to be strong enough so support a super-isostatic state of compensation. The lithosphere in this state would sustain an excess of mass that produced a gravity signal matching the observed Bouguer gravity acceleration data in those regions.

Density anomalies are not only related to variations of crustal thickness. Density anomalies might exist within the crust, upper, mid and deep mantle. Crustal thickness estimation methods might map these anomalies as mantle uplift if it is assumed all Bouguer signal comes from variations in crustal thickness. It is necessary to study all possible distributions of 3-D density anomalies within a body that fit the Bouguer gravity data in order to infer correctly the thickness of the crust and the densities of the crust and mantle. Even if most of the Bouguer gravity signal in a region comes from variations in the thickness of the crust, the part of the signal

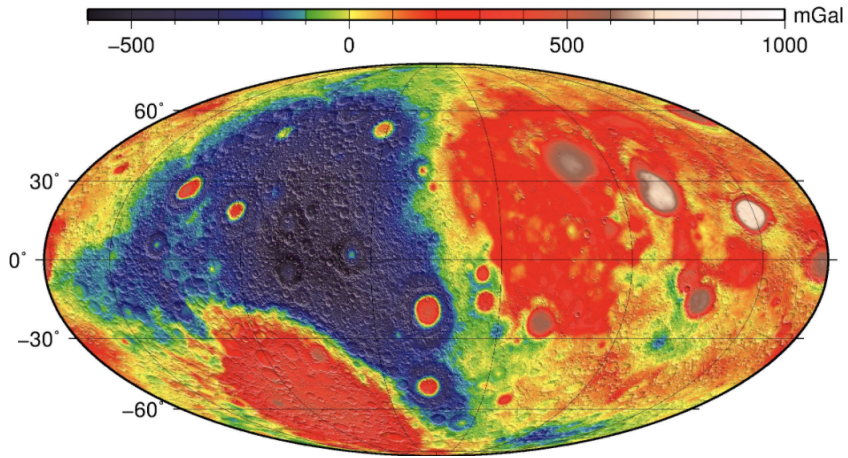


Figure 3.1: Bouguer gravity anomaly of the Moon (orders 1-700) from Lemoine *et al* [47]. The acceleration is produced by the distribution of density inside a reference radius of $R = 1739$ km . The acceleration due to topography is removed.

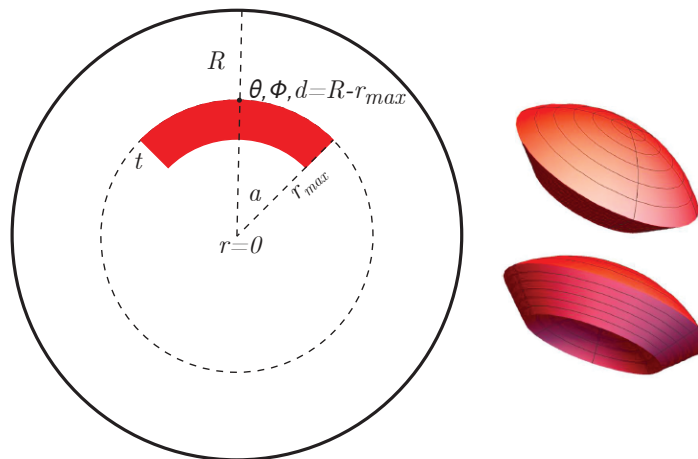


Figure 3.2: 2-D and 3-D representation of a spherical cap. The parameters that define a spherical cap are its density ρ , aperture a , thickness t , depth of outer shell d , longitude ϕ and latitude θ of its center. R is the radius of the planetary interior and r_{max} is the radius of the outer shell of the cap. Figure duplicated from chapter 1 for convenience.

that might come from deeper or shallower locations might be incorrectly mapped to the crust-mantle interface and the properties of the body inferred from this interface might be incorrect.

In this chapter, we build onto the Transdimensional Hierarchical Bayesian method described by Izquierdo *et al.* [41] and incorporate a three-dimensional parametrization of the density distribution inside a sphere using spherical caps to represent density anomalies or density variations from a mean value. Prior information used in this method can be non-informative. For example, anomalies can be located anywhere in the sphere, not only in the core-mantle interface and the number of caps to find inside a sphere is not fixed *a priori* but inferred from the data. The method provides the range of parameter values of density models that fit the observed gravity data, from which uncertainty information can be calculated. The uncertainty information is essential in gravity inversions because different density models can match the gravity data and the significance of a density value in a region depends on how unique or non-unique it is [48].

A spherical cap is an ideal candidate to represent the density anomaly related to an impact basin because the mantle uplift in the circular basin region can be represented by the thickness t and aperture a of the cap. Figure 3.2 shows the schematics of 2-D and 3-D spherical caps. They are completely defined by the parameters: density ρ , aperture a , thickness t , depth of upper shell d , longitude ϕ and latitude θ of center.

This chapter first describes the inversion algorithm using spherical caps (section 3.3). Then describes the validation of the algorithm with the inversion of syn-

thetic gravity data (section 3.4) and finally presents a discussion of the advantages and disadvantages related to other methods and other parametrizations (section 3.5)

3.3 Gravity inversion method

Figure 3.3 shows a flowchart of the algorithm used in this chapter. The central part of the algorithm is the construction of a Markov chain [30] linked to a Transdimensional Hierarchical Bayesian (THB) inversion method. The method is transdimensional because the number of spherical caps in the interior of the sphere is not fixed *a priori* but, instead, is a parameter to be constrained by the input gravity data. It is hierarchical because the noise variance is also unknown and estimated including the modeling error [32] and Bayesian because it uses Bayes' theorem to compare pairs of models and choose the one that best represents the interior of the sphere based on the input data and, if desired, additional constraints.

Since a density anomaly is represented by the shape, size and location of an object, in this case a spherical cap, this inversion approach is an object-oriented approach. Point masses are not used in an object-oriented approach because parameters of a density anomaly are represented by a distribution of point masses. We called this algorithm, THEBOOGIE or Transdimensional Hierarchical Bayesian Object-Oriented Gravity Inversion.

$$m = n, \{\rho\}, \{a\}, \{t\}, \{d\}, \{\phi\}, \{\theta\}, \sigma_g^2 \quad (3.1)$$

At each iteration, there is an accepted density model m and a proposed density

model m' . Equation 3.1 shows that a density model m is defined by the number of caps inside the sphere n , their density $\{\rho\}$, aperture $\{a\}$, thickness $\{t\}$, depth of upper shell $\{d\}$, longitude $\{\phi\}$, latitude $\{\theta\}$ and noise variance of the input data σ_g^2 where the curly brackets denote vectors of size n . The noise variance of the input data is a parameter of the model because σ_g^2 combines the error on the measurements of the input gravity data and the modeling errors caused by the parametrization [32,33].

The values of the parameters of the initial density model m (at iteration $i = 1$) are obtained by sampling uniform distributions with the limits shown in table 3.1. These distributions are called prior distributions because it reflects our knowledge of the interior before inverting the gravity data. The priors are non-informative because they only require the spherical caps to be located inside the sphere and to have a density anomaly that is physically possible. Material with a density anomaly outside the range of -500 and 500 kg/m³ from the mean density value of the Moon are not likely to exist within the Moon.

The proposed model m' is obtained by randomly making one modification to the accepted model m . Figure 3.4 shows the possible modifications and how the proposed model would look compared to the accepted model. There are five possible changes to make: change the aperture of cap i , change the thickness of cap i , change the location of of cap i , delete cap i , add a new cap to the density model or change the noise variance. The change to make is chosen randomly and so is the cap i that is modified. After one of these changes is applied, the density of the caps in model m' is linearly optimized to reduce the misfit between the gravity acceleration

	Lower limit	Upper limit
Density (kg/m ³)	-500	500
Aperture (°)	0	180
Thickness (km)	0	1409 km
Depth (km)	0	1409 km
Longitude (°)	0	360
Latitude (°)	-90	90
Noise variance (mGal ²)	1×10^{-4}	1

Table 3.1: Prior information of model parameters. All the priors distributions are uniform with non-informative limits. Spherical caps are limited to be located within the sphere, between radius $r = 330$ km and $R = 1739$ km. $r = 330$ km is chosen as lower limit of r because it is the location of the core-mantle boundary of the Moon.

produced by m' and the input gravity acceleration. Model m' is then completely defined.

After the proposed model is computed, its gravity acceleration data is calculated and used to compute its likelihood ($P(\{g\}|m')$). The expressions for the likelihood, acceptance probability and their derivations from Bayes' theorem are shown by Izquierdo *et al.* [41] and only summarized here. The likelihood of a model m is given by equation 3.2 where n is the number of spherical caps, s is the number of gravity data points and Φ is the residual. \tilde{C}_m is the posterior model covariance matrix, $\tilde{C}_m = (D^t C_g^{-1} D + C_m^{-1})^{-1}$ [25] where D is a matrix constructed using the gravitational constant G and inverse of the distances between the center of the caps and the observation points. C_g is the data covariance matrix ($C_g = \sigma_g^2 I$) and C_m is the prior model covariance matrix. C_m is assumed to be a diagonal matrix since there is no reason to assume different caps are correlated.

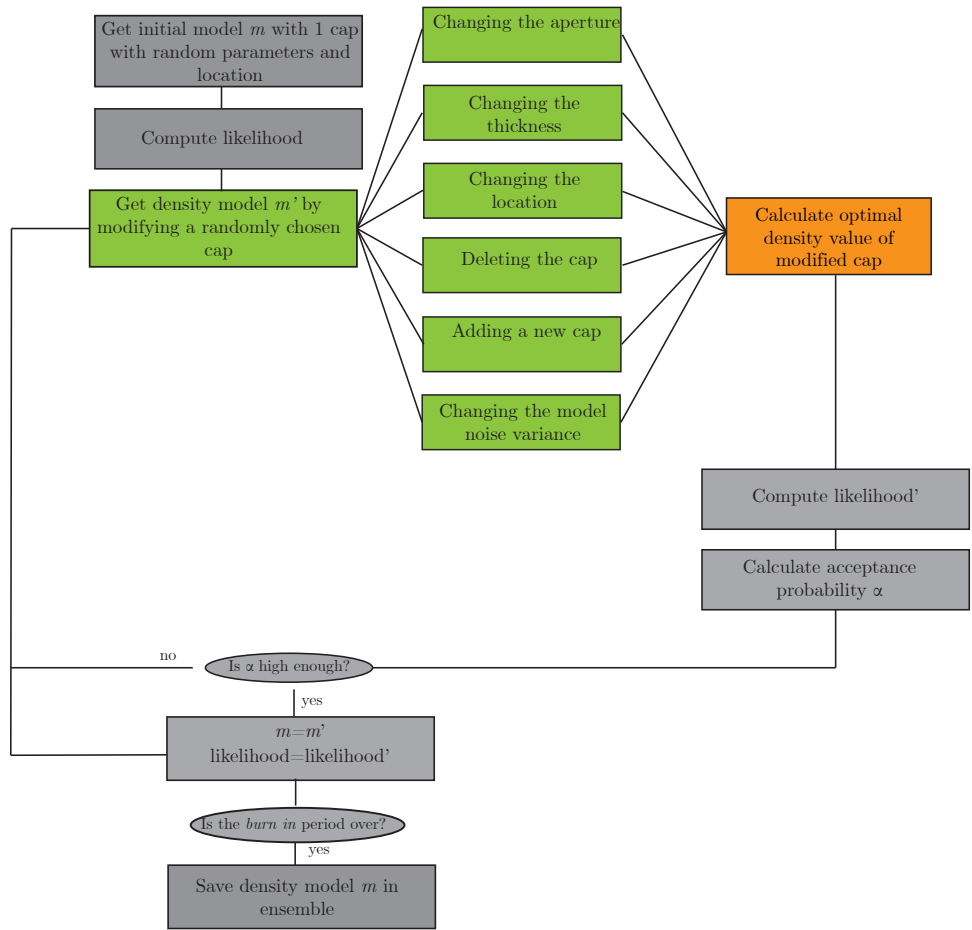


Figure 3.3: Flowchart of the gravity inversion algorithm called THEBOOGIE. Steps necessary to propose a new density model are highlighted in green and orange. Parameters of the new density model obtained from a random walk are highlighted in green while the one obtained from a linear optimization (the density of each cap) is highlighted in orange.

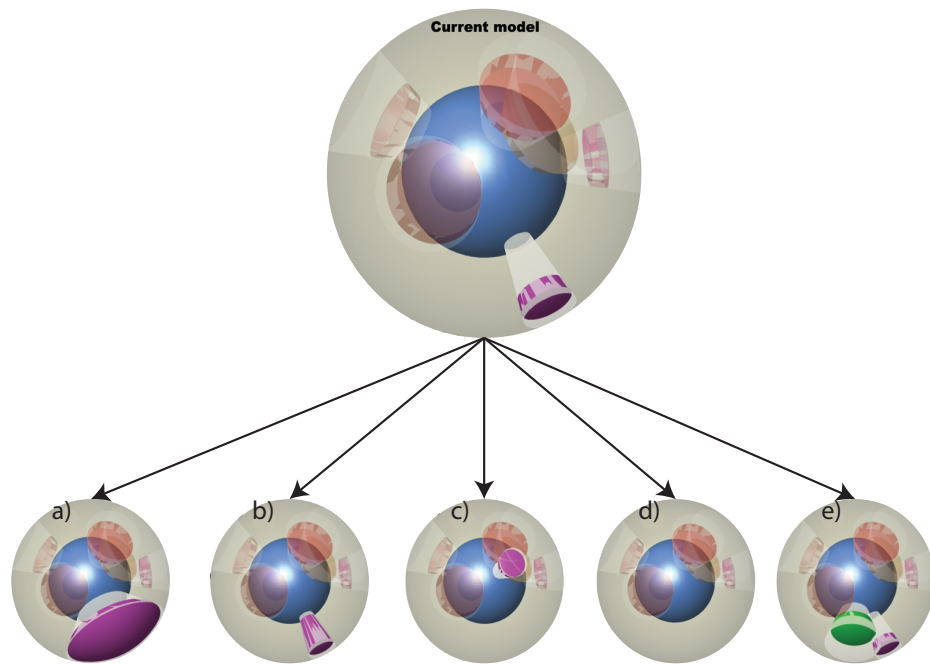


Figure 3.4: Current density model and possible modifications to obtain next proposed density model . The blue sphere represents the core of the Moon. Six caps, each of different position, depth, aperture, and density (represented by the color) make up the current model. Of these, only the one highlighted in purple is modified in this example. It is possible to modify: a) the aperture of the cap; b) the thickness of the cap; c) the location of the cap. In addition, d) the cap can be deleted and e) a new cap (green) can be added. Not visualized: the variance of the data can be changed.

$$P(\{g\}|m) = \frac{\sqrt{|\tilde{C}_m|}}{(\sigma_g^2)^s (\rho_{\max} - \rho_{\min})^n} \exp\left(-\frac{\Phi}{2}\right) \quad (3.2)$$

The residual is given by equation 3.3 where $\{g\}$ is the input gravity data and $\{g_m\}$ is the gravity data of density model m .

$$\Phi = (\{g\} - \{g_m\})^T \frac{1}{\sigma_g^2} (\{g\} - \{g_m\}) \quad (3.3)$$

After the likelihood of model m and m' is computed, an acceptance probability α is assigned to model m' . Equation 3.4 shows the expression of the acceptance probability α . This probability is a function of the ratio of likelihood of the proposed model and the likelihood of the accepted model. If the proposed model has a much larger likelihood than the accepted model, then its acceptance probability is high and the proposed model might replace the accepted model m . The probability of accepting model m' increases if its residual or noise variance decreases compared to the values of model m , the determinant of the model covariance matrix increases or if model m' has a fewer number of spherical caps, keeping everything else constant.

$$\alpha = \min \left[1, \left(\frac{\sigma_g^2}{\sigma_g'^2} \right)^s \exp\left(-\frac{\Phi - \Phi'}{2}\right) \sqrt{\frac{|\tilde{C}_{\rho'}|}{|\tilde{C}_\rho|}} (\rho_{\max} - \rho_{\min})^{n-n'} \right] \quad (3.4)$$

The process of proposing and accepting models is done at each iteration of the THB algorithm. Not all accepted models are part of the group of output models, however. The first accepted model (at iteration 1) is randomly chosen so it most likely has a very bad fit to the gravity data. Even if the model at iteration 2 has a

better fit to the data, the fit might still be poor. Only after convergence is achieved, the accepted models would be a representative sample of the parameters that fit the input gravity data. Convergence is said to be achieved when the values of likelihood (Equation 3.2) do not change much per iteration compared to the variations observed in the initial iterations. The accepted models m obtained during the initial iterations have very different values of its likelihood and they are not part of the output models. This initial period of iterations is called burn-in period.

3.3.1 Gravity acceleration of a spherical cap

The gravity acceleration produced by a spherical cap of density ρ at a set of 2562 points $\{r_s\}$ over the surface of the sphere is given by equation 3.5. R is the radius of the sphere, G is the gravitational constant, p_l is the Legendre polynomial of degree l , a is the aperture of the cap and β is the angle between the observation point and the center of the cap [49].

$$\{g_{cap}\} = 2\pi\rho G \sum_{n=0}^{\infty} \frac{R_{\max}^{l+3} - R_{\min}^{l+3}}{(2l+1)(l+3)R^{l+2}} (l+1)[p_{l+1}(\cos(a)) - p_{l-1}(\cos(a))]p_l(\cos(\beta)) \quad (3.5)$$

At each iteration of the algorithm, the gravity acceleration $\{g'\}$ produced by the proposed density model m' is calculated by adding equation 3.5 n times each time for each cap in the model. The Legendre polynomials are calculated in an iterative way and the time it takes to calculate this gravity data scales linearly with the number of spherical caps of model m' . These two factors make the calculation of $\{g'\}$ the most time-consuming operation in the THB algorithm with a spherical

cap parametrization. The density ρ of each cap needed to compute equation 3.5, is obtained by a constrained linear least-squares optimization where the value of ρ that reduces the residual Φ is obtained bounded to the limits of -500 and 500 kg/m³. This optimization of the density is the second-longest process in the algorithm. For an inversion of 2562 gravity data points ran for 100 iterations with an average of four spherical caps per iteration, the percentage of the total time spent on the calculation of the gravity field of the models was 70 % and the percentage spent in the optimization of density was 4%.

3.4 Validation

The gravity inversion method is validated by creating a density model (target model), calculating its gravity acceleration data, inputting this data into the algorithm in figure 3.3 and comparing the mean of the output models obtained with the target model. The Moon is represented by a perfect sphere of radius $R = 1739$ km and mean density of zero. This mean density is set to zero in order to visualize only the density anomalies parametrized as spherical caps. An spherical cap with density of 300 kg/m³, represents an anomaly of 300 kg/m³ over the mean density of the Moon. The target model consists of two spherical caps with a density of 300 kg/m³ located in the surface of an otherwise empty sphere. The gravity field produced by the target model is sampled over 2562 points uniformly distributed at an altitude of 10 km over the surface of the sphere. Noise with variance equal to 1×10^{-2} mGal is added to the gravity data to test if the value of its variance can

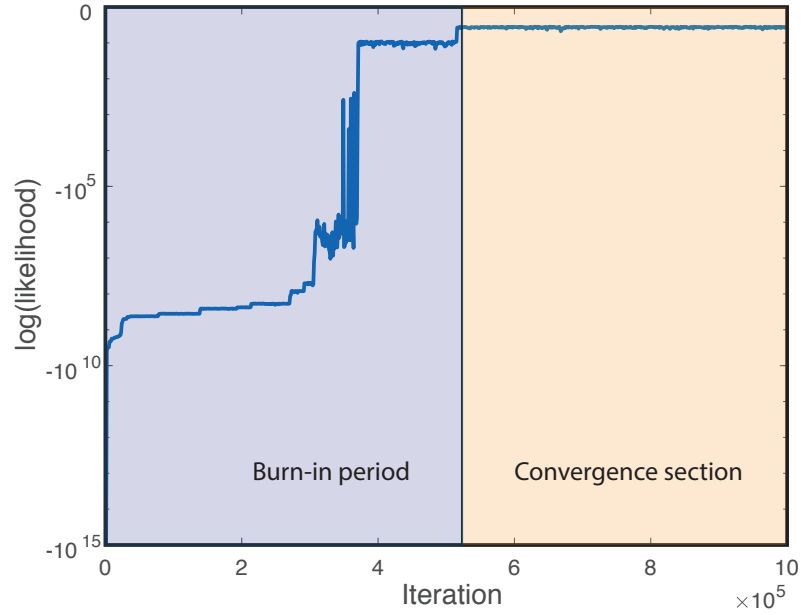


Figure 3.5: Logarithm of the likelihood per iteration. The likelihood increases with increasing number of iterations until it stabilizes around iteration 5.5×10^5 . Accepted models after this point are considered converged models and from part of the output models of the THB algorithm.

be determined by the algorithm.

The THB algorithm was run for 1×10^6 iterations. Figure 3.5 shows the logarithm of the likelihood per iteration or the logarithm of the likelihood of the accepted model at each iteration. There is a large variation of the likelihood during the first half of the run and then the value of the likelihood stabilizes. Convergence is said to occur at iteration 5.5×10^5 and 1×10^3 density models obtained after that iteration form the output density models or ensemble.

As a first validation criteria, it is necessary to check if the output models fit the input gravity data. Figure 3.6 shows that the mean gravity acceleration of models within the ensemble is very similar to the acceleration of the target model. The

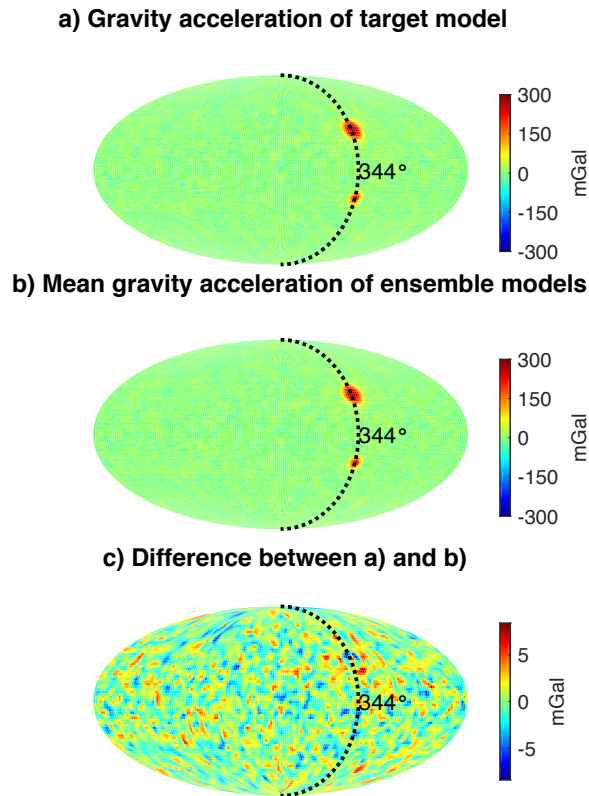


Figure 3.6: a) Gravity acceleration of target model. b) Mean of the gravity acceleration produced by individual density models in the ensemble. c) Difference between gravity acceleration data in a) and b). The differences between the gravity acceleration of the target model (input gravity) and the mean gravity of the output models is relative small. This shows that the THeBOOGIe is able to find an ensemble of density models that fit the data.

maximum misfit is less than 8 mGal. The small residual indicates that the inversion algorithm described in figure 3.3 is able to find a group of density models that fit the input gravity data.

The second validation criteria is to check how similar is the mean density model from the target model. As mentioned before, the THB method does not solve the non-uniqueness of gravity inversions but has the advantage of quantifying how much variation in the parameters is allowed by the input gravity data. Therefore, a mismatch between the mean and the target model does not indicate a failure of the THB inversion method but, instead, shows which parameters of the target model can be uniquely constrain with the input gravity data and which ones cannot.

The target model consists of two spherical caps with different latitudes, longitudes and apertures. Both caps have a density anomaly of 300 kg/m^3 , a thickness of 20 km and their outer shells are located at the surface of the sphere. The sphere has radius $R = 1739 \text{ km}$. The gravity data produced by the target model is the input data of the inversion algorithm and it is shown in figure 3.6 a). Tables 3.2 and 3.3 show the mean value of the model parameters in the ensemble, their standard deviation and the values of the target model. The mean density is the model with parameters values given by the mean of the parameters in the ensemble.

Figure 3.7 shows an upper view of the mean density model, the target model and the difference between the two. In order to visualize the density of the mean model in this figure, the density of all models in the ensemble are averaged in a 2-D grid of 0.1° in latitude and longitude. It is clear that the algorithm is able to fit very well the latitude and longitude of the center of the caps and their aperture. It

	Mean value of ensemble	Standard deviation	Target value
Density (kg/m ³)	444.2	49.8	300
Aperture (°)	7.33	0.06	7.4
Thickness (km)	14.7	2.1	20
Depth (km)	10.7	1.8×10^{-14}	0
Longitude (°)	344.3	8.5×10^{-13}	344
Latitude (°)	32.5	6.4×10^{-14}	32

Table 3.2: Value of the parameters of the North Cap in the output ensemble and the target model.

	Mean value of ensemble	Standard deviation	Target value
Density (kg/m ³)	321.2	75.3	300
Aperture (°)	4.7	0.08	4.7
Thickness (km)	20.1	5	20
Depth (km)	1.1	4.2×10^{-15}	0
Longitude (°)	343.4	9.7×10^{-13}	343
Latitude (°)	-21.2	5.3×10^{-14}	-21

Table 3.3: Value of the parameters of the South cap in the output ensemble and the target model.

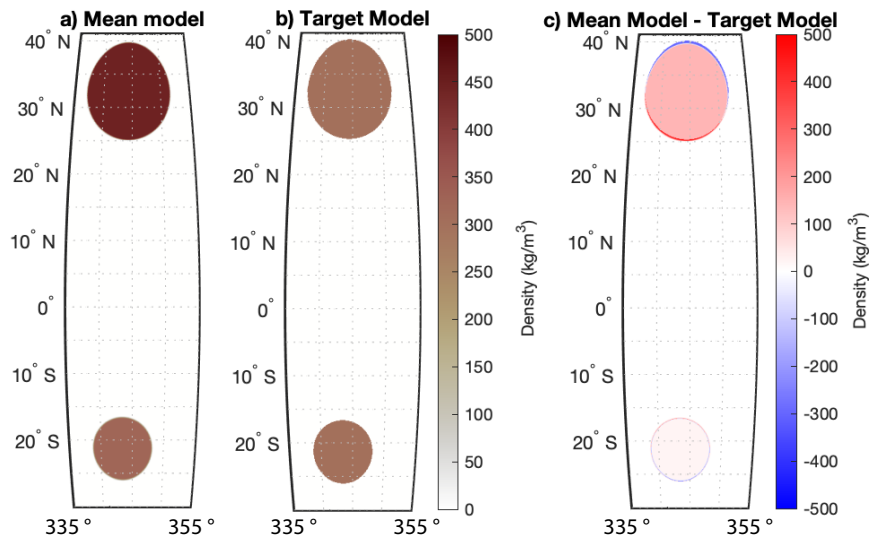


Figure 3.7: a) Upper view of the mean density model with density values at all depths within the ensemble averaged on a 2-D grid of 0.1° in latitude and longitude. The north cap has a mean density of 444.2 kg/m^3 while the south cap has a mean density of 321.2 kg/m^3 . b) Target model contains two caps with densities of 300 kg/m^3 . c) The difference between the mean and target model show that the inversion algorithm estimates the lateral location of the cap very well (latitude and longitude of center and aperture) while the density of both caps are overestimated. The north cap by 48 % and the south cap by 7%.

is also clear that the density of the caps in the mean model is larger than in the target model which means that this parameter was overestimated by the inversion. The north cap has a mean density of 444.2 kg/m^3 and the south cap of 321.2 kg/m^3 corresponding to overestimates of 48% and 7%, respectively, over the target model density anomaly of 300 kg/m^3 . Since the fit to the input data is good, the excess of density should be compensated by the mean model by having deeper or thinner caps than the target model.

Figure 3.8 shows a slice of the density distribution of the mean model, target model and the difference between them. The mean model plotted in this figure is obtained by averaging the density values of all models in the ensemble in a grid of 0.1° blocks in latitude and 2 km in depth. The slice is taken at longitude $\Phi = 345^\circ$. This figure shows that the north cap is much thinner and deeper in the mean model than in the target one. The south cap in the mean model is deeper than in the target model too but it is not necessarily thinner. Most of the density is concentrated in a thinner cap while there is a spread of density values in deeper locations. The spread or fuzziness in the boundaries of the caps in figure 3.7 is due to the fact that the depth extent of the caps varies between different models in the ensemble, even though each cap has uniform density. By contrast, the lateral and top boundaries of the density anomalies in the mean model, are sharp. This shows that the thickness of the caps is less well constrained than their lateral location.

Figure 3.9 shows histograms of the values of density, aperture, thickness, depth, longitude and latitude of all models in the ensemble. This distribution of values is complementary information from the mean model and is specially suited to make a

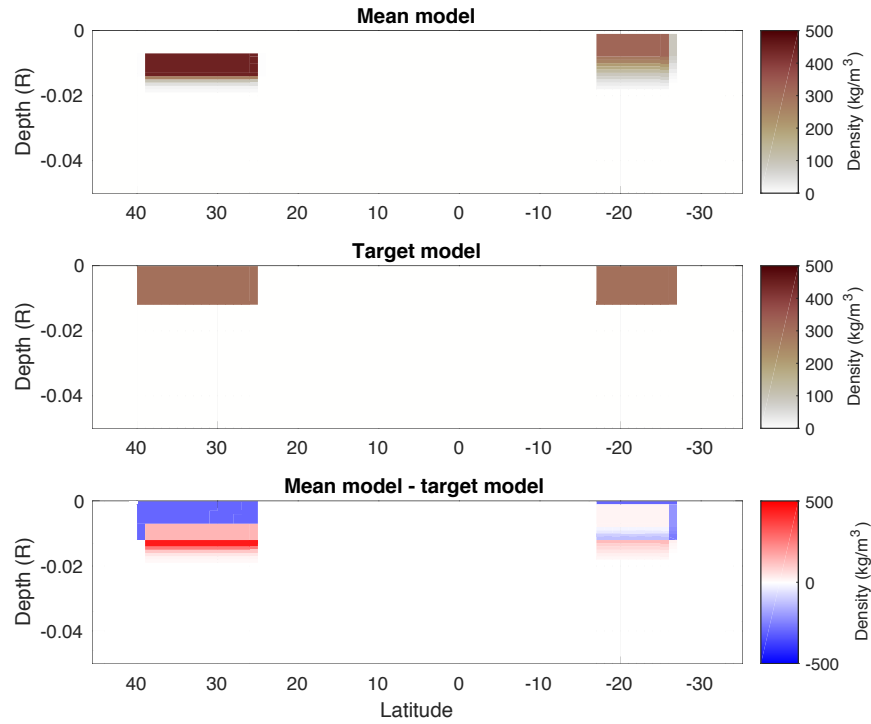


Figure 3.8: Slice of the mean model, target model and difference between depth at longitude $\Phi = 345^\circ$. a) Output of mean density model. The outer shell of the north cap (left) has a depth of $0.016R$ while the one from the south cap (right) has a depth of $0.010R$ where R is the radius of the Moon. b) Both caps in the target model have an upper shell at 0 depth. c) The difference between the mean and target model shows that the inversion algorithm overestimates the depth of both caps. The north cap in the mean model is 27 km deeper than in the target model while the south one is 17 km deeper. The fit to the gravity field is very good because the lateral location and size of the cap is recovered very well and the excess of density is compensated by the deeper location of the caps.

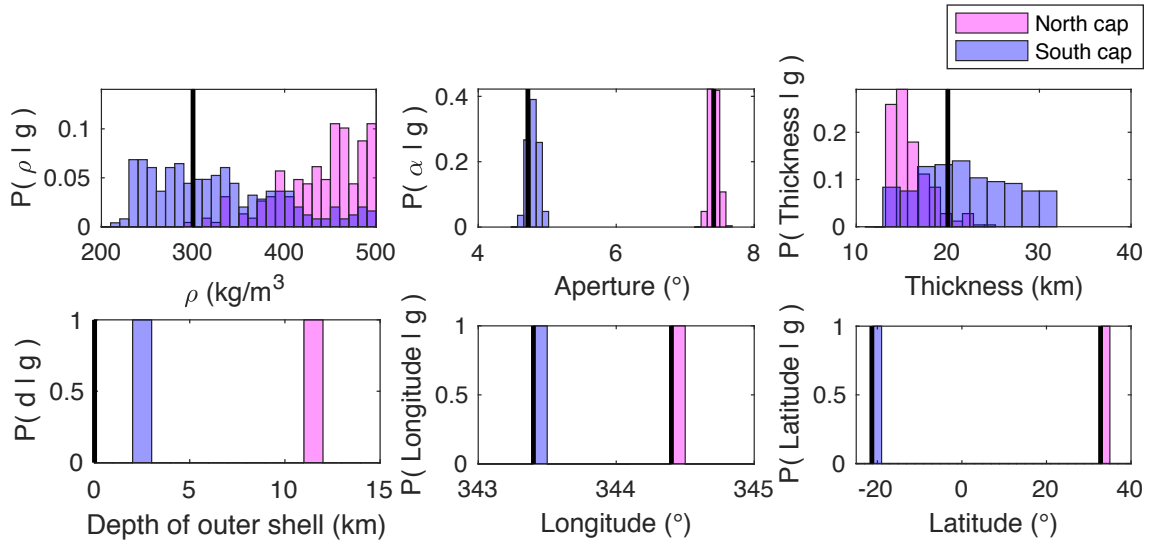


Figure 3.9: Distribution of model parameter values within the ensemble. The black vertical lines show the corresponding value of each parameter in the target model. The aperture, latitude and longitude are very well constrained since most or all models in the ensemble match the values in the target model and the variation within models is small. The density (ρ), thickness and depth are less well constrained because the spread of values is larger and the peak of the distribution is not located at the corresponding value in the target model. There is a trade-off between the density, thickness and depth of the spherical caps which is expected for gravity inversions but only quantified in THB inversion methods.

quantitative analysis of the uncertainty or non-uniqueness of each parameter. The aperture, latitude and longitude have a spread of less than 1° and they all have their distribution peaks located at the values of the respective parameter in the target model. These parameters are well constrained by the input gravity data.

The density, thickness and depth are not as well constrained as other parameters. Since the density of the caps is calculated once a thickness and depth is specified, there are only two independent parameters that are not well constrained, the thickness and depth. A trade-off between these parameters is expected in all gravity inversions but it is only quantified in THB inversions. There is not much variation in the depth of the caps (less than 1 cm of standard deviation for both) but both caps are located deeper in the sphere than they are in the target model. The variation is much greater for the thickness of the caps (2 and 5 km of standard deviation for North and South cap respectively) which means the algorithm is more likely to change the thickness than changing the depth of the caps.

Figure 3.10a shows the depth of the outer shell of the caps vs their thickness. It shows that the depth value of both caps does not vary much between different density models while the corresponding thicknesses do. As shown in figure 3.4, the depth of the current model is modified in the same step as the latitude and longitude. At certain iteration, the algorithm probably chose a location for a cap that fitted the latitude and longitude of the target model very well while it did not fit the depth as well. In order to modify this depth value, the algorithm had to modify latitude and longitude too because the three coordinates are modified in the same step. The location of the cap stayed fixed because the odds of having an even better

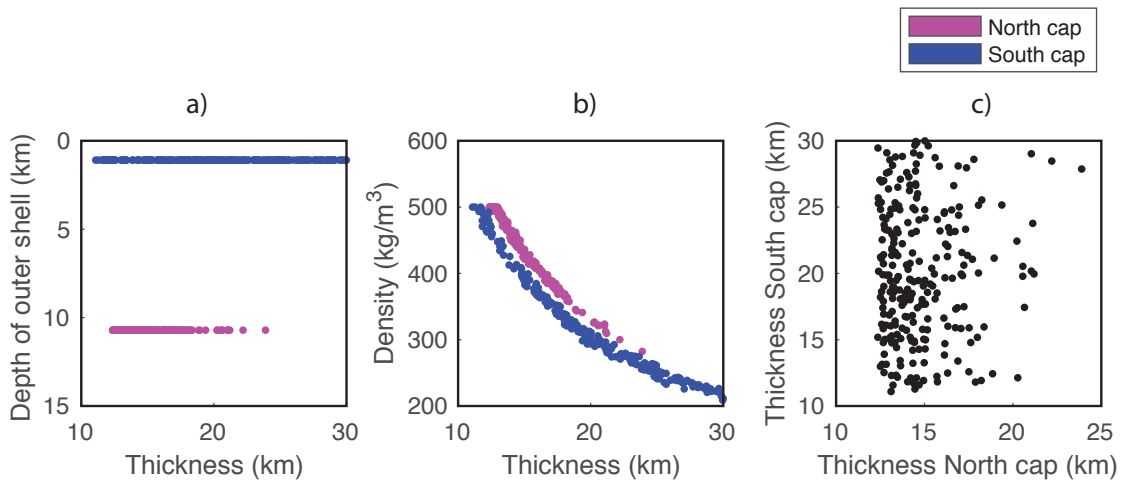


Figure 3.10: Depth, thickness and density values of all models in the ensemble. a) The values of the depth of caps between different models do not change significantly while their thicknesses do. b) Thicker caps in a model have a lower density value than thinner caps in a different model. This is a consequence of the density being obtained by an optimization of the difference between the input gravity data and the gravity data produced by the model at iteration. Since the depth of the caps do not change much, the density values depends on their thicknesses. c) There is no clear relationship between how the thickness of the North cap varies with respect to the thickness of the South cap. These parameters are independent.

value for the three parameters was lower than the odds of worsening the latitude and longitude of the cap.

The prior constraints on the depth of the caps (table 3.1) show that the spherical caps are only allowed to be inside the sphere so the value of their depths is always going to be skewed to deeper values. Figure 3.9 show that the caps in the mean model are always deeper than the ones in the target model. Since the thickness is modified in a individual step and the density of the cap is optimized, modifying the thickness of the current model is easy and proposed models with different thicknesses do not change the fit very much so they are more likely to be accepted than proposed models with a modified location value.

Figure 3.10b shows that, with increasing thickness of a cap, its density decreases. This allows the mass of the cap to be almost constant and produce a similar gravity anomaly than the one produced by the target model. This is a consequence of the fact that the density is not a free parameter of the Monte Carlo algorithm. It is instead obtained by a linear optimization of the difference between the input gravity data and the gravity data produced by the model at iteration i . Figure 3.10c shows that there is no clear relationship between how the thickness of the North cap varies with respect to the thickness of the South cap. These parameters are independent.

The number of caps is another parameter of the ensemble models. All of the models have two caps which is the same as in the target density model. This parameter is perfectly constrained by the input data. The noise of the input data is correctly recovered at 1×10^{-2} mGal. This is possible because the same parametriza-

tion used to produce the input gravity data, is used to find the ensemble models. In contrast, when using spherical caps to produce the input gravity data and point masses to produce the ensemble models, a THB algorithm overestimates the noise variance as described in Chapter 2 (section 2.4.2.3).

3.5 Discussion

The comparison between the mean density model obtained by THeBOOGIE algorithm presented in this paper and the target density model show that the algorithm is able to recover the latitude, longitude and aperture of the caps perfectly and quantifies the expected trade-off between depth, density and thickness of the caps. The spherical cap parametrization allows then the recovery of the location, shape and size of the density anomalies, improving on the point mass parametrization used by Izquierdo *et al.* [41] that only recovers the location of the center of this anomalies.

The input gravity field contains only two visible gravity anomalies with a relative similar size and shape. A more realistic gravity field of the Moon would contain features of different sizes and shapes, additionally to the circular features of impact basins. A density model that produces a similar gravity acceleration would require many spherical caps. Since the time needed to compute the gravity field of model m at each iteration grows linearly with increasing number of caps, the iterations would take much longer than the ones in the inversion described here. Because the number of parameters to find grows with increasing number of caps

too, more iterations of the inversion algorithm would be needed to run in order to find the correct combination of parameters values that fit the gravity data.

In general, a more realistic input gravity field of the Moon would require a longer running time of THeBOOGIe. That is expected for all parametrizations because there are more parameters to find. However, the issue with the spherical cap parametrization is that the running time might be too long for practical applications. For the inversion described here, the THeBOOGIe was ran for 1×10^6 iterations for a total of 70 hours in processor running at 2.8 GHz. An inversion of the gravity field produced by a target model with three spherical caps was tested and convergence was not achieved even after running the algorithm for seven days and 1.5×10^6 iterations. The time it would take to find the parameters of more than two caps is unknown but it is too large for our purposes and resources available. The algorithm needs to be more efficient in the calculation of the gravity field of proposed density models or in the sampling of these models before it can be applied to the inversion of realistic gravity fields.

3.6 Conclusion

We build on the THB global gravity inversion algorithms by using a three-dimensional parametrization of the density anomalies that allows for the recovery of their location, shape and size. The results show that the algorithm matches the lateral location perfectly and quantifies the expected trade-off or non-uniqueness in depth but an increase in the complexity of the input data and corresponding output

ensemble is needed in order to apply this parameterization to realistic planetary inversions.

Chapter 4: Bayesian gravity inversion algorithm for inferring finite size density anomalies in planetary interiors

4.1 Abstract

Gravity inversions have contributed greatly to our knowledge of planetary bodies such as the Moon. They are especially important to constrain the thickness and density variations of the lunar crust. Commonly-used inversion methods, however, would map mantle density anomaly features to the crust as they assume all the Bouguer gravity anomaly signal is coming from the crust-mantle boundary. In order to find density anomalies at different depths, we use a Transdimensional Hierarchical Bayesian Object-Oriented Gravity Inversion method (THEBOOGIE) that does not require any prior constraints in the location of the density anomalies. This iterative method divides the whole volume of the sphere into regions of similar density (Voronoi cells) where the number of regions, their size and location are chosen from a prior uniform distribution. At each iteration, the optimal density of the regions, at their randomly chosen location, and the fit of the density model to the surface gravity data of the body is calculated. Models fitting the data and additional constraints are saved and an ensemble of well fitting models is output when convergence

is achieved. We validate this method by creating a target density model and comparing how well the mean of the ensemble matches its features. The density anomalies in the target model emulate lunar density anomalies: the difference in thickness between the near and far side of the crust, the SPA basin, Imbrium and Serenitatis mass concentrations and a deep feature at the mid mantle. The algorithm is able to recover the lateral location of all the anomalies correctly but overestimates the thickness of the shallow features. The shape of the deep feature in the target model is recovered correctly. Because the output is a group of density models, instead of just one, we can obtain measures of variation from the mean density at each location inside the sphere. This variation provides information about the sensitivity of the method to different depths and about how uniquely a value can be constrained given the data. THeBOOGIe does not provide tighter constraints on the location of the shallow features yet but it provides a new way to detect density anomalies at different locations without mapping deeper anomalies to the crust depth while, at the same time, providing measures of confidence in the density values found.

4.2 Introduction

A layered model of the interior of a planetary body is an idealization of the distribution of material inside it. However, regions with different temperature or composition might exist within layers and the properties of these regions might shed light on the overall history of the body. For example, the location and shape of Large Low Shear Velocity Provinces (LLSVPs) on Earth [50] constrains different

models of the circulation of the mantle [51–56]. The size and magnitude of mass anomalies under impact basins on the Moon indicates the state of compensation of the surrounding crust and upper mantle material at the time of the impact [13]. Deeper anomalies in other planets have also been proposed [57].

Seismic and gravity data can both constrain anomalies in the interior structure of planets, but, because of costs and technology limitations, seismic data is only available on Earth, the Moon [58] and, more recently, Mars [59]. Gravity data, instead, is available for all terrestrial planets and is the most complete data set to infer global density anomalies in other bodies [9]. Gravity data is a sampling of the acceleration felt by a satellite caused by the mass of the body that is orbiting [60]. Regions with a higher density exert a higher pull on the satellite and regions with a lower density, exert a lower one, changing by different amounts the orbit of the satellite which is being tracked from Earth. Thus, inverting gravity provides constraints on the distribution of density anomalies inside a planetary body, especially the deviations from a perfectly radial structure.

Gravity inversions are non-unique and different methods have been developed to obtain unique density models from gravity data. In lunar applications, for example, positive lunar Bouguer gravity anomalies have been linked to regions with a shallower crust-mantle boundary and negative gravity anomalies to a deeper boundary assuming a constant density of the crust and mantle [10,61]. A shallower crust-mantle boundary produces a positive gravity anomaly in the surface because there is more high density mantle material and less low density crustal material than in a location with a deeper boundary. Two-dimensional density variations in the crust

and upper mantle below the South Pole-Aitken basin have been inferred by minimizing residual stress in the lithosphere and residual Bouguer gravity [62]. These gravity inversion have provided invaluable insight into the structure of the crust and upper mantle of the Moon; however, they do not provide a complete view of the density distribution in planetary interiors. Remaining challenges include: constraining the three-dimensional shape of density anomalies instead of only lateral variations; eliminating the need for extensive prior information like compensation state or depth of anomalies; and providing a measure of how well model parameters can be resolved by the gravity data. An inversion method that addresses these challenges would help infer density anomalies at different depths, although perhaps at the cost of producing a more complex result than traditional inversion methods.

We developed a new gravity inversion algorithm that considers that density anomalies might be present anywhere from the core-mantle boundary to the surface of a spherical body. With this method, the density, location and number of anomalies are constrained from the gravity data. Prior assumptions, like limiting the depth of anomalies to the crust mantle boundary, are not needed but could be included if desired. Our method does not eliminates the non-uniqueness of gravity inversions but it quantifies it by obtaining a group of density models that match the gravity data. In that way, our method provides a result that complement other analyses where a priori constraints, not all of which are independently justified, artificially reduce the number of presented results. From this group of models, it is possible to obtain the range of densities, locations and number of anomalies that match the data and to inform decisions about the confidence of the interior view of the body.

Our algorithm, called THeBOOGIe for Transdimensional Hierarchical Bayesian Object Oriented Gravity Inversion, belongs to the general Transdimensional Hierarchical Bayesian (THB) family of gravity inversion algorithms. Transdimensional means that the number of anomalies is not fixed *a priori* [63]. Hierarchical means that the noise of the gravity data, including the modeling error, is a result of the inversion and not necessarily an input [32]. Bayesian means that it uses Bayes’ theorem to infer which density model better represents the interior based on the gravity data and prior information [64]. By Object-Oriented, we mean that the distribution of density in the interior of a planetary body is parameterized as a collection of finite size objects.

Although several choices for the parametrization of density anomalies are possible, we focus here on a space-filling discretization of the planetary interior that uses Voronoi regions and a tesseract grid described in section 4.3. This work builds on previous THB methods that constrain 2D features or layered structures inside bodies at different scales (for example, [65–67]) and our earlier gravity inversion method, that was based on a collection of point masses in the interior of a planetary body [41].

In this paper, we first describe the parametrization used to represent the volume of a planet or moon and the shape of density anomalies (section 4.3). In section 4.4, we explain how to quantify the fit and quality of density models. In section 4.5 we show the steps of the gravity inversion algorithm. We then show the results of inverting synthetic gravity data produced by an idealized version of certain lunar density anomalies and describe how the chosen parametrization and values

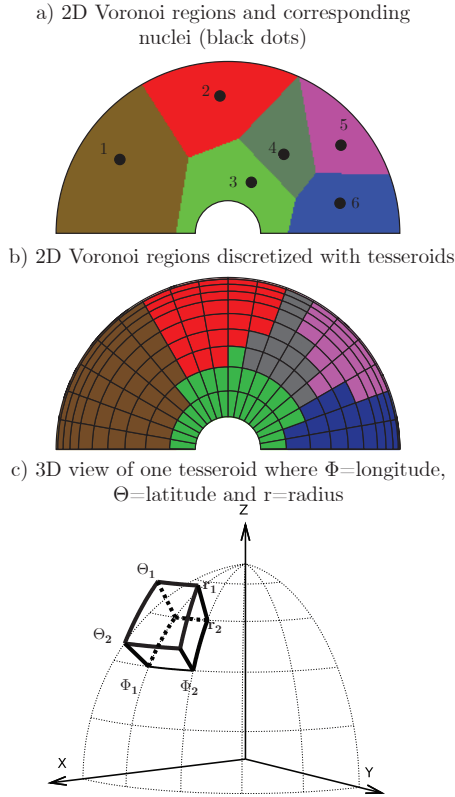


Figure 4.1: Voronoi regions and underlying tesserooid grid. a) A Voronoi region (VR) is the volume closer to a nucleus than to any other nuclei. The number of nuclei define the number of regions in which the volume of a sphere is divided. Moving one nuclei to a different location changes the boundary of its corresponding VR and the ones surrounding it. Voronoi regions are used in this work to represent regions inside the sphere with constant density. b) VR are discretized by an underlying tesserooid grid to aid in the computation of the gravity acceleration produced by the density distribution inside the sphere. c) A tesserooid is the intersection between two latitudes, two longitudes and two concentric spheres.

of parameters of the density models influence inversion results (section 4.6). We finally discuss the advantages and disadvantages of the application of this method to planetary geophysical problems (section 4.7).

Layer number	Depth range (km)
1	0 to 14.1
2	14.1 to 56.4
3	56.4 to 126.8
4	126.8 to 225.4
5	225.4 to 352.2
6	352.2 to 507.2
7	507.2 to 690.4
8	690.4 to 901.7
9	901.7 to 1141.3
10	1141.3 to 1409

Table 4.1: Depth range of tesseroids in the grid.

4.3 Discretization of the interior: Voronoi regions and tesseroid grid

A model is a simplification of reality. Therefore, we use the term density model to refer to a simplification of the three-dimensional density distribution inside a planetary body. The planet shape is represented by a perfect sphere of radius R and the density distribution inside the sphere is represented by Voronoi regions (VR) of constant density. Voronoi region i encloses the volume closest to the nucleus i than to other nuclei inside the sphere [22]. Figure 4.1a shows a schematic of six two-dimensional VRs dividing the area of a half circle. The area inside a VR has a constant density value represented by its color. Using Voronoi regions to represent the density distribution inside a sphere allows the flexibility to have many small VRs in places where there are small scale density variations while having only a few large VRs in places where the density does not vary much. Since the number of density regions is not a prior constraint in transdimensional inversions, the VRs are specially suited to estimating this number as required by the input gravity data.

The calculation of the gravity acceleration of three-dimensional polygons with

changing shape is expensive. It is necessary to find a way to compute the gravity acceleration quickly since it is computed at each iteration in THEBOOGIE. To solve this issue, we discretize the Voronoi regions into units of volume with fixed locations (figure 4.1b). These units are called tesseroids and they are the intersection of two latitudes, two longitudes and two concentric spheres (figure 4.1c). [68] provided a program to compute the gravity acceleration of a group of tesseroids, making it possible to pre-compute the gravity acceleration of each tesseroid in our grid before an inversion and then only multiply the acceleration values produced by each tesseroid by the density value of the Voronoi region enclosing the tesseroid.

The VRs corresponding to each of the tesseroids in the grid are found by doing a k-nearest neighbor analysis between the center of all tesseroids and the nuclei. The Euclidean distance between the points is found and the tesseroids with centers closest to nucleus i than to the other nuclei are assigned the density value of Voronoi region i . Another advantage of using tesseroids is that it allows an easier comparison between the density distribution in different models. For the fixed location of tesseroid i we can compute the mean and standard deviation between the models of the ensemble in a straightforward manner.

Our tesseroids have a 10° size in latitude and longitude. The resulting grid have 648 tesseroids per layer and 10 layers in depth, extending from the surface to the core-mantle boundary. Table 4.1 shows the depth range of each layer of the grid. The thickness of the layers increase with depth as seen in figure 4.1b because it is unlikely that the gravity data is sensitive to very small density features in very deep regions. The number of iterations it takes for the algorithm to reach convergence

depends mostly on the number of Voronoi regions inside the sphere and the memory depends mostly on the number of tesseroids of the grid. The resolution of our tesseroid grid and the maximum number of VR allowed inside the sphere (100) were selected to keep the duration of the inversions presented here under a week and the memory resources under the available ones.

4.4 Selection criteria for density models. Posterior, likelihood and acceptance probabilities

In gravity inversions, density models must fit the radial component of the gravity acceleration of a body in order to be considered acceptable models of its interior. Since gravity inversions are non-unique, many models might fit the gravity data with the same error, and all of these models should be considered as a possible representation of the interior if there are no additional constraints that shows they are unrealistic. THEBOOGIE outputs an ensemble of density models fitting the data with similar error. This ensemble does not contain all of the possible models, of course, but a representative sample of them. The criteria of how to sample a representative group of models is based on Bayes' theorem from which an acceptance probability can be calculated and an iterative Markov chain algorithm to propose models from a uniform prior distribution and save them or delete them based on the acceptance probability (section 4.5).

Equation 4.1 shows Bayes' rule, applied to gravity inversions. $P(\rho_m|\{g\})$ is the

probability of a density model ρ_m being correct based on the observed gravity acceleration data $\{g\}$. It is proportional to the likelihood $P(\{g\}|\rho_m)$ or the probability of model ρ_m producing the same gravity data $\{g\}$ multiplied by the probability of that model being correct according to our current understanding of the interior, or prior information $P(\rho_m)$.

$$P(\rho_m|\{g\}) \propto P(\{g\}|\rho_m) P(\rho_m) \quad (4.1)$$

In this work, a density model ρ_m (equation 4.2) is uniquely defined by the number of Voronoi regions n , their nuclei location vectors $\{v_{loc}\}$, the density values of each region $\{\rho\}$ and the value of the noise variance σ_g^2 . The noise variance is a parameter of the model because it includes the inferred uncertainty of the gravity measurements and the modeling error [69].

$$\rho_m = n, \{v_{loc}\}, \{\rho\}, \sigma_g^2 \quad (4.2)$$

Equation 4.3 shows the likelihood or how well the combination of parameters in the density model fits the gravity data. This is obtained after a forward calculation where the gravity data produced by the density model is compared to the gravity data of the body. The better the fit, the higher probability of this model being the correct one.

$$P(\{g\}|\rho_m) = \frac{|\tilde{C}_m|^{1/2}}{(\sigma_g^2)^{s/2}(\rho_{\max} - \rho_{\min})^n} \exp\left(-\frac{\Phi}{2}\right) \quad (4.3)$$

	$v_{loc}\hat{r}$	σ_g^2	n	ρ
Min	<i>CMB</i>	$10^{-14} \text{ (m/s}^2\text{)}^2$	1	-500 (kg/m ³)
Max	<i>R</i>	$10^{-10} \text{ (m/s}^2\text{)}^2$	500	500 (kg/m ³)

Table 4.2: Uniform prior distributions used in equation 4.1. R is the radius of the sphere. The limits of the radial component of vector $v_{loc}\hat{r}$ are clearly marked by the boundaries of the sphere and nuclei are not allowed to be outside it. The distributions of σ_g^2 and n do not have tangible limits. We instead set them to sufficiently large values so that the posterior distributions for these parameters are not truncated.

\tilde{C}_m is the posterior covariance matrix which is a function of the data and model covariance matrices, σ_g^2 is the noise variance of $\{g\}$, s is the number of independent data points of $\{g\}$, n is the number of Voronoi regions, ρ_{\max} and ρ_{\min} are the limits of the density of the regions and Φ is the misfit between the gravity data produced by the model $\{g_m\}$ and the input gravity data $\{g\}$ (equation 4.4).

$$\Phi = (\{g\} - \{g_m\})^T \frac{1}{\sigma_g^2} (\{g\} - \{g_m\}) \quad (4.4)$$

The prior probability $P(\rho_m)$ shows our current understanding of the interior before data $\{g\}$ is taken into account. It can include constraints additional to the gravity field like *in situ* measurements of rock samples. If no additional constraints are available, then $P(\rho_m)$ can be uniform or non informative. For example, if there are no additional information about the possible locations of the nuclei, the prior probability of their vector location, $P(v_{loc})$ is uniform in the volume from the CMB to the surface. In this work, the prior probabilities are uniform within reasonable limits (table 4.2) in order to determine what the gravity data can tell us by itself. However more informative priors can be used too.

Putting it all together, equations 4.3, 4.4 and table 4.2 show the expressions

used to compute the posterior probability $P(\rho_m|\{g\})$ which assigns a high value to good density models based on their fit to the gravity data, prior constraints and the number of Voronoi regions it contains.

4.5 Gravity inversion algorithm

Section 4.4 shows how to use Bayes' rule to quantify what a good model is. In this section, we describe the algorithm used to create density models in a unbiased way, test them according to their likelihood and priors and output a group of good models representative of the interior distribution of density. A complete description of the derivation of the acceptance probability based on Bayes' rule is provided by Izquierdo *et al.* [41].

THEBOOGIE is a reversible jump Markov chain Monte Carlo algorithm that uses the Metropolis-Hastings criteria [26] to 1) choose models from a proposal distribution $q()$ and 2) keep models based on an acceptance probability α derived from equation 4.1. The probability of accepting a proposed model ρ'_m depends uniquely on the last accepted model ρ_m .

$$\begin{aligned} \alpha(\{\rho'_m\}|\{\rho_m\}) &= \min \left[1, \frac{P(\{\rho'_m\})P(\{g\}|\{\rho'_m\})q(\{\rho_m\}|\{\rho'_m\})}{P(\{\rho_m\})P(\{g\}|\{\rho_m\})q(\{\rho'_m\}|\{\rho_m\})} \right] \\ &= \min \left[1, \left(\frac{\sigma_g}{\sigma'_g}\right)^s \exp\left(-\frac{\Phi - \Phi'}{2}\right) \sqrt{\frac{|\tilde{C}_{m'}|}{|\tilde{C}_m|}} (\rho_{\max} - \rho_{\min})^{n-n'} \right] \quad (4.5) \end{aligned}$$

Equation 4.5 shows that a proposed density model has a higher acceptance probability if it has a better fit to the data and additional constraints than the

current model, if it has the same fit but fewer Voronoi cells or if its noise variance is smaller. Figure 4.2 shows an schematic of the rjMCMC algorithm that uses the acceptance probability α . This is an iterative method where, at each step, a pair of models is compared. Convergence is achieved when the likelihood of accepted models does not change anymore. After convergence is achieved, accepted density models are saved as the resulting ensemble of models that match the gravity data and are representative of the interior density distribution of a body.

As a first step, the algorithm sets the first density model with $n = 2$. The nuclei location of both Voronoi regions and the noise variance are selected from the uniform prior distribution. The density of the regions is optimized with a linear inversions bounded from -500 to 500 kg/m³. After this step, the accepted density model m is completely defined according to equation 4.2 and its likelihood 4.3 is computed. The proposed density model m' is set by making one change to m . This change can be adding a new nucleus or a new Voronoi region, deleting one, changing its location or changing the noise variance. The change is chosen randomly. After the number and location of Voronoi regions are defined, the density of each region is calculated by minizing the misfit between the gravity field of the body $\{g\}$ and the gravity field produced by the proposed model $\{g_m\}$. Obtaining the density values this way helps reduce the number of iterations needed to find good density models.

The data $\{g_m\}$ is calculated using the pre-computed forward problem approach for tesseroids in spherical coordinates provided by Uieda *et al.* [68]. After the values of all parameters are assigned, the likelihood of the proposed model is calculated and it is accepted with probability α . In iterations where the proposed model is

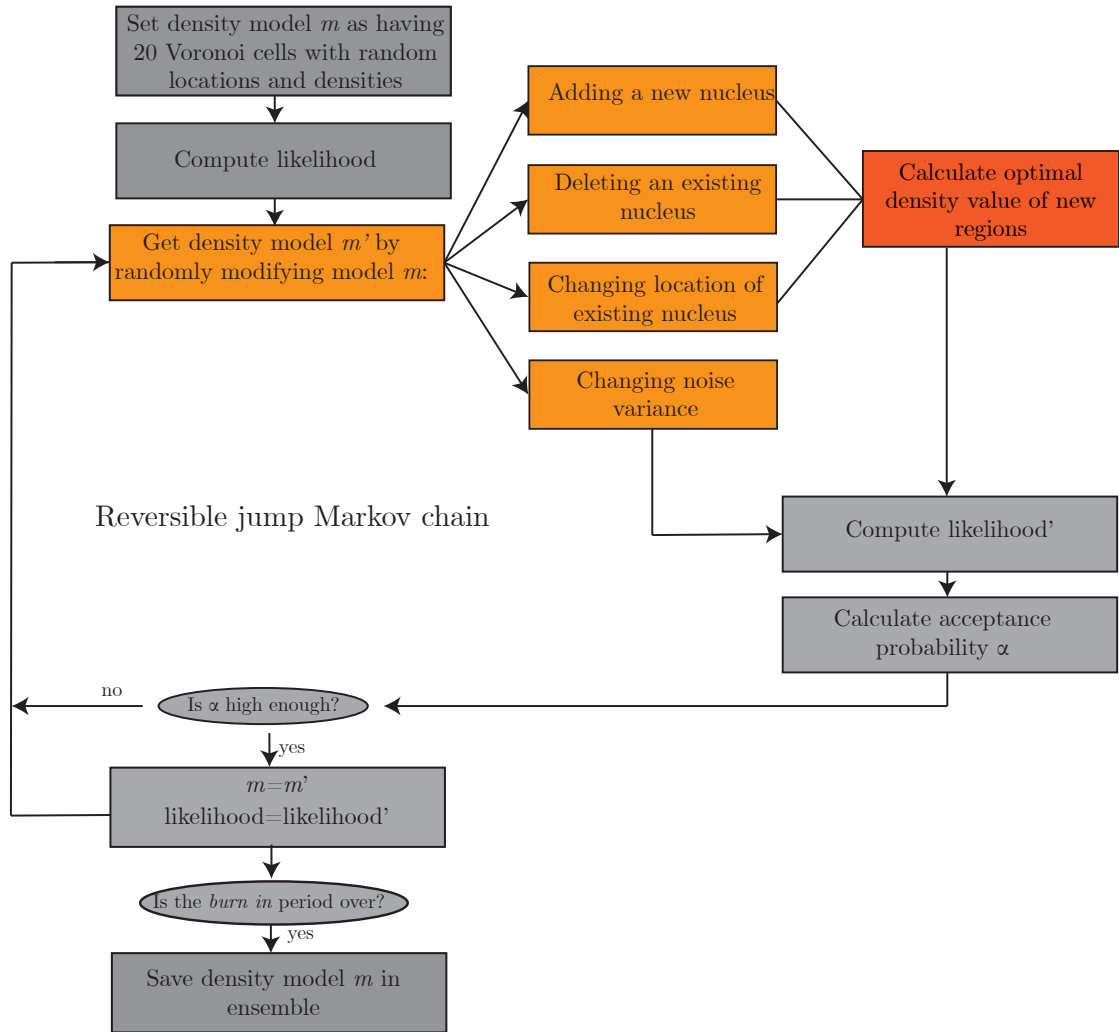


Figure 4.2: Flowchart of the TheBOOGIE. The initial model is chosen randomly. At each iteration, a new model is proposed by making a randomly chosen modification to the current density model. The proposed model is then accepted or rejected based on its acceptance probability (equation 4.5). The process is repeated until convergence is achieved. The output of the algorithm is a group of density models with a good fit to the input gravity data.

accepted, the model m takes the value of the parameters in m' . The process is repeated until accepted models have similar likelihood throughout many iterations and the ensemble is produced by saving a group of these last models. The burn-in period refers to the first iterations where the fit to the gravity data $\{g\}$ is not good since the initial model is chosen randomly.

Bayesian inversion algorithms of this sort have previously been used to invert various geophysical data, including gravity data. We have earlier presented a THB gravity inversion where the model was parameterized using a collection of point masses inside a planetary body [41]. Here, we adopt an object-oriented approach (See section 2) that motivates the acronym THEBOOGIe (Transdimensional Hierarchical Bayesian Object-Oriented Gravity Inversion) for our algorithm as a whole.

4.6 Method validation

We test how well the algorithm constrains the interior density distribution inside a sphere by inverting synthetic data resembling the lunar radial gravity acceleration. The objective is to compare the mean of the ensemble of density models to the target density model used to calculate the gravity acceleration. Using synthetic lunar data allow us to test more accurately how the acceptance probability and the Voronoi parametrization perform to find density features with shapes and locations likely to exist in the Moon. Since we can compare the output models to the one that is actually producing the gravity data, we can understand the tradeoffs and limitations of the algorithm before making inferences about the real interior of the

Moon.

4.6.1 Target density model and input gravity acceleration data

We consider density features that may be present in the interior of the Moon due to the availability of a high quality lunar gravity field [70] but very limited seismic information which makes it important to evaluate whether or not they could be constrained using gravity data. The target model is then a perfect sphere with a mean density of 3300 kg/m^3 and idealized lunar features that deviate from that mean density. The shape and location of the deviations or density anomalies are shown in figure 4.3. Plotting the anomalies instead of the absolute value of density, allows the visualization of the four features inside the sphere.

The gravity signature of the shallow features included in the target model can be easily identified in lunar Bouguer gravity maps [44] and are related to the crustal dichotomy, the South Pole-Aitken basin and the largest mass concentrations called mascons [71]. The Moon has a thicker far side crust than near side crust. The origin of this dichotomy is still uncertain but models of different near and far side thermal evolution result in consistent thicknesses [12]. The thicker far side crust is represented in the target model as a half shell 15 km thick with a density anomaly of -500 kg/m^3 (500 kg/m^3 less than the mean density of 3300 kg/m^3). The South Pole-Aitken (SPA) basin is the largest basin in the Moon. The SPA density anomaly in the target model is a positive and has a circular shape. The Imbrium and Serenitatis mascons are also positive density anomalies in the target model but

have a square shape due to the limitations in the resolution of the tesseroïds. The density anomaly of these basins is higher than the one in SPA because they are the result of the removal of crust from the impact and a superisostatic state of the Moon at the time of the impact, which allowed for more mantle material to be supported in such a shallow location [13].

The fourth feature in the target model is a deeper anomaly of the kind that has not been observed in the lunar gravity. There is no clear evidence that the deep feature exists but it is necessary to investigate the capabilities of the method to detect it in case anomalies at the same depth are mapped into shallower locations by other methods. It is also important to understand if the absence of a clear signal from a deep anomaly is because this signal would not be detectable or because there actually is no deep density anomaly.

Figure 4.3b shows the gravity data produced by the target model which is the input gravity data of THEBOOGIE. This gravity data is sampled at 10424 locations uniformly distributed at a altitude of 100 km over the surface of the sphere. The density distribution inside the lunar core is not to be constrained in this work. The target density model does not contain a core and, instead, covers the volume between the core-mantle boundary ($R_{core} = 330$ km) and the surface ($R = 1739$ km). The gravity data produced by the target model does not contain then the signal corresponding to a synthetic lunar core and the output models of THEBOOGIE will only be able to provide a density distribution between the same limits of R_{core} and R .

Figure 4.4 shows the natural log of the likelihood of the accepted density

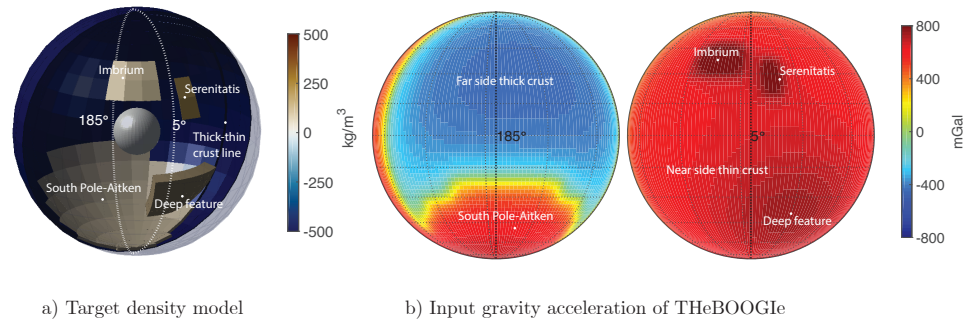


Figure 4.3: Target density model and input gravity acceleration data. a) Target density model. Plotted values are density anomalies from a reference mean density of 3300 kg/m^3 . The density of the Lunar mantle is 3330 kg/m^3 and the corresponding 30 kg/m^3 density anomaly in the target model was made transparent to help visualize the non spherically symmetric anomalies: the Imbrium and Serenitatis mascons, crustal dichotomy, SPA basin and a deep feature in the near side. b) Radial component of the gravity field used as input data in THEBOOGIE which are produced by the target model. The density distribution inside the core is not of interest in this work, therefore, the target model covers the volume between the core-mantle boundary ($R_{core} = 330 \text{ km}$) and the surface ($R = 1739 \text{ km}$) and the gravity acceleration data in b) does not contain the gravity signal corresponding to a synthetic lunar core. The longitudes 185° and 5° are used as references of the location of cross sections of the output model in figure 4.12.

model ρ_m for each iteration of the THB algorithm. As described in section 4.5, the likelihood is a measure of the residual between the input gravity data and the gravity data of the density model obtain at iteration i . Each line in figure 4.4 represents an inversion with a different initial density model, all chosen randomly. The likelihood generally increases with increasing number of iterations. It does so abruptly at first and then slowly converges to a certain value. The output ensemble of density models comprises 10×10^4 which are all saved after iteration 7×10^5 of the algorithm, when the likelihood is believed to have stabilized enough. The number of models that should be part of the ensemble is arbitrary, more models show a more detailed sampling of the different density distributions that match the input gravity data but also more memory is needed to save them and to later perform statistical analysis on them.

Figure 4.5a shows the mean gravity acceleration produced by the ensemble of models and figure 4.5b shows the average misfit or difference between the mean output gravity and the input gravity. The ensemble of density models fits the input data very well in most places, with maximum differences of the order of 80 mGal in the outline of the density anomalies related to the SPA basin, dichotomy and mascons. A finer grid would most likely reduce this differences. The inversion algorithm is able to find a group of models that fit the input gravity data. It is necessary, however, to look at the density distribution of these models in order to analyze the similarities and tradeoff they have compared to the target density model.

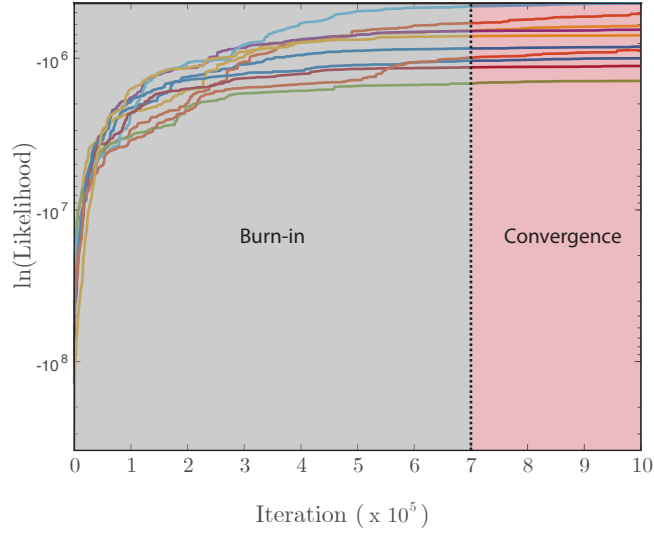
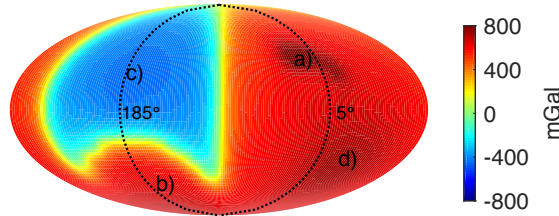


Figure 4.4: Natural logarithm of the likelihood per iteration of THeBOOGIE. Each line color corresponds to an inversion starting with a different initial density model. Each starting models was chosen randomly from an uniform distribution of the location of Voronoi nuclei and noise of the input data. The likelihood of each inversion increases with increasing number of iterations and converges after 700 000 iterations. Models obtained after convergence form the output ensemble used to compute mean density values and measures of variation.

a) Mean gravity of output ensemble



b) Average misfit

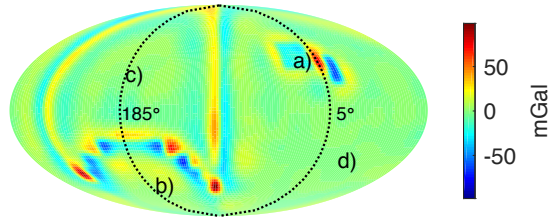


Figure 4.5: Mean gravity acceleration data and average misfit. a) The mean gravity data shows that most models produce radial gravity acceleration similar to the input data shown in figure 4.3b. b) The average misfit is the difference between the mean gravity of the output ensemble and the input gravity data. The largest differences are located in the boundaries of the far side crust, SPA basin and Imbrium and Serenitatis mascons. Points a) to d) are located in tesseraoids inside these features and they will be used as reference in plots throughout this work.

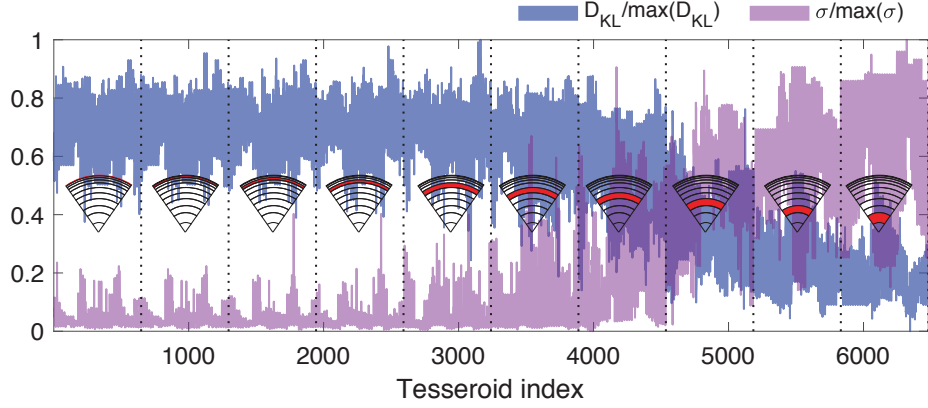


Figure 4.6: Normalized Kullback-Liebler divergence ($D_{KL}/\max(D_{KL})$ in blue) and standard deviation ($\sigma/\max(\sigma)$ in purple) of the density values of the ensemble. The values of these two functions are plotted against the tesseroid index with schematics showing the depth of the tesseroids at each layer. D_{KL} measures how different the posterior distribution of the densities at each location is from an uniform distribution (the prior distribution), with higher values being more different or less random. σ shows how much the density value of each location varies between models of the ensemble. The density values of shallow tesseroids have a less random distribution and less variation between different models in the ensemble compared to deeper tesseroids. The behavior of D_{KL} and σ show how much we can trust the deeper tesseroids relative to the shallow ones.

4.6.2 Output density models

As mentioned before, the output of THEBOOGIE is a group or ensemble of 10000 density models fitting the input gravity data. Each model contains a density value for each Voronoi Region and the corresponding tesseroids inside each region. In order to summarize the information given by this large group of models, we calculate the mean of density values for each tesseroid and two measures of the spread and significance of this value. It is more practical to calculate these quantities at the tesseroid level instead of the VRs because the tesseroid grid (number, location and size of tesseroids) is fixed for all models. The measures of spread and significance are the standard deviation (σ_ρ) and the Kullback-Liebler divergence (D_{KL}). The

standard deviation of the density value at tesseroid i shows what is the spread or variation of the density value at that location between all models in the ensemble. If σ_ρ is very large, then a wide range of density values at location i can fit the input gravity data and the density is then poorly constrained.

$$D_{KL}(p|q) = \sum_{i=1}^N p(\rho_i) \log \left(\frac{p(\rho_i)}{q(\rho_i)} \right) \quad (4.6)$$

The Kullback-Liebler divergence D_{KL} (Equation 4.6) quantifies how similar or different the posterior probability distribution of density at tesseroid i , $p(\rho_i)$, is from its prior distribution $q(\rho_i)$ [72]. Applied to Bayesian inference, D_{KL} shows how similar the distribution of density values in the ensemble is to the prior distribution. A tesseroid with high values of D_{KL} has a distribution of density values very different from a random one which implies that imposing constraints from input gravity data has added information on the density at that location. Conversely, a low value of the D_{KL} indicates a location where the results are dominated by the prior. Although it is conceivable that the prior is a good representation of the distribution of density at this location, it is also possible that the imposed data are not sensitive to this region. Thus, it is impossible to confidently interpret the density in these locations.

Unfortunately, there are not absolute values of σ_ρ and D_{KL} that clearly indicate if density values can or cannot be constrained by the input gravity data. In other words, there is no way to know which value of σ_ρ is too high or which value of D_{KL} is too low, we only know that a lower value of σ_ρ is better than a higher σ_ρ value, for example. We use the following criteria as an arbitrary indication that the

density value at tesseroid i can be constrained by the input data: $\sigma_{\rho_i}/\mu_{\rho_i} < 1$ where μ_{ρ_i} is the mean density at tesseroid i and $D_{KL_i}/\max(D_{KL}) < 0.5$ where $\max(D_{KL})$ is the maximum value of D_{KL} of all tesseroids.

Figure 4.6 shows the $D_{KL}/\max(D_{KL})$ and $\sigma_{\rho}/\max(\sigma_{\rho})$ of each tesseroid in the grid where $\max(D_{KL})$ and $\max(\sigma_{\rho})$ are the maximum value of D_{KL} and σ_{ρ} in all tesseroids, respectively. The schematics show the relative depth of the layer where they are located. There are 6480 tesseroids in the grid, distributed as 18 x 36 x 10. The indexing of the tesseroids from 1 to 6480 correspond to their location, where the first 18 correspond to different latitudes at the same 0 to 10° longitude range and the first 648 correspond to tesseroids at the shallowest layer. Deeper tesseroids have lower $D_{KL}/\max(D_{KL})$ and higher $\sigma_{\rho}/\max(\sigma_{\rho})$ than shallower tesseroids. This is expected since the gravity acceleration decreases with increasing distance from the source which makes the residual in equation 4.4 more sensitive to the density values of shallow tesseroids.

Figure 4.7 shows the density anomalies of the target model per layer. It contains the same values as in figure 4.3 with the difference that the density anomaly of the mantle is made visible. The mean density anomalies of the output models is plotted in figures 4.8 and 4.9. Figure 4.8 shows the density anomaly only in regions where the divergence is high enough and tesseroids with $D_{KL}/\max(D_{KL}) < 0.5$ are grayed out. Figure 4.9 shows the density anomaly only in regions where the standard deviation is low enough and tesseroids with $\sigma_{\rho}/\mu_{\rho} > 1$ are grayed out where μ_{ρ} is the mean density anomaly. Figures 4.7, 4.8 and 4.9 show which density values can be confidently constrained from the input gravity data and how those values are

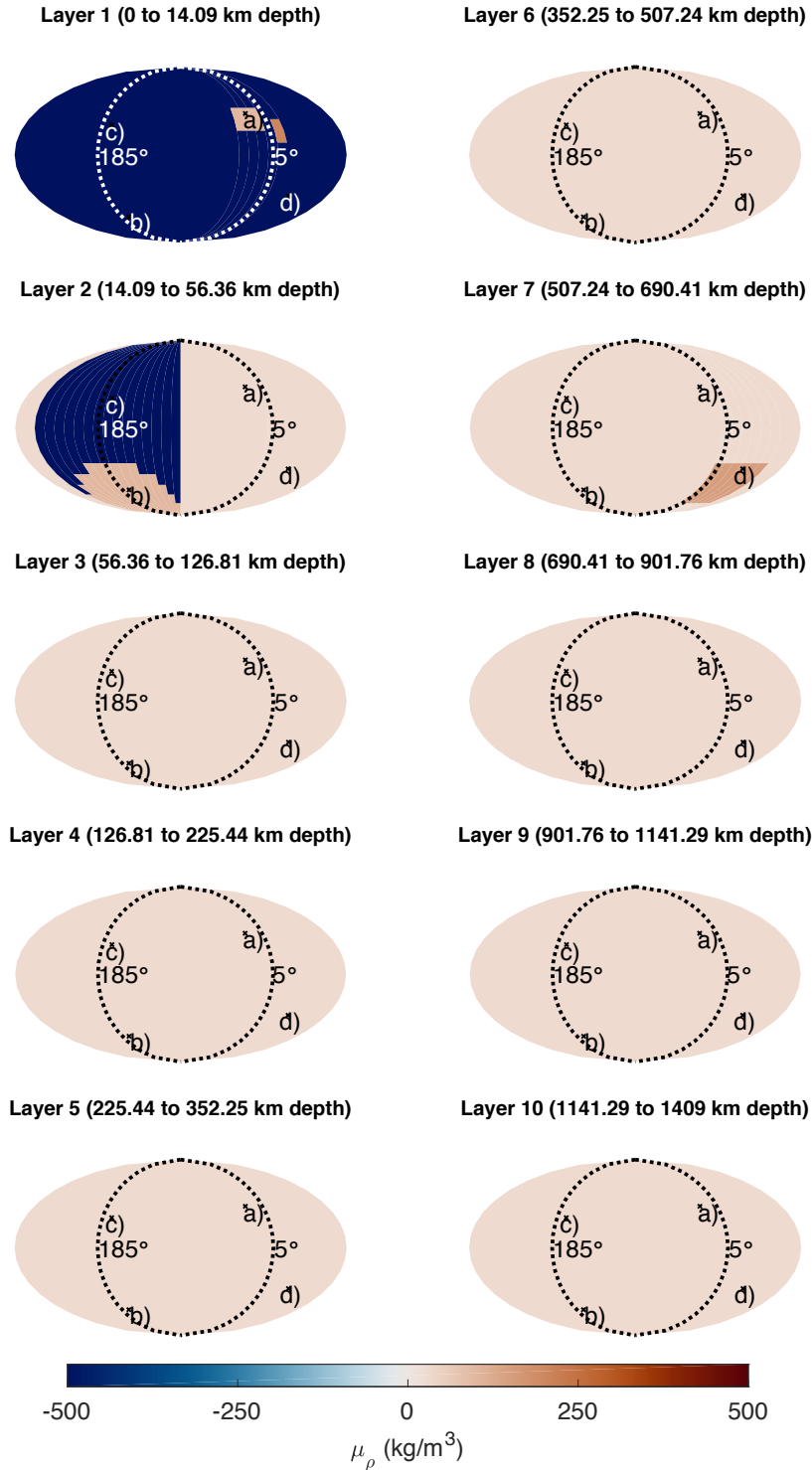


Figure 4.7: Density anomalies of the target model. Map view of each layer of the target density model shown in figure 4.3. The first layer has a negative density because the lunar crust is less dense than the reference density of 3300 kg/m³. The first and second layer show the density anomalies related to the mascons, crustal dichotomy and SPA basin. Layers 3 to 10 show the mantle density anomaly and layer 7 shows the deep anomaly.

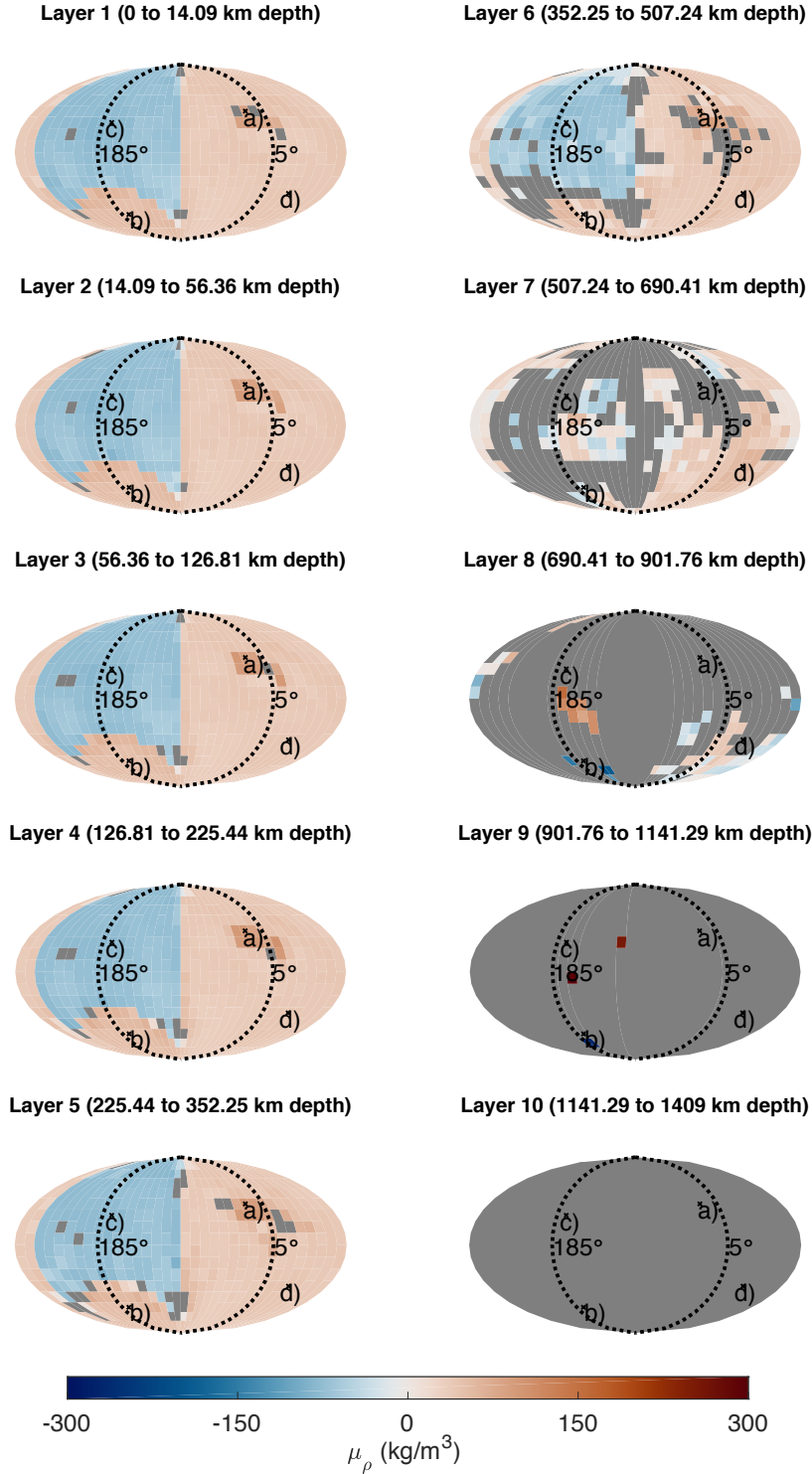


Figure 4.8: Mean density anomalies of the ensemble for each layer of the grid with the normalized Kullback-Liebler divergence as a measure of uncertainty. Tesseroids with $D_{KL}/\max(D_{KL}) < 0.5$ are grayed out in order to show only reliable values. The first six layers show clear density anomalies related to the crustal dichotomy, Imbrium, Serenitatis and SPA basins. Layer 7 shows a slight increase in density around point d). This is the location of the deep feature. The number of grayed out tesseroids increases with depth, from a few tesseroids near sharp density changes to all 648 tesseroids in layer 10.

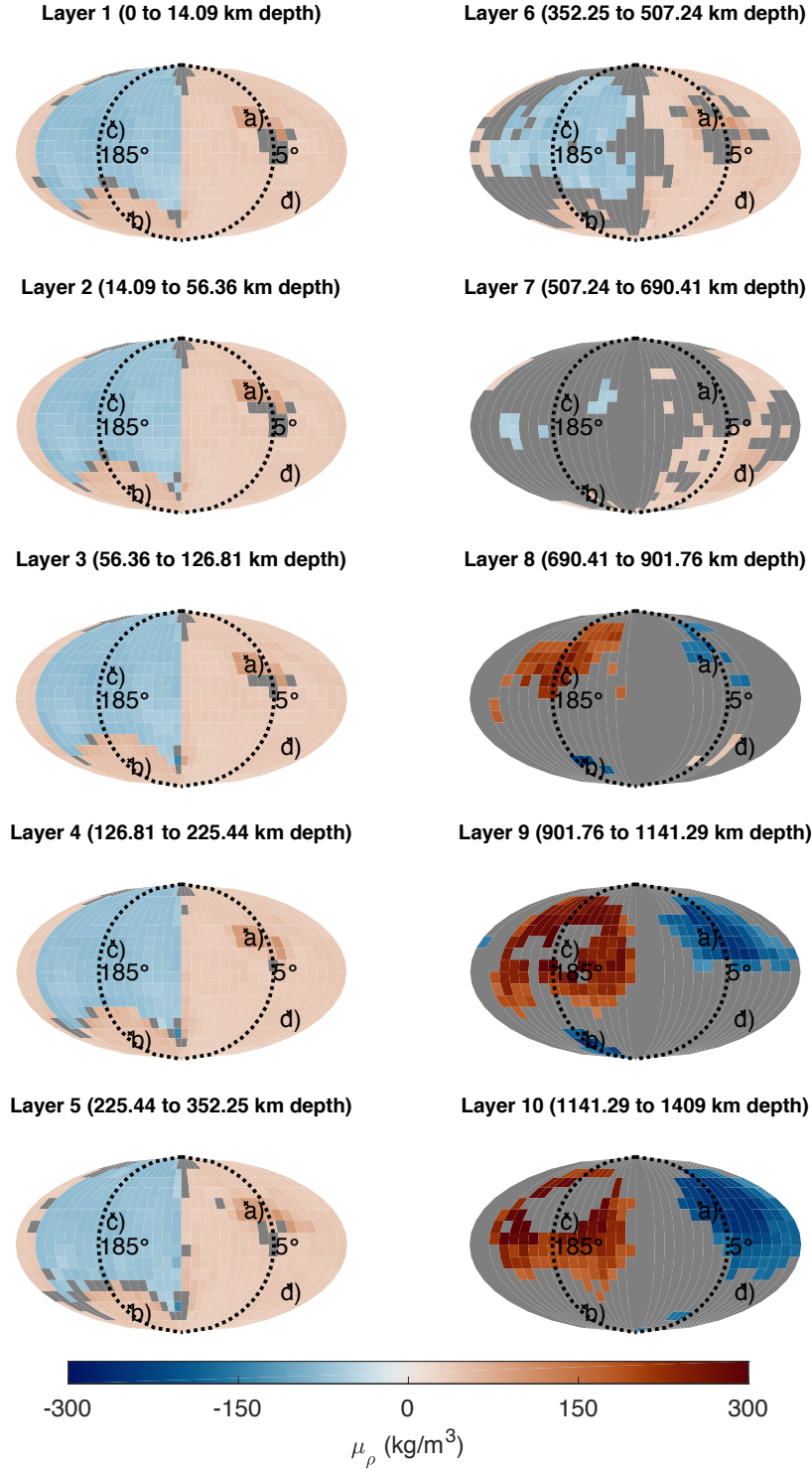


Figure 4.9: Mean density anomalies of the ensemble for each layer of the grid with the standard deviation as a measure of uncertainty. Tesseroids with a ratio of $\sigma_\rho/\mu_\rho > 1$ are grayed out in order to show values that can be confidently differentiated from 0. As in figure 4.8, the first six layers show clear density anomalies related to the crustal dichotomy, Imbrium, Serenitatis and SPA basins. Layer 7 shows a slight density increase in the location of the deep feature.

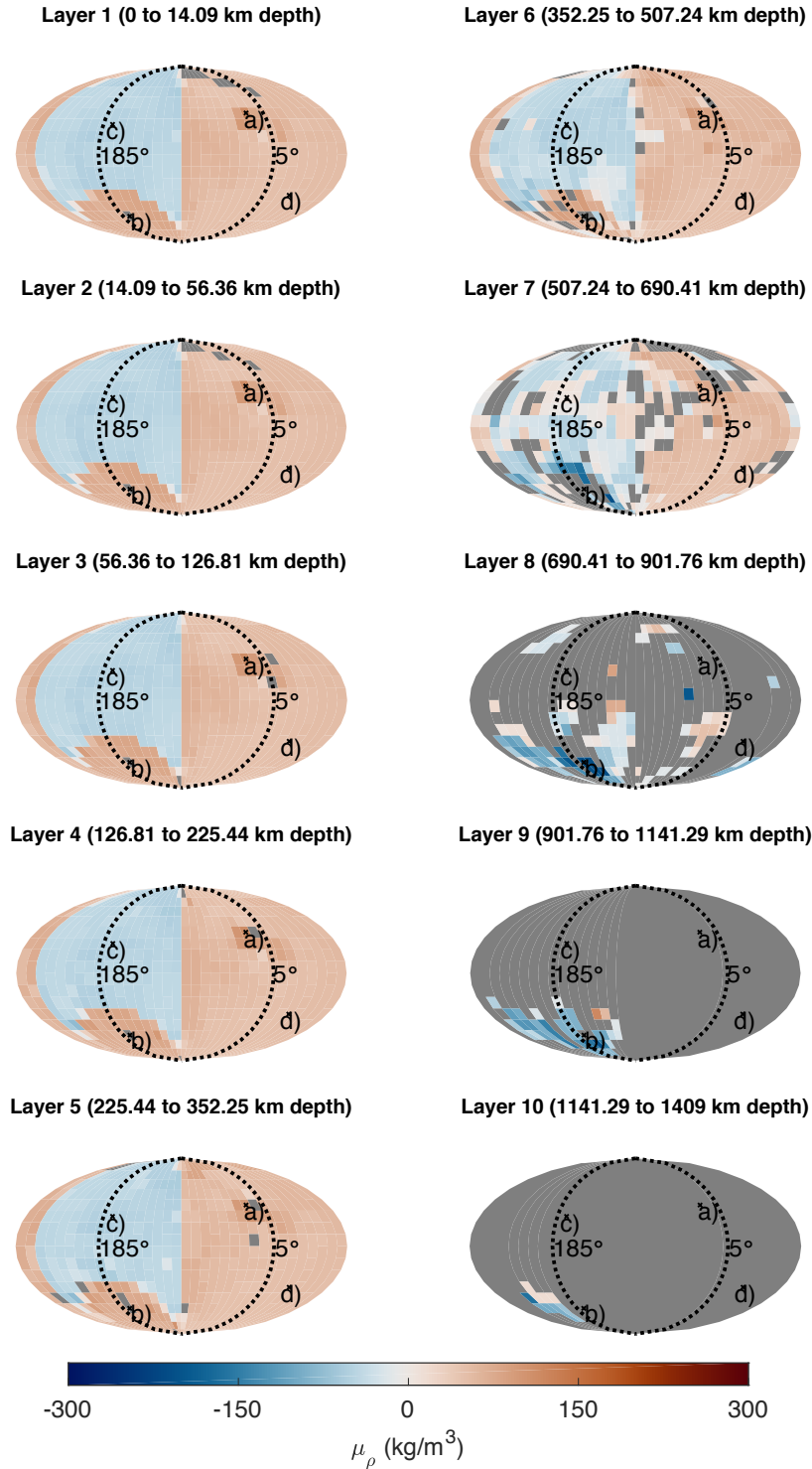


Figure 4.10: Mean density anomalies of the ensemble for an inversion where the gravity signal of the deep density anomaly is not included in the input gravity data. The normalized Kullback-Liebler divergence as a measure of uncertainty. Tesseroids with $D_{KL}/\max(D_{KL}) < 0.5$ are grayed out in order to show only reliable values. The first six layers show clear density anomalies related to the crustal dichotomy, Imbrium, Serenitatis and SPA basins. Layer 7 does not show an increase in density at location d) compared to surrounding area.

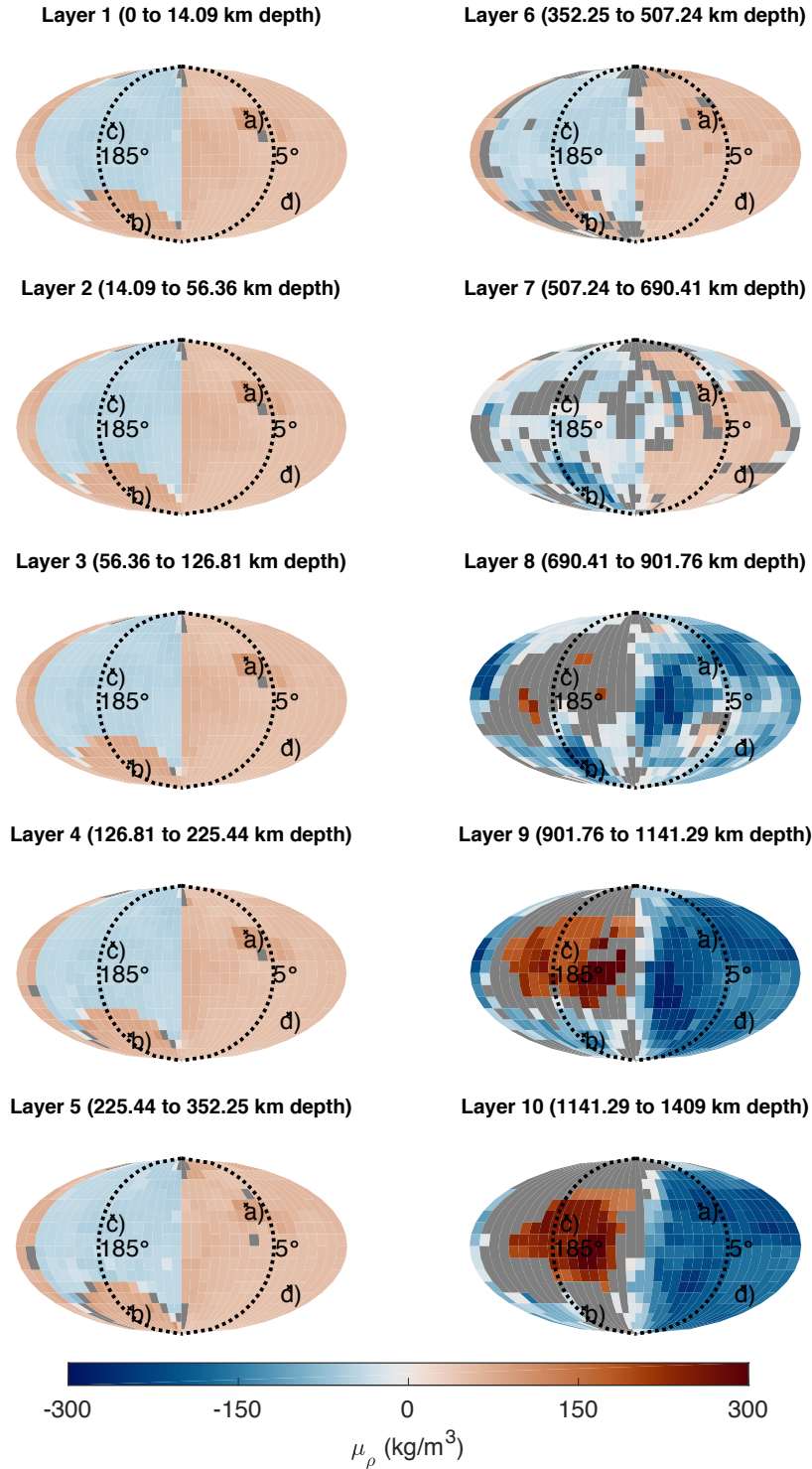


Figure 4.11: Mean density anomalies of the ensemble for an inversion where the gravity signal of the deep anomaly is not included in the input gravity data. The standard deviation is used as a measure of uncertainty. Tesseroids with a ratio of $\sigma_\rho/\mu_\rho > 1$ are grayed out in order to show values that can be confidently differentiated from 0. The first six layers show clear density anomalies related to the crustal dichotomy, Imbrium, Serenitatis and SPA basins. As in figure 4.11, layer 7 does not show an increase in density at location d) compared to surrounding area and it is not grayed out.

similar or different from the “correct” values in the target density model.

The first six layers of the mean of the output models have a similar density distribution, with regions of higher density anomaly at locations a) and b) and lower density anomaly at location c). Most of the tesseroids at these layers are visible in both Figures 4.8 and 4.9 which shows they are well constrained by the input gravity data. Layer 7 shows a region with higher density anomaly than the surrounding area at point d). This region is also well constrained by the input gravity data according to the two measures of confidence used. The density anomalies at layers 8 to 10 are completely uncertain using the Kullback-Liebler divergence criteria while only some of them are uncertain using the standard deviation criteria. The mean of density values in layers 8 to 10 is higher than their standard deviation but the distribution of density values within the ensemble is not significantly different the uniform prior. Plots of mean density of the output models without grayed out tesseroids, $D_{KL}/\max(D_{KL})$ and σ_ρ are shown in the supplementary material.

The density values at the first six layers of the mean of the output models form similar features than the ones in the first two layers of the target model. The features with positive density anomaly near points a) and b) has the same shape and location than the mascons and SPA in the target model while the feature with negative anomaly near point c) has a similar location and shape than the far side thick crust in the target model. The deep feature with positive density anomaly at layer 7 near d) has the same shape and location than the deep feature in the target model.

The main difference between features near points a) - d) in the mean of the

output models and the target model is the magnitude of their density anomalies and their thickness. The density anomalies of the target model have a higher magnitude (SPA 100 kg/m^3 , far side crust -500 kg/m^3 , Imbrium mascon 100 kg/m^3 , Serenitatis mascon 200 kg/m^3 and deep feature 150 kg/m^3) than the mean density anomaly of the output models (SPA 50 kg/m^3 , far side crust -100 kg/m^3 , Imbrium and Serenitatis mascon 85 kg/m^3 and deep feature 47 kg/m^3). The shallow density anomalies near points a)-c) extend from layer 1 to layer 6 in the mean model resulting in a thickness of 507 km while the same anomalies in the target model have varying thickness going from 14 km for the mascons, 70 km for the far side crust and 32 km for the SPA. The deep feature in the mean model has the same thickness and depth than in the target model. The two mascons in the target model appear as one feature in the mean model. We might expect that a higher resolution input gravity field than used here, and perhaps a finer tesseroïd grid, would be able to separate these features.

The density anomalies of layers 8-10 are much higher than anomalies in shallower layers and do not correspond to density anomalies in the target model. They are, most likely, a result of optimization of density performed in THEBOOGIE at each iteration. When the gravity acceleration of the model is not sensitive to a location in the grid, an optimization of the density values at that location results in very large magnitudes. Layers 8-10 also show a reversal of the magnitude of density anomalies between the far and near side. The far side has a positive anomaly while the near side a negative one. This can be explained by the fact that the anomalies related to the mascons, SPA and dichotomy are much thicker than in the target

model, creating an excess or deficit of mass that is compensated by the anomalies in layers 8-10.

We ran an inversion with a different input gravity data. The data does not contain the gravity signal of the deep density anomaly near point d), only the gravity signatures of the shallow features in the target model (SPA, dichotomy and mascons). Figures 4.10 and 4.11 show the mean of the output models for that inversion. The lateral distribution of density in the first six layers are very similar than the ones from the mean output of the previous inversion. The mean density anomaly of the SPA is 66 kg/m^3 , far side crust is -50 kg/m^3 , Imbrium and Serenitatis mascon is 93 kg/m^3 while there is no density increase near point d) in layer 7 compared to the surrounding area. The standard deviation and Kullback-Liebler divergence show similar variations per depth as in the previous inversions. Comparing the output model of this inversion with the output of the previous one shows that THEBOOGIE can effectively constrain a deep density anomaly down to a depth of 500 to 690 km if its signal is present in the input gravity data.

Figure 4.12 shows the mean density (μ_ρ), normalized divergence ($D_{KL}/\max(D_{KL})$) and standard deviation (σ_ρ) of the ensemble for a slice of the sphere at 185° and 5° . Locations with unconstrained density values according to any of the two criterias are grayed out. The mean density plot shows how depth the density anomalies are stretched out compared to the ones in the target density model. This is why most density models in the ensemble are able to fit the input gravity data very well even though the magnitude of the density anomalies is less than in the target model. Our inversion method does not provide tight constraints on the depth of density

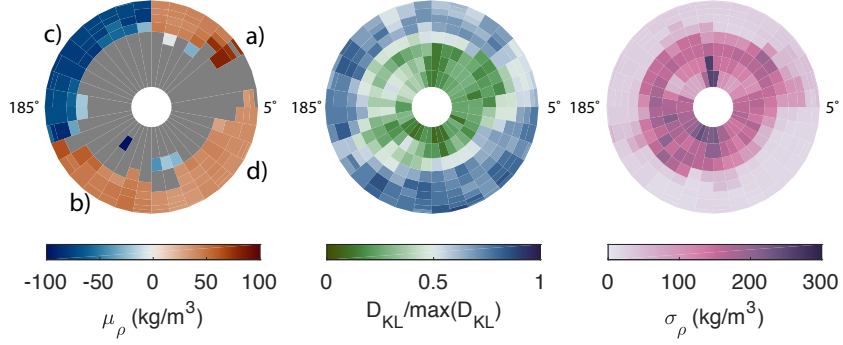


Figure 4.12: Slices of mean density of the ensemble (μ_ρ), normalized Kullback-Liebler divergence $D_{KL}/\max(D_{KL})$ and standard deviation (σ_ρ). Tesseroids in the left half are located at longitude 185° and the ones in the right at 5° which are the longitudes of the dashed lines shown throughout this work. The letters show the latitude of points a)-d). The mean density in a) is only shown in tesseroids with $D_{KL}/\max(D_{KL}) > 0.5$ and $\sigma_\rho/\mu_\rho > 1$ in order to focus on reliable density values according to the two measures of uncertainty. The colorbar is saturated at 100 kg/m^3 . Crustal density features like the mascons, SPA and dichotomy are thicker than in the target model while their magnitudes are lower. The deep feature does not appear in the slices because it is located at different longitudes but it is described in Figure 4.13

anomalies, which tend to bleed to greater depth. This might occur because the Voronoi Regions must fill the entire space of the planetary interior. The parsimony inherent to our methods favors a solution with a smaller number of regions, which necessarily will have greater volume. The density anomalies are therefore diluted through these regions.

Figure 4.13 shows density profiles at location d): the target density distribution, the mean of the output models, standard deviation (σ_ρ) and the normalized Kullback-Liebler divergence $D_{KL}/\max(D_{KL})$. The magnitude of the mean and its σ_ρ increases with depth while $D_{KL}/\max(D_{KL})$ decreases, consistent with the behavior shown in Figure 4.6. Figure 4.13 also shows the difference between the the crustal anomaly in the target model and the one in the mean output model. The

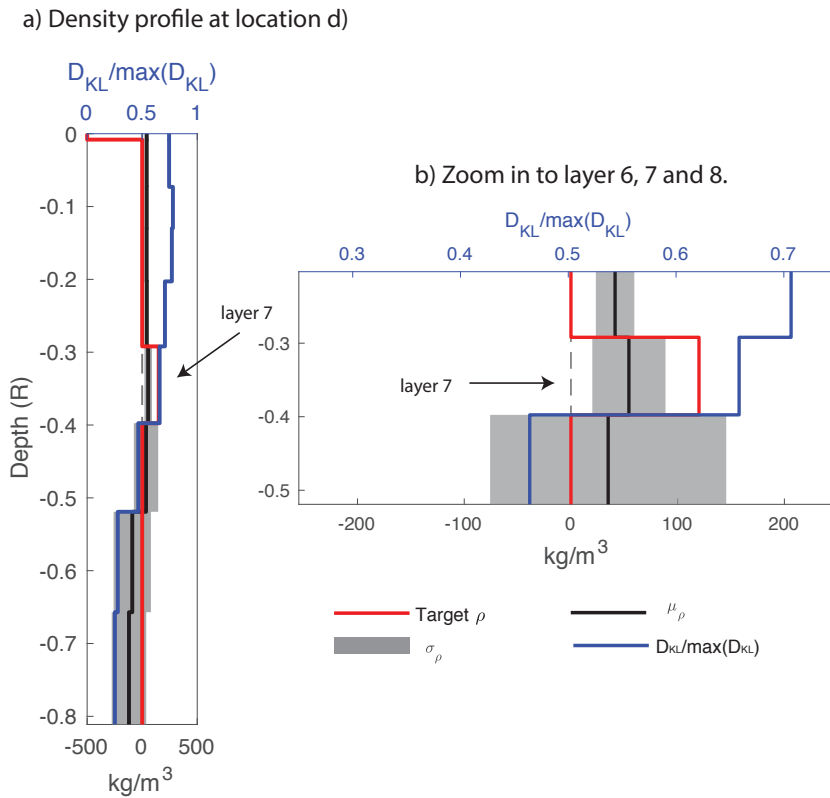


Figure 4.13: Target density, mean density of the output models (μ_ρ), standard deviation (σ_ρ) and normalized Kullback-Liebler divergence $D_{KL}/\max(D_{KL})$ at location d). a) Depth vs density for all layers. The negative density anomaly of the target model at layer 1 is not recovered by the output models and instead, the mean model has a positive anomaly stretching from layer 1 to layer 8. b) Zoom in to layers 6, 7 and 8. There is an increase in the mean density of the ensemble in layer 7 compared to layer 6 and 8. The location of this increase in the density coincides with the location of the deep feature in the target model, indicating that the algorithm can recover this deep feature although with a lower magnitude.

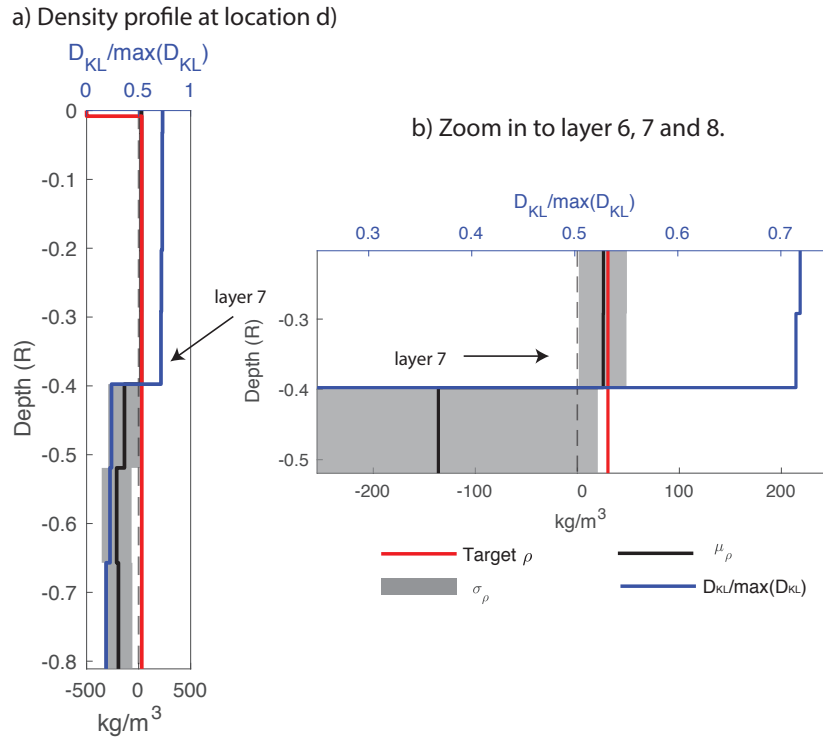


Figure 4.14: Target density, mean density of the ensemble (μ_ρ), standard deviation (σ_ρ) and normalized Kullback-Liebler divergence $D_{KL}/\max(D_{KL})$ at location d) for an inversion where the input gravity field does not contain the gravity signal of a deep anomaly. a) Depth vs density for all layers. The target density model has the same distribution of density as in Figure 4.13 with the exception of the increase of density at layer 7. b) Zoom in to layers 6, 7 and 8. The mean of the output models matches the density anomaly of the target model almost perfectly without an increase of density at layer 7.

target model has a crustal thickness of 14 km in the near side, shown also in Figure 4.7 as a negative density anomaly covering most of the first layer. The mean of the output models shows no negative crustal anomaly at the first layer, but a positive density anomaly extending from layer 1 to layer 6 (507 km thick). The mean of the output model does not recover the negative density anomaly in the first layer of the target model because this anomaly covers the whole shell, making it spherically symmetric and impossible to recover using gravity data. In figure 4.13 b), we can see that the mean density increases slightly at layer 7, where the deep feature of the target density model is located. In contrast, Figure 4.14 shows the distribution of density per depth for the same location from the output of an inversion where the input gravity data does not contain the gravity signal of a deep anomaly. There is no increase of density anomaly at layer 7 in Figure 4.14b. As mentioned before, the inversion algorithm can detect a density anomaly if its gravity signature is included in the input gravity data.

4.7 Discussion

The output ensemble used in plots of section 4.6.2 is obtained by sampling models after convergence is achieved in the THeBOOGIe. Convergence to a distribution, however, is not straightforward to identify. The mathematical proof of convergence to the posterior probability distribution only exists for an infinite number of iterations of a Markov chain algorithm [27]. Therefore, any convergence assessment on finite chains is flawed in theory. In practice, there are diagnostic

tools to assess convergence [73–75]. In this work, we follow the time-series approach and compare the change in the likelihood parameter between chains or inversions starting from different initial conditions.

The natural logarithm of the likelihood for the starting models of these chains range two orders of magnitude while the range of this parameter for the converged part, range less than one order of magnitude. Variations within each chain are also smaller in the convergence part than in the burn-in one and chains cross over in the burn-in part meaning they do not explore completely separate regions of the model space. These properties show convergence as it is usually assessed.

The models in the ensemble have the correct lateral location and boundaries of the density anomalies of interest while their thicknesses are overestimated. This issue might be a consequence of the shallow location of the anomalies in the target model (first and second layers), the Voronoi parametrization used and the linear optimization of the density values. The location of the Voronoi nuclei of the initial model are chosen randomly with uniform probability between the CMB and the surface which makes having a nuclei in the first layer of the tesseroid grid unlikely. The parsimony of the algorithm included in equations 4.5 makes density models with fewer Voronoi Regions most likely to be included in the output ensemble. Big Voronoi Regions result in thicker density anomalies and, in order to fit the input gravity data, these anomalies have lower values than in the target model. Randomly sampling the density values instead of optimizing them would eliminate this tradeoff but the convergence is too slow to be a practical solution.

The Kullback-Liebler divergence does not have a specific value we can use to

disregard tesseroids. The relative value used in this work $D_{KL}/\max(D_{KL}) < 0.5$ is arbitrary but the choice of this value would not change the retrieved lateral density distribution, only the depth to which we can interpret anomalies, whether or not there are anomalies close to the surface.

The discretization of the volume of the sphere in tesseroids allows us to retrieve the three-dimensional shapes of density anomalies and their corresponding density values. This discretization provides a clearer way to analyze what the inversion algorithm is able to constrain and what it is not able to. It is a key improvement compared to the point mass discretization used by Izquierdo *et al.* [41] where the gravity acceleration data of three-dimensional density anomalies were matched by configurations of point masses and no clear shape of density values could be recovered but only central locations.

THEBOOGIE estimates a thickness of 507 km for the mascons, far side crust and SPA basin. This value is not a better estimate than the ones given by other synthetic gravity inversion methods (41 km mean crust by Zhang *et al.* [76] and 100 km mean crust by Liang *et al.* [77], for example). On the contrary, this method provides a larger range of possible values because no informative prior is used and there is a tradeoff between the thickness of these features and their density anomaly. The advantage of this novel method is that it can constrain features of very different sizes in very different locations without the need to assume all the gravity anomalies are caused by anomalies in the Moho depth. Another advantage is that this method provides a measure of confidence in the resulting density distribution. Including prior information to limit the possible ranges of depths and magnitudes would reduce this

tradeoff and it would be interesting to explore how it would affect the ability of the algorithm to constrain features of very different sizes and locations.

4.8 Conclusions

We invert synthetic gravity data with magnitudes and features similar to the Bouguer gravity field of the Moon using a novel inversion algorithm, THeBOOGIe. This algorithm is able to recover the correct lateral location and boundaries of the density anomalies producing the input gravity data even when these anomalies have differences sizes and locations. The thickness of the crustal density anomalies in the target model is overestimated while the thickness of a mid mantle feature is not. The amplitude of all features is reduced. The reason for the mismatch between the thicknesses is that the correct location of the anomalies is too shallow and it is more likely to end up with nuclei at deeper locations. The method is able to provide the standard deviation and Kullback-Liebler divergence values of the output models. These two indicators of confidence allows us to provide a more complete analysis than current gravity inversions methods and inform decisions about the ability to constrain the density value of a region of the body given its gravity acceleration data.

Chapter 5: Shallow and deep density anomalies of the Moon from a flexible inversion of GRAIL data

5.1 Abstract

Knowledge about the interior structure of the Moon can help test hypotheses about its origin and evolution. In this study, we use Bouguer gravity acceleration from the GRAIL mission data to infer the location and shape of density anomalies in the Moon with respect to a mean density value of 3300 kg/m^3 . The inversion uses minimal prior constraints on the location of the density anomalies in order to fully explore the range of density distributions consistent with the observed lunar gravity field. This philosophy is complementary to the approach in which gravity variations are ascribed to a particular density interface in the subsurface, such as the core-mantle boundary. THEBOOGIE algorithm introduced in chapter 4 enables this inversion while obtaining a group of density models that fit the data from which confidence measures can be obtained.

The lateral distribution of shallow density anomalies matches the lateral variations in crustal thickness and other surface features. The shape and size of the SPA basin, near side basins and far-side highlands are recovered. Because we introduce

less prior information on the location of the density anomalies than other methods, shallow structures are smeared at depth. The confidence on the density values obtained decreases with increasing depth, as expected, but a clustering of the deep density anomalies shows that there are negative and positive density anomalies in the depth range of 507-1141 km. The density distribution of the far side is not significantly different from the one in the near side and deep moonquakes do not seem to be related to a specific positive or negative anomaly. Deep density anomalies might be related to an inefficient overturn of ilmenite cumulates or to water reservoirs in the deep mantle. However, their implications for the rheology and dynamics of the lunar mantle warrant further modeling study.

5.2 Introduction

The present-day interior structure of the Moon is a result of its compositional and thermal evolution. The difference in thicknesses and composition between the lunar far side and the near side [10, 12], for example, have been associated to spatial variations in tidal heating [78], tilted convection [79] and asymmetric crystallization of the lunar magma ocean [80]. The literature contains many other examples of the link between the interior structure of the Moon and models of its evolution [1, 13, 15, to name a few].

Different data sets have been used to infer the interior structure of the Moon. Seismic, electromagnetic and gravitational data, moment of inertia, tidal numbers and mean mass are only some of them [81]. Each type of data has its advantages

and limitations, often acting as complementary sources of information about the interior. Seismic data, for example, is able to distinguish between layered models of the Moon while it is not able to detect small-scale lateral variations due to the limited sampling done during the Apollo missions [11,14,82,83]. Gravity data, on the contrary, is not able to distinguish between perfectly radially-distributed material inside a sphere [84] but is able to detect anomalies at very different scales if they are not spherically-symmetric. The gravity acceleration data of the Moon has an impressive $4.5 \text{ km} \times 4.5 \text{ km}$ resolution at the equator [7] thanks to the gravity acceleration data sampled by the Gravity Recovery and Interior Laboratory (GRAIL) mission [6].

It is more practical to globally sample the gravity acceleration of a planet or Moon by orbiting satellites than by deploying a sufficiently large network of seismometers on its surface. Regions of the body with a higher density exert a higher pull on an orbiting satellite and regions with a lower density exert a lower one, perturbing the orbit of a satellite tracked from Earth [60]. Put simply, the tracking data is converted to spherical harmonic models of the gravity field after sources of acceleration modifying the trajectory of the satellite, other than the mass anomalies of the body, are removed [9].

The inversion of geophysical data is non-unique [85] and gravity inversions are no exception. Different density distributions can fit the observed gravity acceleration values [86]. However, the fact that gravity data from many planetary bodies is available, including all terrestrial planets, while seismic data is only available at Earth, the Moon [58] and, more recently, Mars [59], has made gravity data and gravity inversions necessary tools to constrain the properties of density anomalies

that exist within layers of a planetary body.

Different methods had been developed to reduce the non-uniqueness of gravity inversions. It can be reduced by requiring density models to fit additional types of data [87–90, for example] or by making prior assumptions about the interior density distribution of a body. The crustal and upper mantle density of the Moon, for example, have been assumed to be uniform and the observed Bouguer gravity anomalies considered to be caused by anomalies in the crust-mantle interface depth [10, 61]. A shallower crust-mantle boundary produces a positive gravity anomaly in the surface because there is more high density mantle material and less low density crustal material than in a location with a deeper boundary. If the prior assumptions used are not justified, however, then this would lead to biasing the density models obtained or neglecting other models that fit the data. Density anomalies in the mid mantle can be mapped as crustal thickness variations if the location of all anomalies is restricted *a priori* to the crust-mantle interface, for example.

In order to map out the likelihood of mass anomalies at all locations of the Moon and not only the crust-mantle interface, we need to use a gravity inversion method that does not require prior constraints on their depths and quantifies how well these anomalies are constrained by the input gravity data. A Transdimensional Hierarchical Bayesian gravity inversion algorithm is a great tool to do that since the prior constraints used can be non-informative and it outputs a collection of samples from the posterior distribution of density in the moon given the gravity field. From this output, the variation and significance of the density anomalies can be obtained [41]. Specifically, the Object-Oriented approach of THeBOOGle

algorithm can provide the finite-sized shape of these density anomalies. In this work, we invert lunar gravity data using THEBOOGIE algorithm and compare how the interior density anomalies obtained with this method and their variations compare to the accepted view of the lunar interior inferred by other methods.

5.2.1 Lunar interior anomalies

The existence of some features in the interior of the Moon is widely accepted while the existence of others is debated. Generally, shallow features are inferred with greater confidence because of the availability of gravity, topography and samples in addition to seismic data [9]. Mid-mantle or deeper features are more obscure because of the lack of samples and the reduced sensitivity of surface data to this depth.

The Bouguer gravity anomaly of a planetary body shows the gravity acceleration produced by the interior distribution of density after the removal of the acceleration due to topography, assuming a near surface density [43]. Figure 5.1 shows the Bouguer field of the Moon which is dominated by a broad negative anomaly related to the far side and positive anomalies related to the near side and impact basins. Figure 5.2 shows a map of the crustal thickness of the Moon obtained using this Bouguer data. Locations with a thicker crust coincide with locations having a negative Bouguer anomaly while locations with a thinner crust coincide with locations having a positive one.

The crustal thickness is constrained by the estimation of crustal bulk density from short wavelength gravity data [10] and estimation of the mantle density and

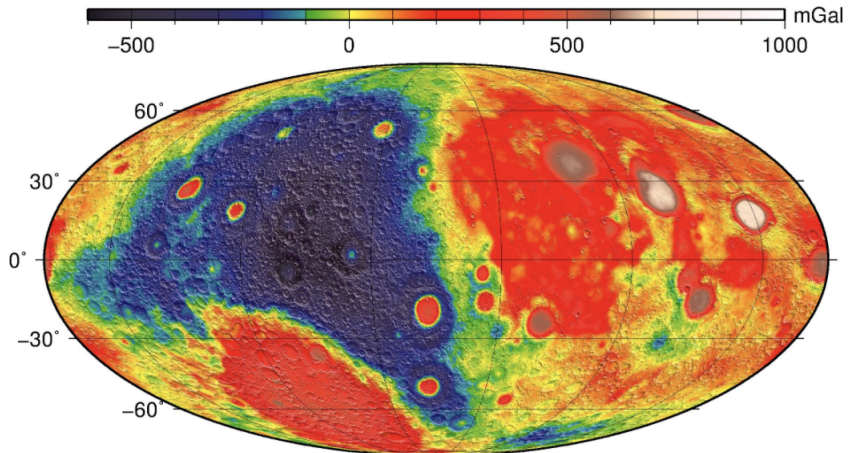


Figure 5.1: Bouguer gravity anomaly of the Moon (orders 1-700) from Lemoine *et al.* [47]. The acceleration is produced by the distribution of density inside a reference radius of $R = 1739$ km . The acceleration due to topography is removed. Figure duplicated from chapter 3 for convenience.

mean crustal thickness from seismic data [11]. The thickness of the lunar crust was inferred to be between 34 and 43 km in average. The far side crust is thicker than the near side crust (approximately 50 km in average for the far side and 30 km in the near side, near the location of the Apollo stations) and the crust of the SPA basins and the major basins in the near side is very thin, almost close to zero.

Lunar mantle anomalies have also been inferred but they are more uncertain than shallow ones. A seismic discontinuity in the range of 500-750 km has been proposed [19, for example] while a chemically uniform mantle can also fit the seismic data [20]. The presence of a partial melt layer in the lowermost mantle is supported by inversions of seismic and laser ranging data [1, 15, 91] while evidence of this layer was not found by Garcia *et al.* [16] using the same Apollo data. Moonquakes in the lower mantle are not uniformly distributed and none has been detected in the

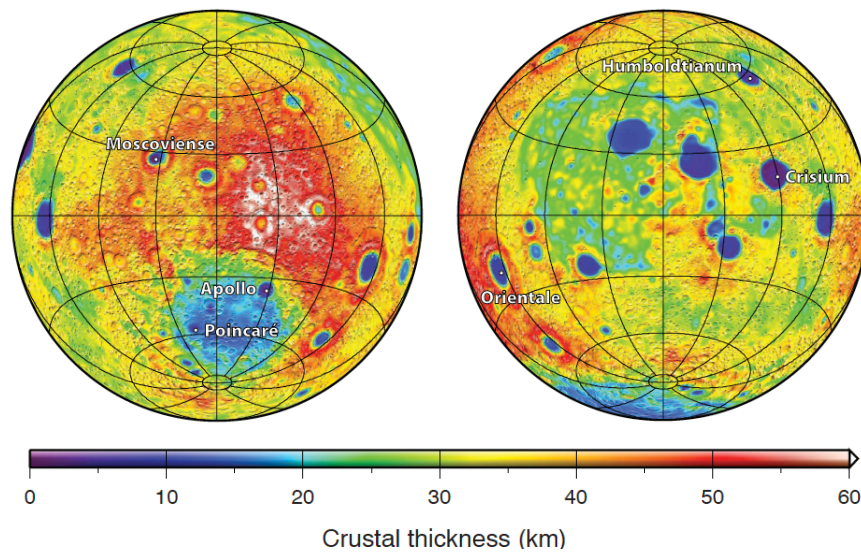


Figure 5.2: Crustal thickness of Moon inferred by Wieczorek *et al.* [10]. Duplicated from section 1.2.1 for convenience. The far side of the Moon (left) has a thicker crust than the near side (right), except for the crust in the SPA basin. The thickness of the crust in the major basins of the near side is close to zero. The Bouguer gravity acceleration in Figure 5.1 was used to compute this crustal thickness and thicker crust coincides with negative Bouguer values while thinner crust coincides with positive values.

region within 40° of the antipode from Earth [21]. Seismic rays originated in the far side might be attenuated by the partial melt layer so they are not observed by the Apollo network in the near side of the Moon or moonquakes might not exist there because of the particular properties of that region.

5.2.2 Lunar evolution

The Moon most likely formed from the debris of the collision between a Mars-sized object and Earth [92–94]. It was initially molten, possibly down to a 1000 km depth [95] due to the energy of the impact, radiogenic heating, and tidal forces, forming a lunar magma ocean (LMO) [96, 97]. As the LMO cooled, it crystallized minerals that were denser (olivine, pyroxene) and lighter (plagioclases) than the remaining liquid. Thus, the last layer to crystallize, rich in incompatible elements (potassium, rare Earth elements, phosphorus, uranium and thorium) formed over a dense ilmenite (Fe-Ti) layer located between the solidified plagioclase crust and olivine mantle [95]. Once crystallized, this layer would have been denser than the underlying olivine-rich mantle [96].

It is believed that a fraction of the incompatible elements (called urKREEP [95]) and ilmenite layer sank to the lower mantle because of gravitational instability, driving a large-scale overturn of the lunar mantle [98, 99]. The urKREEP and ilmenite material might have reached the core-mantle boundary (CMB), possibly forming the partially molten layer inferred by Weber *et al.* [15]. If the urKREEP and ilmenite material became positively buoyant instead, it could have ascended to

shallower mantle. An inefficient overturn or upwelling of the Fe-Ti material could create Fe-Ti rich zones in the lunar mantle [100]

Mallik *et al.* [98] estimated the densities of Fe-Ti partial melts in order to assess the buoyancy and resulting stability of the material at the CMB, finding that a wide range of lower and higher values of density, compared to the density of the lunar mantle, were possible. Scheinberg *et al.* [101] showed that a density contrast from 300 to 500 kg/m³ between the urKREEP layer and the lower mantle would keep the urKREEP material stable at the CMB. Scheinberg *et al.* further proposed that the urKREEP layer could remain molten for several billions of years, forming a metalliferous basal magma ocean from which a high-intensity lunar dynamo could be sustained, with intensities and duration agreeing with the ones inferred from Apollo samples of lunar crust.

Apollo samples of the lunar crust indicate that a magnetic field of approximately 77 μT must have existed between 4.2 and 3.56 Ga with a weaker field of approximately 5 μT existing beyond 2.5 Ga. This observation is significant because core convection alone could not sustain a lunar dynamo for the duration and intensities described [102]. The basalt magma ocean (BMO) proposed by Scheinberg *et al.* [101] and previously described, is one of the mechanisms proposed to increase the magnetic field intensities. In this scenario, the lunar dynamo would be driven by convection in a basal magma ocean near the core-mantle boundary.

For the lower intensity period of the magnetic field, it was proposed that water reservoirs located in the deep mantle would have enhanced the vigor of the lunar core dynamo by reducing the mantle viscosity [103]. This water is most likely

primordial [104], possibly coming from Earth, and the water reservoirs might be located below the 1000 km depth estimated for the lunar magma ocean. Other mechanism that could have increased the intensity of the lunar magnetic field are the removal of a thermal blanket near the CMB [105], impact-induced rotation changes [106] or precession of a lunar inner core [107].

As mentioned before, in this work we remove the prior constraints that interpret gravity variations entirely in terms of shallow density anomalies in order to obtain a 3-D density distribution of the Moon and analyze the similarities and differences between the image we obtain and the one the community has been building up over the years. Constraining the location and magnitude of density anomalies in the Moon with flexible priors might show crustal anomalies in addition to deeper anomalies linked to seismic activity, to an inefficient overturn or upwelling or to water reservoirs of the lunar mantle.

In section 5.3 we describe the inversion algorithm and how it can use minimal prior information and obtain variation and significance measures. In section 5.4, we describe the density anomalies found and explore the measures of confidence of these anomalies. Finally, in section 5.5, we compare the anomalies obtained with this method to the anomalies inferred by others, previously described.

5.3 Method

The Transdimensional Hierarchical Bayesian Object-Oriented Gravity Inversion algorithm, THeBOOGIe is a transdimensional algorithm in the sense that the

number of density anomalies is not fixed *a priori* but it is inferred directly from the gravity data. It is Hierarchical in the sense that the uncertainty of the gravity data, including the modeling error, is estimated through the inversion [108]. Bayesian means that it uses Bayes' theorem to infer which density model better represents the interior based on the gravity data and prior information [64]. In a Bayesian framework, the current knowledge of the interior (prior), the gravity data and the inferred interior structure (posterior), are all modeled as probability distributions. Object-Oriented means that the distribution of density in the interior of a planetary body is parameterized as a collection of finite size objects. The finite-sized objects are Voronoi regions (VRs) that enclose the volume closer to the point i , called nucleus, than to other chosen points (nuclei) inside the sphere [22]. THEBOOGIE outputs a group of density models sampled from the posterior probability distribution of the lunar interior given by the gravity data.

5.3.1 Parametrization of density anomalies and global grid

All shapes of density anomalies can be parameterized using Voronoi regions, assuming the number of nuclei inside the sphere is large enough. The parameters that describe a density model using a Voronoi parametrization are: the number of VRs (n), the location of each nuclei ($\{x\}$, $\{y\}$ and $\{z\}$) and the density value of each region ($\{\rho\}$). The shapes of density anomalies obtained with a VR parametrization is mapped into an underlying tesseroid grid with fixed locations in order to speed up the computation of the gravity field of a given density model. A tesseroid is

the intersection between two latitudes, two longitudes and two concentric spheres. The global tesseroid grid used in this work has $18 \times 36 \times 10$ tesseroid elements. The tesseroids have a 10° size in latitude and longitude and there are 648 tesseroids in each of the 10 layers of the grid. The details of this mapping and the computation of the gravity field are given in section [5.3.3](#).

5.3.2 Prior constraints

THEBOOGIE is implemented through a reversible jump Markov Chain Monte Carlo algorithm. At each step, a density model is proposed with randomly selected parameters from a prior distribution. Different parameter can have different priors. The prior distribution of the location of Voronoi nuclei, for instance, can be uniform in the volume the core-mantle boundary to the surface of the Moon. A density model having VRs with depths randomly sampled in this volume is then saved or deleted based on how similar the gravity field produced by its density distribution is from the input gravity data. The uniform prior distribution of the locations allows the algorithm to find all density models that fit the data independently of where their VRs are. Table [5.1](#) shows the prior distributions used in this work for the location of nuclei v_{loc} , variance of the noise in the input data σ_g^2 , number of Voronoi Regions n and density of each region ρ . The density of each region is not sampled from an uniform distribution but, instead, optimized linearly once the location of the nuclei are sampled. The density values assigned to each Voronoi region are obtained by a constrained linear minimization of the residual within the ranges -500 and 500

	$v_{loc}\hat{r}$	σ_g^2	n	ρ
Min	<i>CMB</i>	$10^{-10} \text{ (m/s}^2\text{)}^2$	1	-500 (kg/m ³)
Max	<i>R</i>	$10^{-1} \text{ (m/s}^2\text{)}^2$	500	500 (kg/m ³)

Table 5.1: Prior distributions used in THEBOOGIE. R is the radius of the sphere. Voronoi regions can exist in the volume between the core-mantle boundary (CMB) and the surface of the sphere. The distributions of σ_g^2 and n do not have tangible limits. We instead set them to sufficiently large values so that the posterior distributions for these parameters are not truncated. The density of the Voronoi regions obtained by reducing the residual between the gravity acceleration produced by the density model and the input gravity data. This is constrained linear optimization between the ranges of -500 and 500 kg/m³.

kg/m³.

5.3.3 Ensemble of density models

The output density models of THEBOOGIE are a sample of the posterior density distribution that fit the input data very well, selected from the pool of density models that fit the prior distribution. This group of output models is called the ensemble. The mean of the ensemble and its standard deviation will be used to summarize the content of all these models in section 5.4. Equation 5.1 shows the likelihood used to quantify the fit of each model.

$$\text{likelihood} = \frac{|\tilde{C}_m|^{1/2}}{(\sigma_g^2)^{s/2}(\rho_{\max} - \rho_{\min})^n} \exp\left(-\frac{\Phi}{2}\right) \quad (5.1)$$

Where σ_g^2 is the noise variance of the input gravity data $\{g\}$, s is the number of data points of $\{g\}$, n is the number of Voronoi regions of the model, ρ_{\max} and ρ_{\min} are the limits of the density of the regions shown in table 5.1. \tilde{C}_m is the posterior covariance matrix, $\tilde{C}_m = (D^t C_g^{-1} D + C_m^{-1})^{-1}$, where D is a function of the gravitational constant

and distances of the Voronoi regions to the observation points fitting $\{g\} = D \times \{\rho\}$, C_g is the data covariance matrix ($C_g = \sigma_g^2 I$) and C_m is the prior model covariance matrix. Φ is the misfit between the gravity data produced by the model $\{g_m\}$ and the input gravity data $\{g\}$ (equation 5.2).

$$\Phi = (\{g\} - \{g_m\})^T \frac{1}{\sigma_g^2} (\{g\} - \{g_m\}) \quad (5.2)$$

The gravity field of the density model proposed at iteration i , $\{g_m\}$, is calculated by mapping the Voronoi regions into an underlying tesseroid grid [109]. Once the location of the Voronoi regions are defined, the tesseroids having its center within the VR are assigned the density value of the VR. The gravity acceleration of each tesseroid is pre-computing following Uieda *et al.* [68] and updated with the corresponding density value assigned to the corresponding VR at iteration i .

At each iteration, the algorithm creates model m' by sampling the value of its parameters from the prior distributions described in section 5.3.2 and compares how well or bad it fits the data relative to a previously saved model m . Model m' is saved with a probability $\alpha = \min(1, \text{likelihood}'/\text{likelihood})$. According to equation 5.1, the probability of keeping model m' increases if ϕ' , $\sigma_g'^2$ and n' are smaller than ϕ , σ_g^2 and n , respectively. Keeping everything else constant, the algorithm prefers to keep models that have fewer Voronoi regions. This is a fortuitous consequence of parsimony and the fact that an increasing number of VRs increases the computational time of the inversion so the additional VRs are only valuable if they improve the fit of the model to the input data.

Instead of having one model of the interior, the output of this inversion approach are thousands of models, each one containing n Voronoi regions, their locations and density values. This vast amount of information can be presented in different ways in order to help visualize the similarities and differences between models of the interior of the Moon which show the amount of variation in the parameters of density models allowed by the input gravity data.

The mean density model is obtained by averaging the density values of all output models within each tesseroïd of the grid and shows the most likely value of the density at that location. The standard deviation of the density values at each tesseroïd (σ_ρ) shows how much or little the value in that location can change while still fitting the input data. Tesseroïds with densities that vary greatly across models in the ensemble have less well constrained density than tesseroïds with lesser variations.

$$D_{KL}(p|q) = \sum_{i=1}^N p(\rho_i) \log \left(\frac{p(\rho_i)}{q(\rho_i)} \right) \quad (5.3)$$

The Kullback-Liebler divergence D_{KL} (Equation 5.3) shows how similar or different the posterior probability distribution of density at tesseroïd i , $p(\rho_i)$, is from its prior distribution $q(\rho_i)$ [72]. A tesseroïd with high values of D_{KL} has a distribution of density values very different from the prior one which implies that imposing constraints from input gravity data has added information on the density at that location. A tesseroïd with a low value of D_{KL} indicates that the input data might not be sensitive to that location, therefore, it is impossible to confidently interpret the density in this location. The mean density, standard deviation and Kullback-

Liebler divergence will be the measures used throughout this work to represent the information contained in the output density models of THeBOOGIe.

5.3.4 Input GRAIL gravity acceleration data

Equation 5.4 shows the expression for the radial component of the gravity field as a summation of spherical harmonic coefficients C_{lm} . G is the gravitational constant, M is the mean mass of the body, R is its radius and r , θ and ϕ are the altitude, latitude and longitude of the observation point \mathbf{r} . C_{lm} is the spherical harmonic coefficient of degree l and order m and $Y_{lm}(\theta, \phi)$ are spherical harmonic functions of the corresponding coefficients at the location given by the latitude θ and longitude ϕ . We use the spherical harmonic coefficients obtained by Lemoine *et al.* [47] using data from the GRAIL mission. and a grid of points uniformly distributed over the sphere as input in equation 5.4 in order to produce the set of gravity acceleration values used as input in THeBOOGIe. The grid has a total of 10242 points at a altitude of 100 km over the surface of the sphere and the summation in equation 5.4 was truncated to degree $l = 100$ in order to include the degrees corresponding to that spatial resolution and avoid aliasing.

$$g(\mathbf{r}) = \frac{GM}{r^2} \sum_{l=0}^{100} \sum_{m=-l}^l \left(\frac{R}{r}\right)^l (l+1) C_{lm} Y_{lm}(\theta, \phi) \quad (5.4)$$

The location of each of the 10242 points where $g(\mathbf{r})$ is calculated, is saved and the output density models of THeBOOGIe should produce similar values when their radial gravity acceleration is sample at these points.

5.4 Results

TheBOOGIe algorithm was used to run seven parallel inversions of the same gravity acceleration data described in section 5.3.4. The mean radius of the Moon was considered to be $R = 1739$ km. Each inversion starts from a different density model, selected randomly from the prior. If the output models obtained from these seven inversions are similar, then the inversion results can be considered to not depend on the starting model. Figure 5.3 a shows the logarithm of the likelihood at each iteration for the seven inversions. The likelihood increases at each iteration until it stabilizes around iteration 2.1×10^6 . A closer look into iterations $2.1 \times 10^6 - 3 \times 10^6$ (Figure 5.3 b) shows that there is some variation between the likelihood of models within the same inversion and that models from different inversions have slightly different likelihood values. However, since the variations of the likelihood after iteration 2.1×10^6 are much smaller than the initial variations, the algorithm is considered to have converged and models obtained after iteration 2.1×10^6 are then representative of the interior density distribution of the Moon as constrained by the input gravity data .

The gravity acceleration of all output models is calculated and averaged in Figure 5.3c. This average shows gravity acceleration features related to the crustal thickness variations shown in figure 5.1. The misfit between the input gravity data and the mean gravity acceleration data of the output models (Figure 5.3d) shows that the fit between these two data sets is very good, with the largest differences found at small-scale circular features. The mean gravity of the output models cannot

fit these small scale gravity features because the low resolution of the tesseroïd grid.

5.4.1 Mean density anomalies and confidence

Figures 5.4 and 5.5 show the mean density model obtained as an inversion of the input gravity data described in section 5.3.4 where unconstrained values are grayed out according to two different criteria, the standard deviation σ_ρ and the Kullback-Liebler divergence D_{KL} . As mentioned before, the mean density model is the mean density value μ_ρ in each tesseroïd of the output models across the seven inversions. The criterion $|\sigma_\rho/\mu_\rho| < 1$ shows the tesseroïds with small density variations relative to their mean and the criterion $D_{KL}/\max(D_{KL}) > 0.5$ shows the tesseroïds with a large normalized Kullback-Liebler divergence which have a distribution of density different to the prior distribution.

Figure 5.4 shows that the σ_ρ criteria considers density values in most of the tesseroïds unconstrained, with the exception of few density features. In layers 1-6 (depths 0-507 km), these features are density anomalies clearly related to the far side thick crust, SPA basin and major near side basins. Layers 7 - 10 (depths 507-1409 km) show positive density anomalies not related to any surface feature. Figure 5.5 shows that the significance of the density values at each tesseroïd decreases with depth. Most tesseroïds in the first five layers have density values with a distribution significantly different from an uniform one while tesseroïds in layers 7-10 do not. Within layers 1-5, the far side of the Moon is better constrained than the near side.

The location of positive density anomalies in the mean model coincide with the

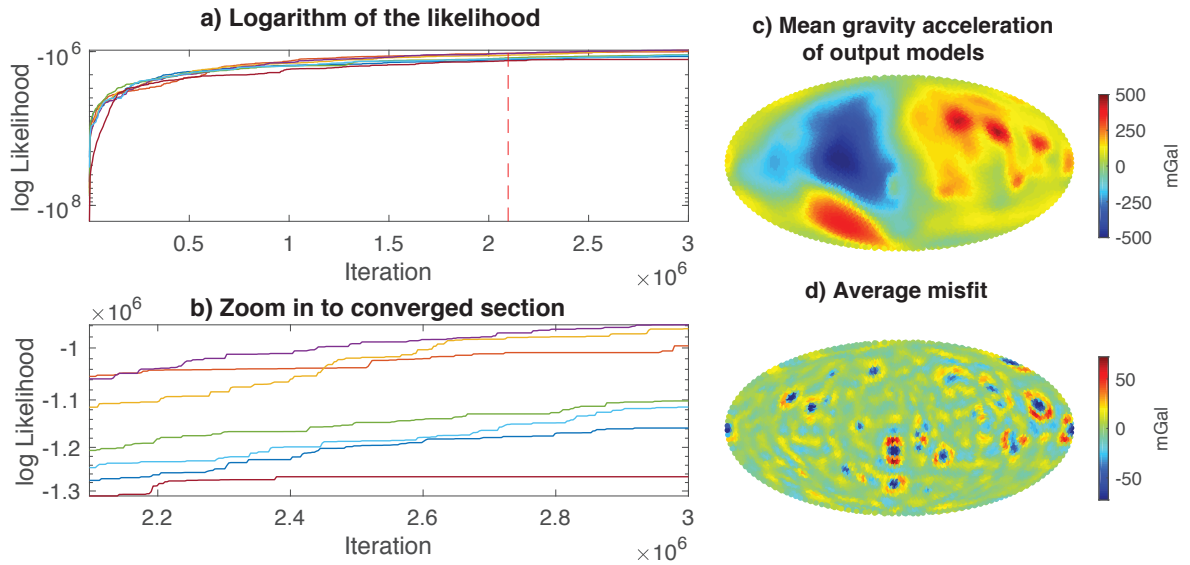


Figure 5.3: **Convergence and fit of the output models to the input gravity data.** a) For each of the seven inversions with different initial density models (lines of different color), the likelihood increases per iteration and stabilizes after iteration 2.1×10^6 . The inversion is said to have converged at this point. b) The likelihood of most inversions keep increasing after iteration 2.1×10^6 but their variations are still much smaller than before this number of iterations. Density models obtained after convergence are the output models of THEBOOGIE. c) The mean gravity acceleration of the output models shows gravity features related to the crustal dichotomy, SPA basin and major lunar mascons. d) The average misfit shows that the gravity data in a) fits the input gravity data very well. With differences in the range of -50 to 50 mGal. The largest differences between the data in c) and the input gravity data are located near smaller scale impact craters of the Moon. The low resolution of the tesseroïd grid makes it impossible to have density anomalies of this size in the output models.

location of positive Bouguer gravity anomaly (Figure 5.1) and thinner crust (Figure 5.2). As mentioned in section 5.2, a shallower crust-mantle boundary produces a positive gravity anomaly in the surface because there is more high density mantle material and less low density crustal material than in a location with a deeper boundary. The inversion algorithm is then able to find density anomalies that fit the expected crustal thickness variations while also finding anomalies at a deeper location than the crust-mantle boundary depth.

The lateral variations between the density distribution found by THeBOOGIE and the lateral variations of crustal thickness are very similar while the density anomalies in the mean model are thicker and have a lower magnitude than the ones expected by crustal thickness variation alone. Both Figures 5.4 and 5.5 show that the density anomalies related to the far side crust, SPA and near side basins in the mean model have a thickness of 507 km (layers 1-6) and the magnitude of the density anomalies are less than 200 kg/m^3 . By contrast, Wieczorek *et al.* [10] inferred crustal thickness ranges from 0 to 60 km and magnitude of crustal density anomalies from 1000 to 400 kg/m^3 . The tradeoff between thickness and density value of shallow features was expected because of the non-uniqueness of gravity inversions. The same gravity signal can be matched by modifying the thickness or modifying the density value.

Figure 5.6 shows the distribution of density values of the ensemble at 30 tesseroids chosen randomly. The row of the tesseroids indicate the layer they belong to. With the first row of tesseroids belonging to the first layer and so on. The red line shows the mean value shown in the maps of Figures 5.4 and 5.5, the black line

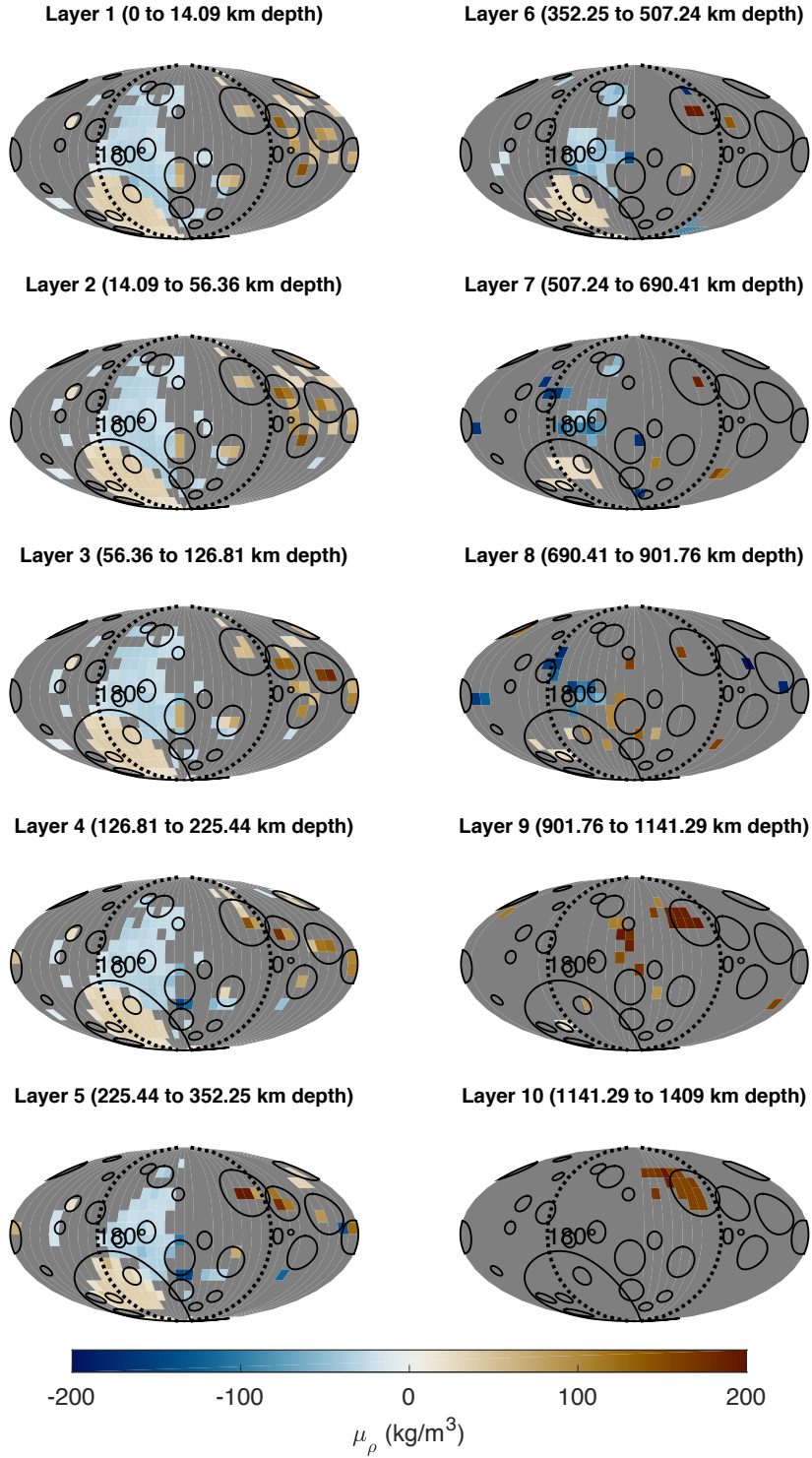


Figure 5.4: Mean density model with grayed out area indicating the location of tesserooids with a very high standard deviation (σ_ρ) relative to their mean value (μ_ρ). The criteria $|\sigma_\rho/\mu_\rho| > 1$ is used to select which tesserooids to gray out.

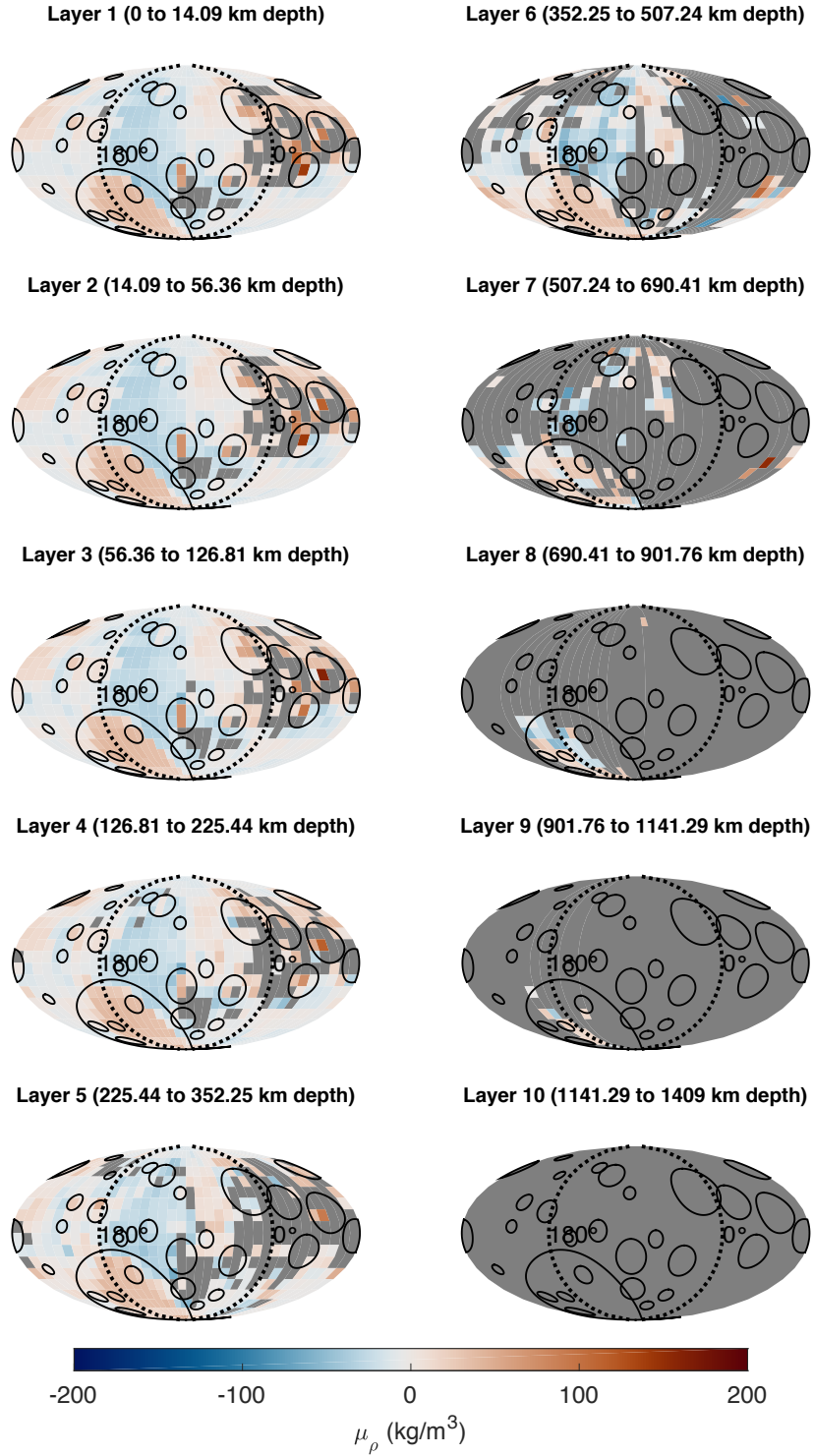


Figure 5.5: Mean density model with grayed out area indicating the location of tesseroids with a very low Kullback-Liebler divergence (D_{KL}). The criteria $D_{KL}/\max(D_{KL}) < 0.5$ is used to select which tesseroids to gray out.

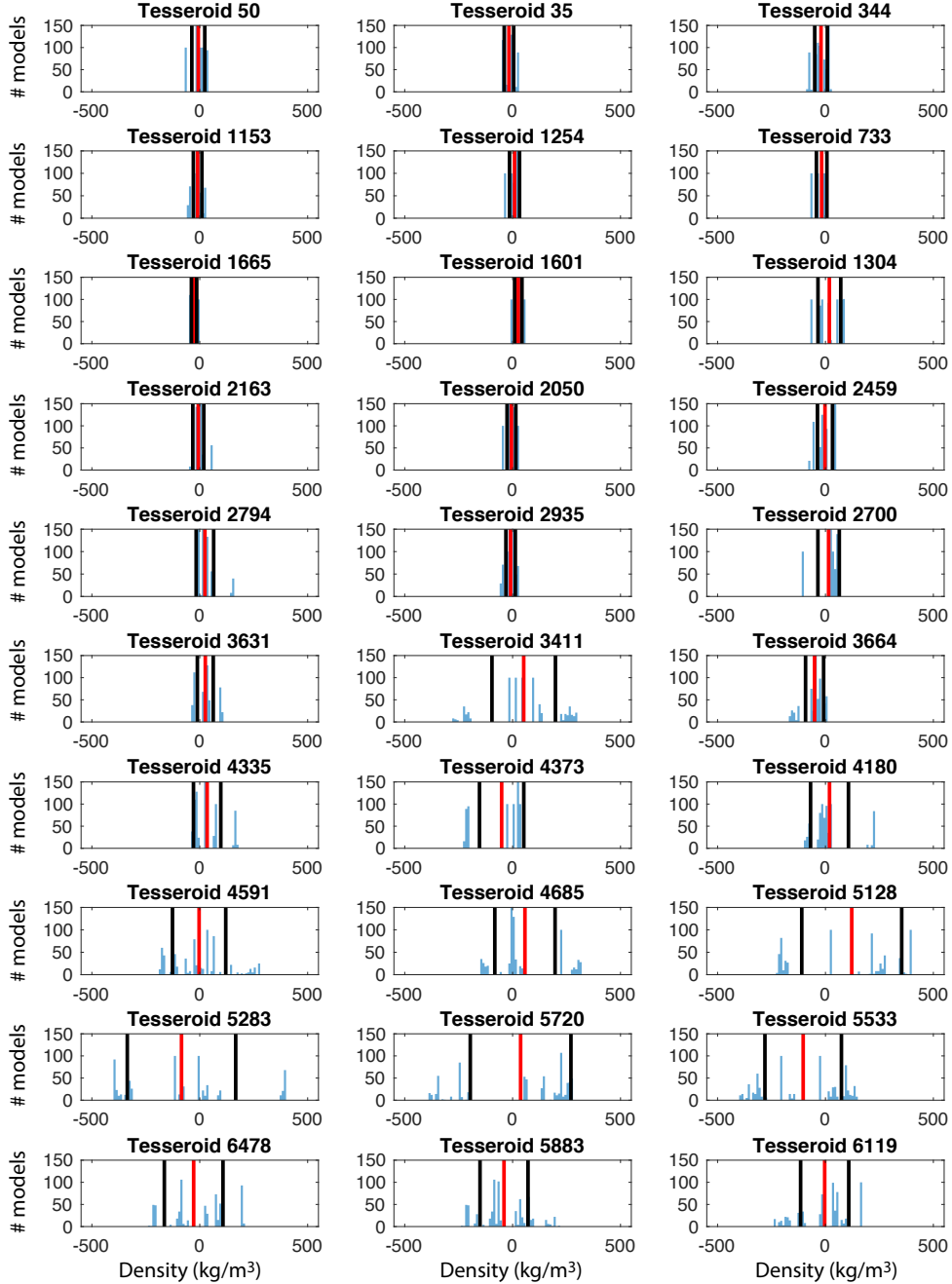


Figure 5.6: Distribution of density values of the ensemble at 30 tesserooids. Each row corresponds to tesserooids at the same layer, with the first row corresponding to layer 1 and the last row to layer 10. The red line shows the mean density of the ensemble at tesserooid i (value shown in Figures 5.4 and 5.5) and the black line shows the standard deviation of the ensemble at the same tesserooid. The distribution of density values is not normal in some tesserooids and the mean and standard deviation parameters do not provide a complete description of the distribution. The histogram of each tesserooid is needed to fully understand the variations of density at each location.

shows the standard deviation and the blue bars show the number of models having density ρ in that tesseroïd. Many of these histograms show that the distribution of density values per tesseroïd is not Gaussian, especially in the deeper layers.

The distribution of density values in the ensemble is not necessarily Gaussian because the value of density is obtained by a least-squares optimization of the residual once the location and size of the Voronoi region is obtained. If the size of the VR changed abruptly from one model to the other, then its density value also changes abruptly. The bayesian approach of this gravity inversion allows us to see the full distribution of density values per tesseroïd which does not need to be parametrized into a normal distribution, however, this vast amount of information is difficult to analyze for all 6480 tesseroïds in the grid. We explore next other alternatives for summarizing the information obtained.

5.4.2 Correlation between density anomalies in the output models

Figure 5.7 shows the correlation coefficient between the density values of tesseroïds in the grid. Tesseroïd indexes are random variables and the density anomalies from different density models are observations. The x and y axes show the tesseroïd indexes of the 6480 tesseroïds in the grid. White grid lines are placed every 648 tesseroïds, showing the boundaries of all ten layers in the grid. The correlation value c_{ij} in the plot shows the correlation coefficient between tesseroïd i and tesseroïd j with light blue values showing anti-correlation and light green values showing positive correlation. The main diagonal of the plot has values $c_{ii} = 1$.

There are three sections in the plot with similar correlation values. The first section contains tesserooids from layers 1 to 5 (tesserooid indexes 1-3240 vs tesserooid indexes 1-3240) with mostly positive correlation values. The second section is formed by tesserooids in layers 6 to 8 vs all other layers (tesserooid indexes 3241-5184 vs tesserooid indexes 1-6480). These tesserooids are not clearly correlated or anti-correlated, having low magnitude correlation coefficients. The third section is formed by tesserooids in layers 9 and 10 vs tesserooids in layers 1 to 5 (tesserooid indexes 5185-6480 vs tesserooid indexes 1-3240) that are anti-correlated.

In the first five layers of the grid, there are groups of tesserooids that change their density value together, if the density in one tesserooid decreases, the density of the rest of the tesserooids in the group do too. Tesserooids in layers 6 to 8 are not correlated to any tesserooid in any other layer. Their density value varies independently of the values of other tesserooids. Tesserooids in layers 9 and 10 increase or decrease their value in opposite way as the ones in layers 1 to 5.

Figure 5.8 shows a zoom in to sections a and b highlighted in Figure 5.7. Section a of figure 5.8 shows the correlation between tesserooids in the first layer of the grid. The tesserooids indexes enclosed by the red squares correspond to the near side Mare region and tesserooids in the green square correspond to the SPA basin. Although not all tesserooids in these squares have positive correlation values, most do, indicating that there are density structures related to the SPA basin and near side mare in layer 1. Since the correlation pattern between tesserooid indexes 1-3240 and tesserooid indexes 1-3240 is similar to the one in section a, the structures related to the SPA and near side mare present in layer 1 are also present in layers 2 to 5.

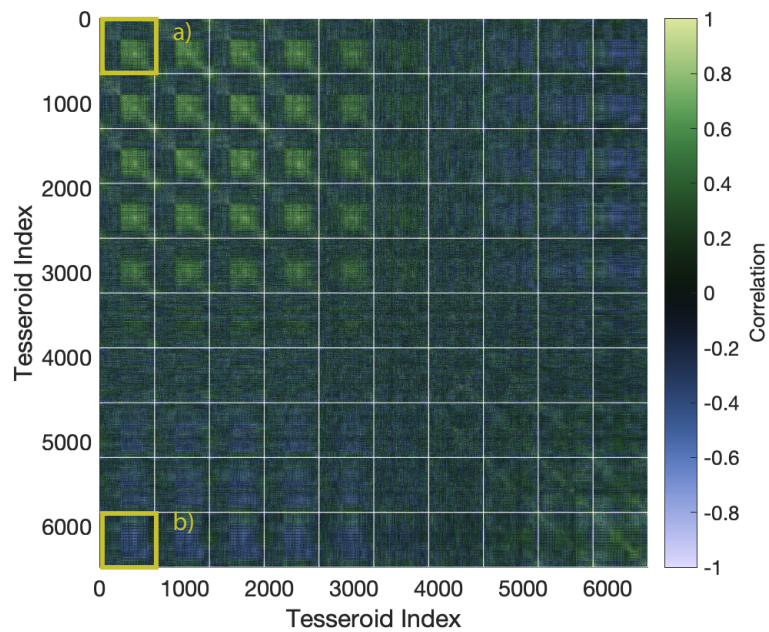


Figure 5.7: Correlation of the density values at tesseroids of the grid. White grid lines show the boundary between layers. There are three main features in the correlation matrix. Most tesseroids in layers 1 to 5 are positively correlated between each other. Tesseroids in layers 6 to 8 are not correlated to tesseroids in any other layer. Tesseroids in layers 9 and 10 are anti-correlated to tesseroids in layers 1 to 5. Sections a and b are zoomed-in in figure 5.8.

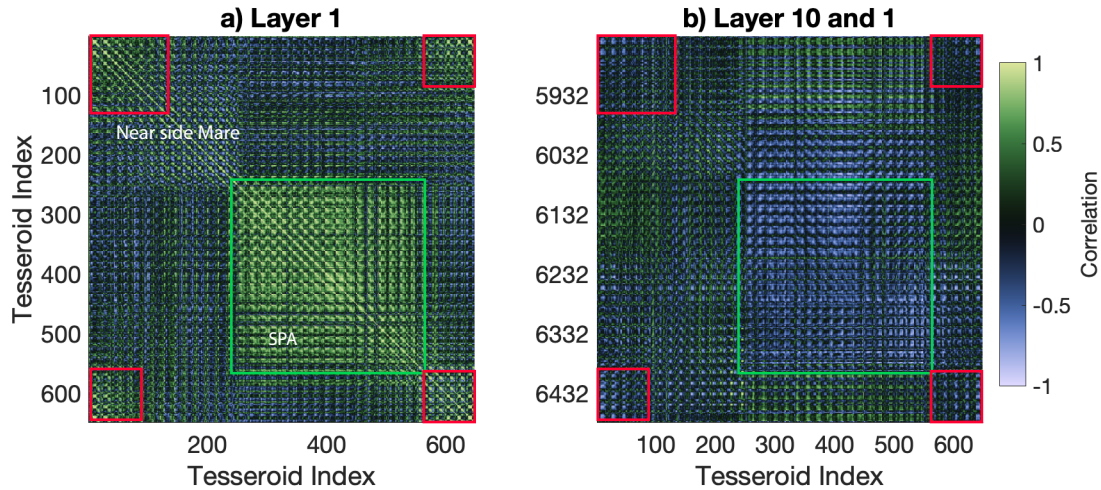


Figure 5.8: Zoom in to correlation values of sections a and b in figure 5.7. a) Correlation between tesserooids in layer 1. The red and green squares highlight the tesserooids with the most positive correlation values. They are located in the nearside Maria (red) and the SPA basin (green). b) Correlation between tesserooids in layer 10 and 1 with corresponding squares highlighting the most negative correlation values. These two correlation plots show that the tesserooids in the nearside Maria and SPA basin regions change their density in the same direction as a group while the density of the corresponding regions in layer 10, change to the opposite direction.

Section b of figure 5.8 shows the correlation values between tesserooids in layer 10 and tesserooids in layer 1 with tesserooids enclosed by the red and green squares having the same latitude-longitude than the ones enclosed by the corresponding rectangles in section a. The tesserooids at the deepest layer are anti-correlated to the tesserooids at the shallowest layer which means that if tesserooids in the SPA basin region (layer 1) have a higher density value in one density model, the tesserooids in the corresponding latitude-longitude in the deepest layer of the same model have a lower density value.

Figure 5.9 shows maps and cross-sections of the correlation values between the density anomaly in one chosen tesserooid and others. The star shows the location of

the chosen tesseroid. The red line shows the location of the cross-sections. Tesseroids near the star are positively correlated and tesseroid far away are not correlated or anti-correlated. This behavior occurs in all maps and cross-sections and supports the correlation pattern found in Figure 5.8.

If shallow tesseroids are anti-correlated with deeper tesseroids, then there might be a depth that shows the boundary between shallow density features and deeper features. The radial correlation (R_ρ) and correlation length (ρ_ρ) have been used before to find depth boundaries based on the correlation between features at the same range of depths [110–112].

Equation 5.5 shows the expression to calculate the radial correlation between the density values at locations $r = r_1$ and $r = r_2$. $\rho(r_1)$ is the density at $r = r_1$, $\mu_\rho(r_1)$ is the mean of the density and $\sigma_\rho(r_1)$ the standard deviation at that radius.

$$R_\rho(r_1, r_2) = \frac{\mathbb{E}[(\rho(r_1) - \mu_\rho(r_1))(\rho(r_2) - \mu_\rho(r_2)))]}{\sigma_\rho(r_1)\sigma_\rho(r_2)} \quad (5.5)$$

The correlation length $\rho_\rho(r)$ shows the rate at which the structure present at a location r decorrelates in the radial direction. Specifically, the correlation length is the distance from r , δr , at which the radial correlation is equal or less than 0.75. Equation 5.6 shows the exact expression for $\rho_\rho(r)$.

$$\rho_\rho(r) = \min[|\delta r| : R_\rho(r - \delta r, r + \delta r) \leq 0.75] \quad (5.6)$$

Figure 5.10a shows the radial correlation (R_ρ) between layers of the mean density model. Figure 5.10b shows the mean radial correlation of all output density

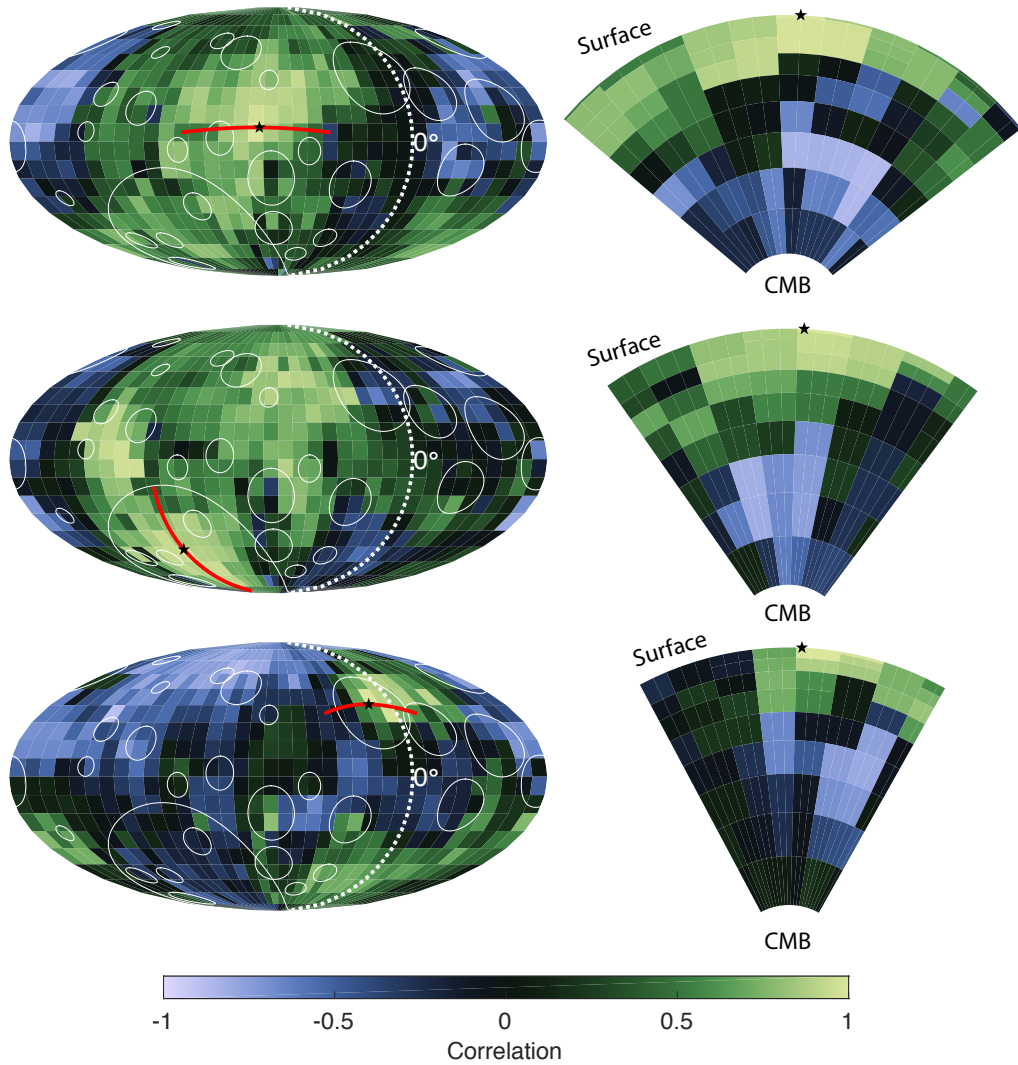


Figure 5.9: Map of the correlation values between the tesseroïd at the location of the star and all other tesseroïds at layer 1 (0 to 14 km depth) and cross-sections in depth. The red line shows the location of the cross-section in the map. Tesseroïds near the star are positively correlated while tesseroïds far away (in different latitudes and longitudes or in the deepest layers) are anti-correlated.

models of the THeBOOGIe. Figure 5.10c shows the standard deviation of the radial correlation between output density models, as complementary information of Figure 5.10b. With some small differences, both the radial correlation of the mean model and the mean radial correlation of the output models show that: the first (shallow) layers are positively correlated between each other; some layers immediately below them are not correlated with the shallow layers and some deeper layers are anti-correlated with the shallow layers.

Figure 5.11 shows the correlation lengths calculated as a function of the radial correlation of the mean model (blue line) and the mean radial correlation of the output models (red line). The depth of the minimum of the correlation length is indicative of a boundary depth since the structures at this depth are different from the structures immediately above or below them. The minimum correlation length given by the radial correlation of the mean model is located at the boundary between layer 5 and layer 6 (black line), at a depth of 352 km. The minimum given by the mean radial correlation of the output models is located in the boundary between layer 4 and 5 (orange line), at a depth of 225 km. The slice of the mean density model in Figure 5.11 shows the location of the two boundaries found. We choose the black boundary given by the radial correlation of the mean model as the better fitting one. This boundary matches the limit between the low magnitude shallow density anomalies and the higher magnitude, smaller scale density anomalies below them.

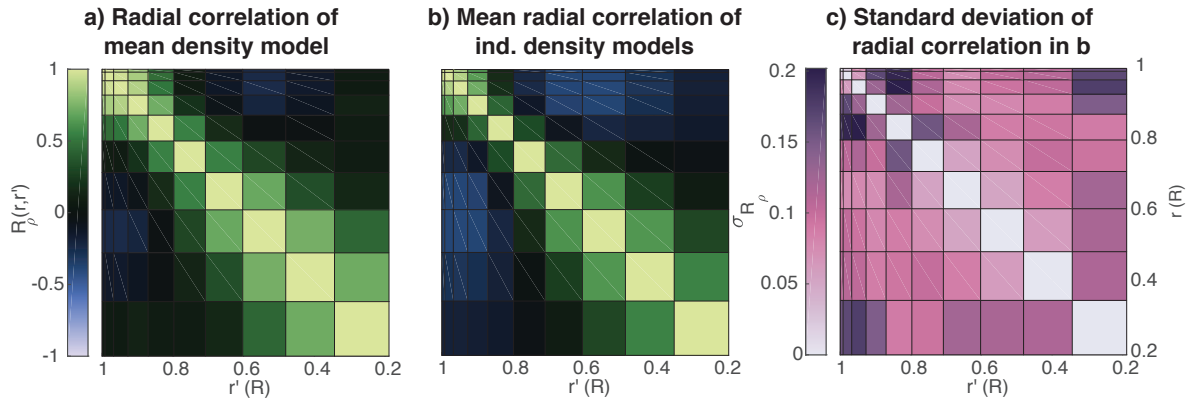


Figure 5.10: Radial correlation analysis. a) The radial correlation of the mean density model show that the first five layers are positively correlated between each other, slightly anti-correlated with layer 8 and not correlated to layers 6, 8, 9 and 10. b) The mean radial correlation of individual models in the ensemble show that the first four layers are positively correlated between each other, slightly anti-correlated with layers 7, 8 and 9 and not correlated to layers 5, 6 and 10. c) The standard deviation of the mean radial correlation show that the radial correlation values between layer 5 and layers 1, 2, 3 have the highest variation, followed by the correlation values between layer 10 and layers 1, 2, 3 and 4.

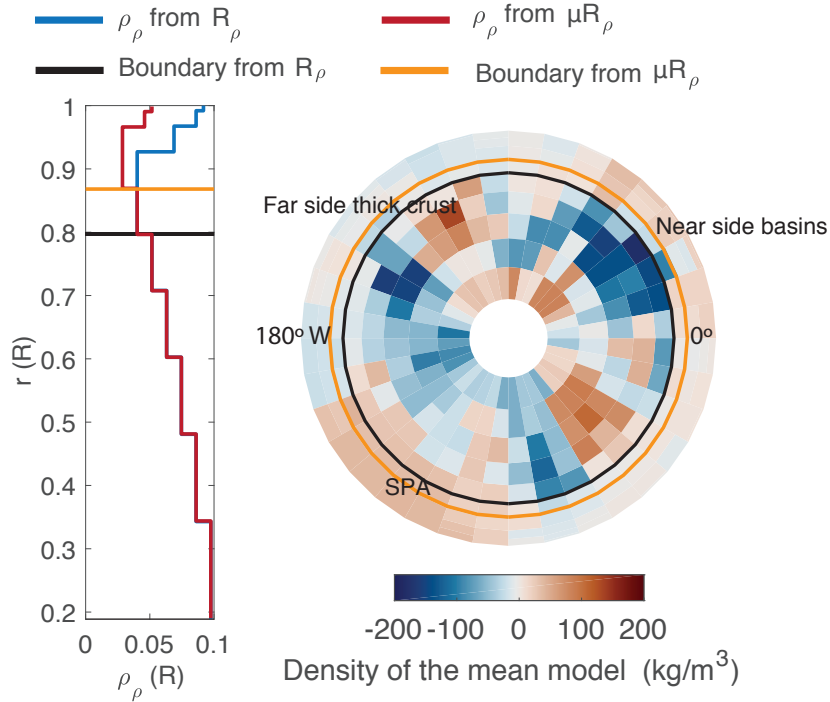


Figure 5.11: Correlation length ρ_ρ and corresponding boundary of the mean density model. ρ_ρ is a function of the radial correlation R_ρ and shows the distance at which layers are no longer correlated. A small value of ρ_ρ means that the density distribution immediately above or below r , is very different from the one in r . The blue line is calculated from the radial correlation of the mean density model (figure 5.10 a) and the red line from the mean radial correlation of the individual models in the ensemble (figure 5.10 b). Their minimums indicate a boundary at $0.8R$ and $0.88R$, respectively. The slice of density values show that the boundaries effectively divide the mean density model into distinct regions.

5.4.3 Cluster analysis of density anomalies in the mean model

A cluster analysis provides a way to quantify patterns in a data set. There are 648 density profiles of the mean density model, each one showing what is the density value at the 10 different layers of the grid. Clustering the density profiles would show regions that have a similar distribution of density per depth. Since there is a boundary between shallow and deep tesseroids given by the correlation length, the clustering is done in the density profiles above the boundary (648 density profiles of layers 1-5) separately from the clustering of the density profiles below the boundary (648 density profiles of layers 6-10). The features found in the clustering of the first five layers will be called shallow features while the ones found in the deepest five layers will be called deep features.

We use a k-means algorithm [113] and a Euclidean metric to classify density profiles into n_c clusters. The k-means algorithm requires specifying n_c . Different values of n_c were tested (2-11) and the final value used in this section was chosen based on how robust the assignment of models to clusters was. If more clusters are used than what is justify by the data, then the resulting assignment of density profiles to clusters is dependent of the initial conditions of the algorithm. Density profile i can sometimes be assigned to cluster c and sometimes to cluster d , for example. The value of n_c used for the clustering of the shallow layers is 6 while the one used for the clustering of the deep layers is 3.

5.4.4 Shallow density anomalies

Figure 5.12 shows the topography of the Moon (a), the mean density of the output models at layer 1 (b) and the location of members of the six clusters of shallow density profiles (c). The topography is plotted in the same grid as the mean density with light yellow colors showing positive topography and light blue colors showing negative topography. Zero topography shows the reference radius of 1739 km. The k-means algorithm groups the density profiles into six clusters and these clusters match the location of surface features.

Cluster 1 contains density profiles of the SPA basin, confidently recovered by the inversion algorithm, while containing some near side profiles which are not confidently recovered. Cluster 2 and 3 contain most of the unconstrained density profiles which coincide with topography near zero. Cluster 4 contain the density profiles at the center of the major near side basins: Imbrium, Serenitatis, Crisium, Smythii and Nectaris. They coincide with positive density anomaly and low elevation. Cluster 5 is mostly formed by the density profiles of the highlands and low density of the far side. Cluster 6 contains the density profiles at the center of the Orientale and Humorum basin which are well constrained by the input gravity data and some unconstrained density profiles in the near side. Although not perfectly, the clustering of shallow density profiles finds six clusters with density distributions linked to surface features of the Moon.

Figure 5.13 shows the mean density profile and the related standard deviation of each cluster. The mean of each cluster is plotted in colors corresponding to the

ones used in the map of Figure 5.12c while the standard deviation is plotted in light pink. The standard deviation used in Figure 5.13 should not be confused with the standard deviation used to gray out tesseroids in the mean density maps of Figure 5.4. The one used in Figure 5.13 represents the variation of density between members of the same cluster, which are all part of the mean model while the one used in Figure 5.4 represents the variation of density between output models of the inversion algorithm.

Having clusters of density profiles allow us to analyze the distribution of density per depth for each type of feature, individually. The density anomaly of the SPA basin (cluster 1), for example, is positive and its magnitude does not change much from layers 1 to 5. The density anomaly of the near side basins is also positive from layers 1 to 5 but there is more variation per layer than there is for the SPA basin. Layer 1 of the mean model (Figure 5.12b) shows that the density anomaly at each basin is different which causes this variation within cluster 4. However, the relationship between increasing depth and increasing density (down to layer 5) is similar for the five major near side basins Imbrium, Serenitatis, Crisium, Smythii and Nectaris. The density of the highlands is negative and its magnitude does not change much per layer. The density of the Orientale and Humorum basins is positive in the shallowest layers and decreases per depth until it becomes negative in layer 5.

Figure 5.14 shows the density profile at the center of 28 lunar basins. The outline of each basin is plotted in the maps throughout this work (Figure 5.12b, for example). The location and size of each basin was provided by Neumann *et*

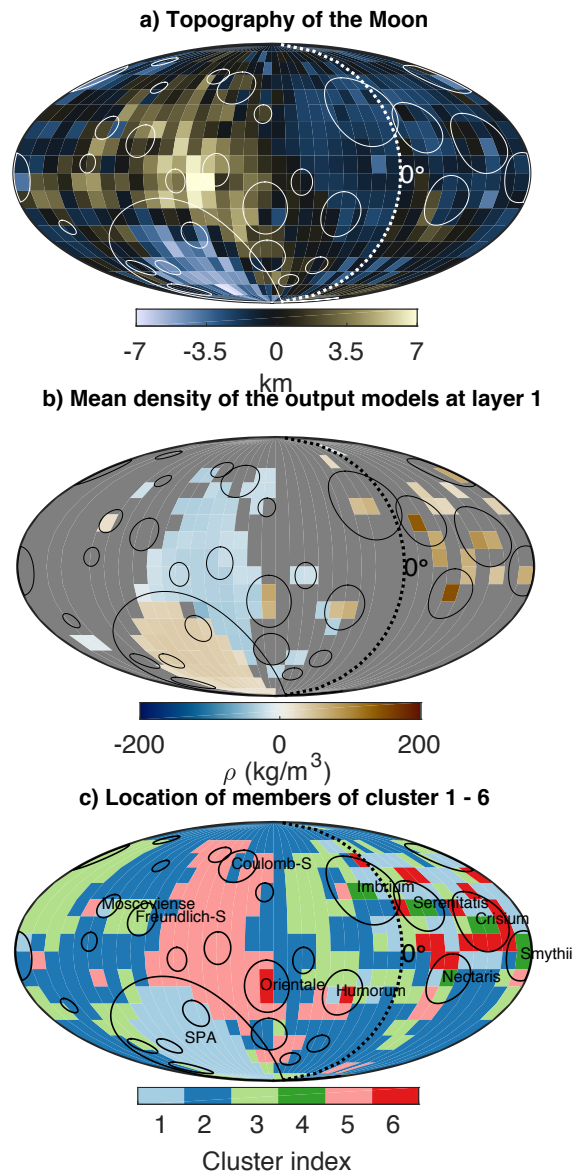


Figure 5.12: Topography of the Moon (a), mean density of the output models at layer 1 with grayed out tesseroids having very large standard deviation (b) and location of clusters obtained from classifying tesseroids in layers 1 to 5 of the mean model (c). Although not perfectly, the clustering identifies groups of density profiles that match the location of surface features in the Moon.

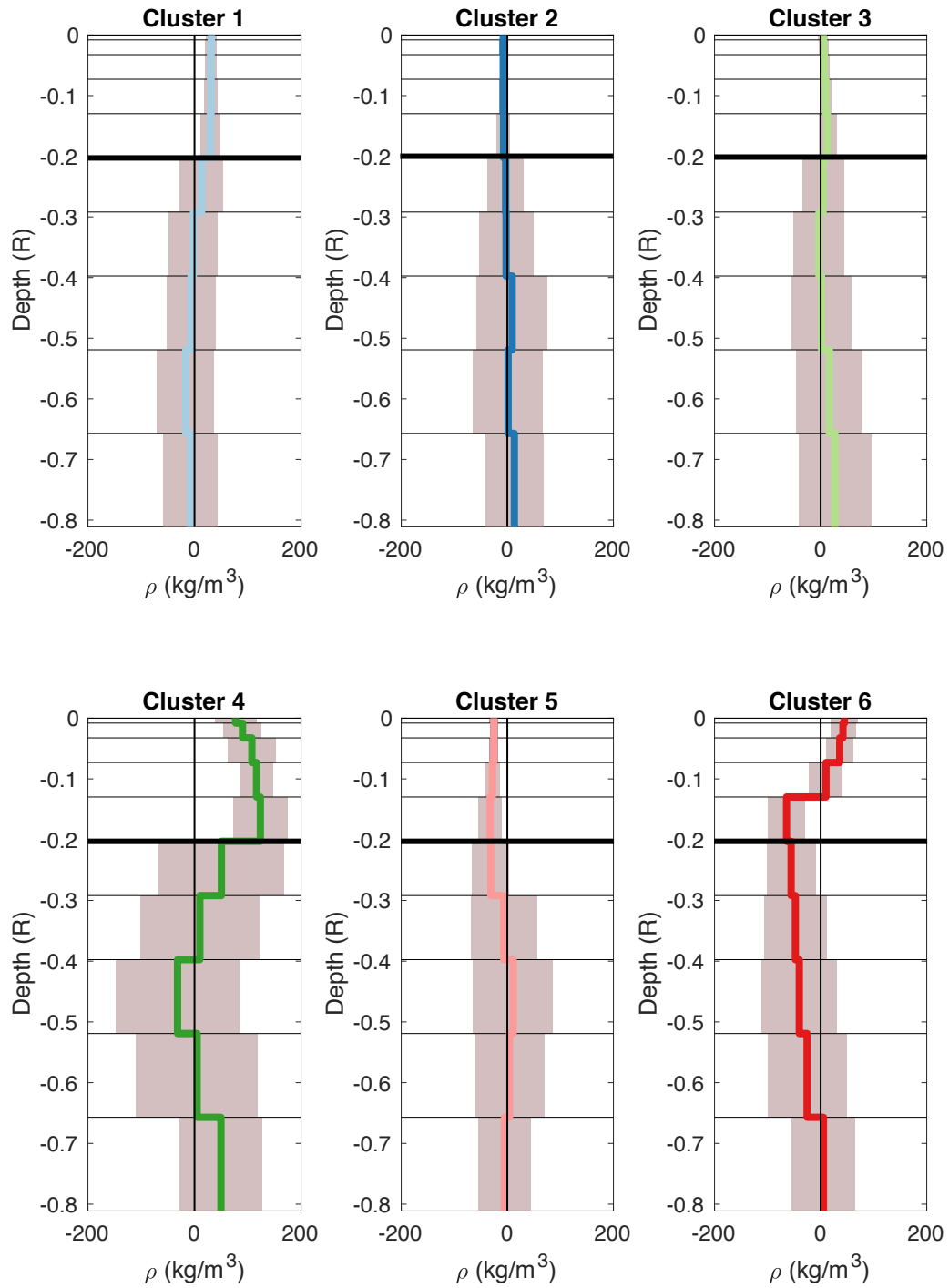


Figure 5.13: Density profiles of the mean model classified into six clusters and their respective standard deviation. The color of the mean of the cluster correspond to the ones used in Figure 5.12. The standard deviation shows the variations of density value per layer between members of the same cluster.

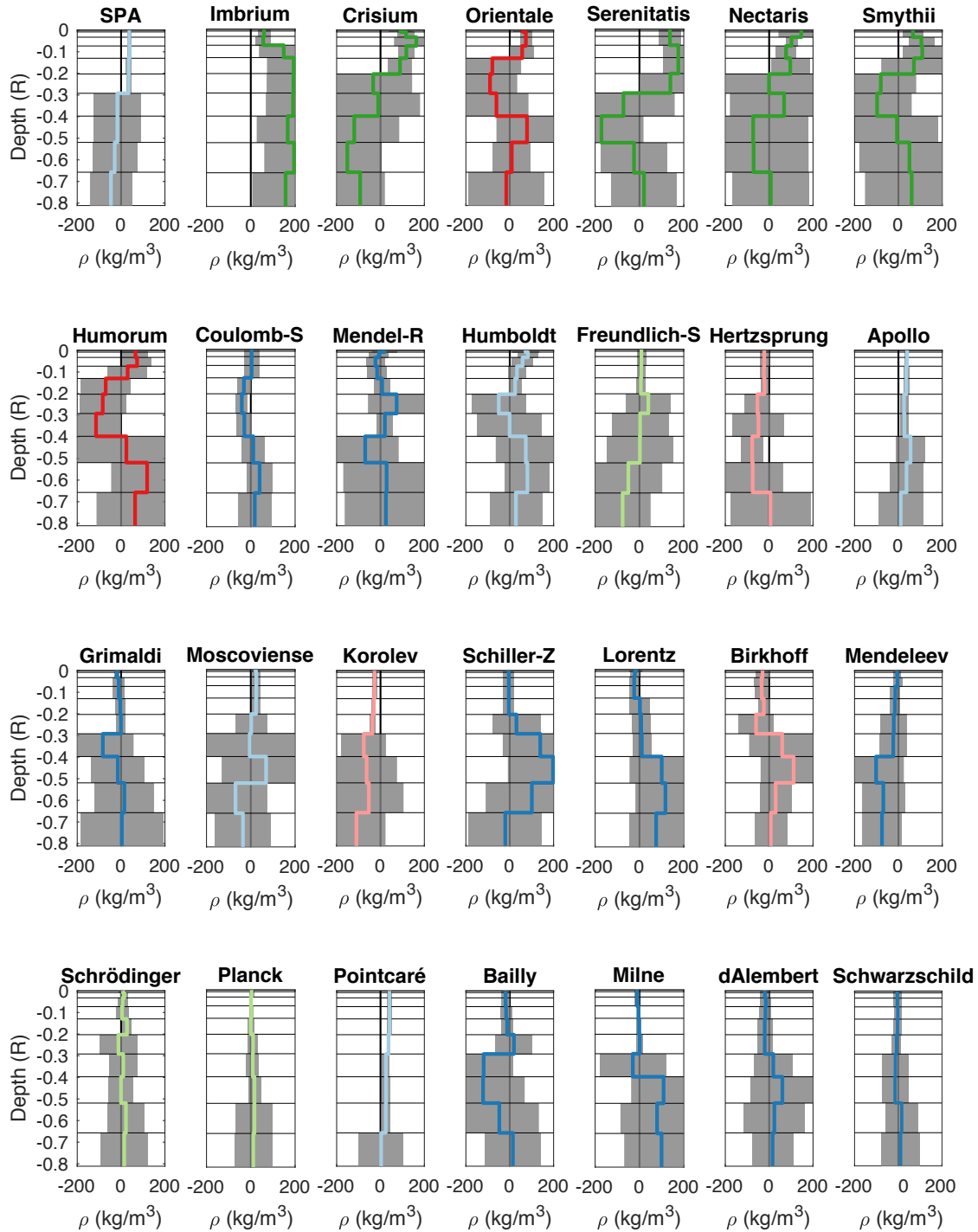


Figure 5.14: Density anomaly of the mean model and standard deviation of tesserooids at the center of 28 lunar basins. The standard deviation shows the variation of density anomaly between the output models. The color of the density profiles show the cluster at which they belong to. The lunar basins appear in decreasing order of diameters size with SPA first having the largest diameter and Schwarzschild last, having the smaller diameter.

al. [40]. The color of the density profile correspond to the color of the cluster each basin belongs to while the gray area corresponds to the 1σ variation of the output models for the corresponding locations. The basins are ordered according to their diameter size with the SPA basin first (largest basin) and the Schwarzschild basin last (smallest basin). Comparing the density profiles of each basin would allow us to identify any relationship between the diameter of the basin and the depth of the positive density anomaly in its center.

Comparing the profiles of the SPA and Imbrium basin shows that the largest basin does not necessarily has the deepest distribution of positive density anomaly. The positive density anomaly of the SPA basin stretches from layer 1 to layer 6 while the positive density anomaly of the Imbrium basin reaches down to layer 10. The algorithm does not simply match a broader gravity signal with a deeper density distribution, instead, it finds a particular density distribution for each basin which is a more complex and possibly more realistic way to represent the distribution of density per depth.

5.4.5 Deep density anomalies

The clustering of the deepest five layers was performed separately from the clustering of the shallowest layers since density features above the boundary given by the correlation length are significantly different than the features below the boundary. Figures 5.15 a-c show the mean density of the output models at layers 7, 8 and 9 with pink dots showing the location of deep moonquakes in the corresponding layers

as inferred by Nakamura *et al.* [21]. Figure 5.15d shows the location of members of the three clusters obtained by classifying density profiles from layers 6 to 10.

Most of the tesseroids at layers 7, 8 and 9 of the mean model are grayed out because they have very high standard deviations compared to their mean ($|\sigma_\rho/\mu_\rho| > 1$) however, Figure 5.16 indicates that the density anomalies in cluster 1 are negative while the ones in cluster 2 are positive and the ones in cluster 3 are close to zero. Although the standard deviation is high, the fact that the means of tesseroids in a cluster are not randomly distributed and, instead they are all negative, indicates that it is more likely that the density anomalies of those tesseroids are negative, instead of positive. We can say then, subject to the resolution of our tesseroid grid and input gravity data, that there are regions of lower than average density in the near and far side of the Moon. The exact value of the density of these regions is unknown, however, and it is necessary to evaluate further if the magnitude of these anomalies is not a product of the linear optimization of density, as they were in chapter 4.

As described in section 5.2.1, the main features in the deep interior of the Moon are the proposed mid-mantle discontinuity, the partial-melt layer and the asymmetrical distribution of moonquakes, which could be caused by a difference in properties between the deep far side and the deep near side of the Moon. If the mid-mantle discontinuity and the partial-melt layer are in fact global and spherically symmetric features of the interior of the Moon, then their location cannot be evaluated using gravity data. The asymmetrical distribution of the deep moonquakes, however, can be compared to the distribution of density found by THeBOOGIE at similar depths.

As can be seen in Figure 5.16, approximately half of the near side deep moonquakes coincide with the location of the low density region in the near side of cluster 1 while the other half coincides with areas of clusters 2 and 3. There is not a clear relationship between the location of a low or high density anomaly and the location of near side deep moonquakes. There are only three moonquake clusters of the far side and they do not coincide with the location of a specific density anomaly cluster either.

The positive deep density anomalies found at layers 7-9 (507 to 1141 km depth) could be caused by an inefficient overturn of the Fe-Ti cumulates and the negative anomalies might reflect primordial water reservoirs in the lunar mantle. It is necessary, however, to analyze if the water content of these reservoirs is enough to produce a detectable change in density in the material.

5.5 Discussion

The thickness of the density anomalies found by THEBOOGIE is larger than the ones expected by crustal thickness variations. The combined effect of the parsimony of the algorithm and the fact that density models are less likely to have very shallow nuclei, contributes to creating large Voronoi region and, as consequence, large and thick density anomalies. The prior distribution of the location of Voronoi nuclei is uniform in the volume between the core-mantle boundary and the surface of the Moon (table 5.1). However, the location vector v_{loc} has three components in Cartesian coordinates (x, y and z) that are sampled uniformly from the core-mantle

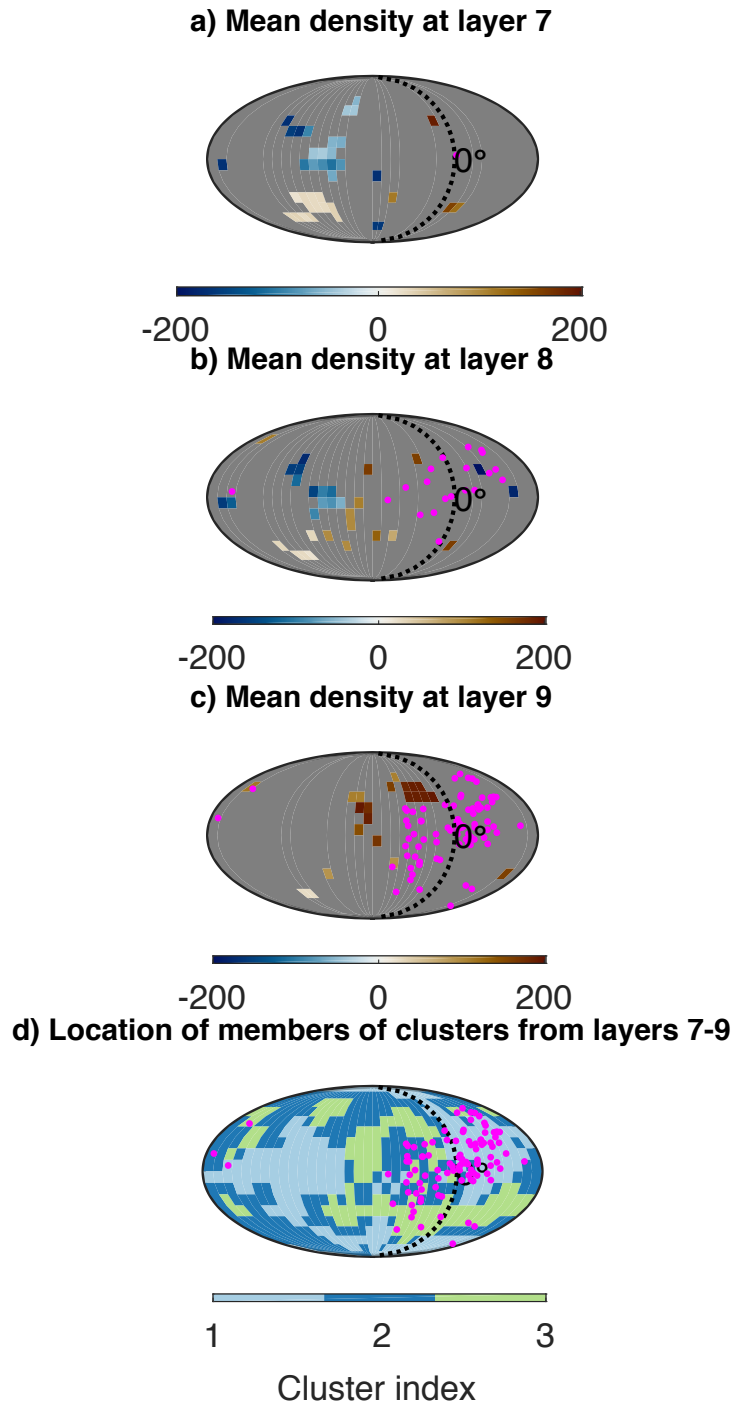


Figure 5.15: Mean density of layers 7-9 with grayed out tesseroids having very large standard deviation (a-c) with pink dots showing the location of deep moonquakes [21]. d) Map of the location of clusters obtained using tesseroids at layers 6-10 of the mean model.

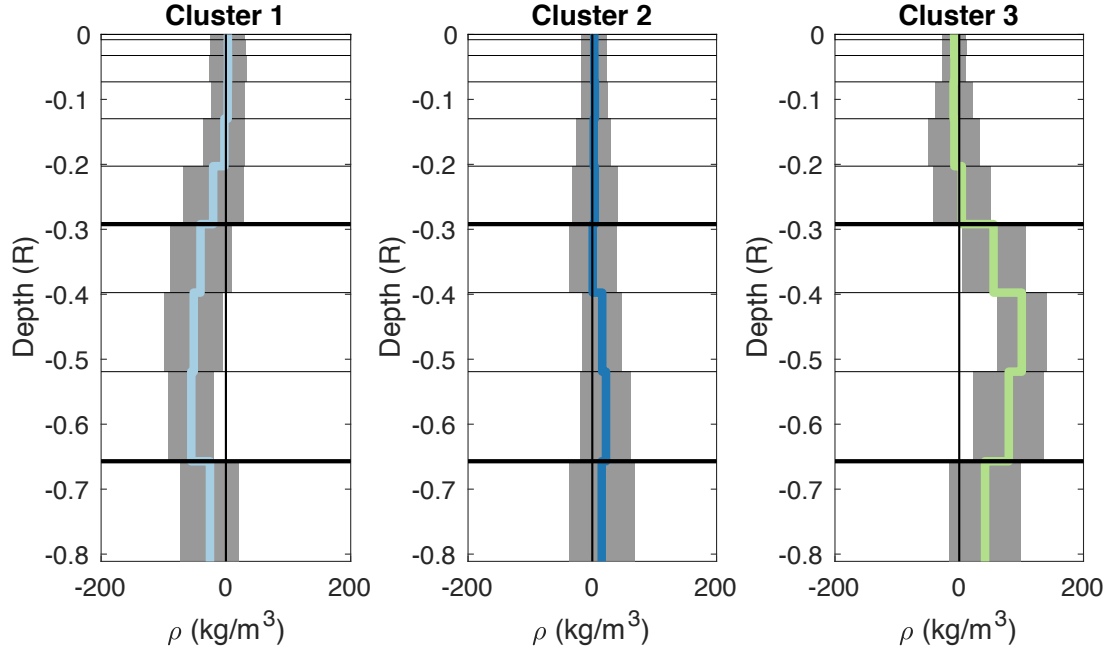


Figure 5.16: Density per depth of clusters 1-3. Thick black lines show the location of layers 7, 8 and 9 used in the clustering of deep density anomalies.

boundary to the surface. This means that there are fewer combinations of the values of these coordinates that result in nuclei at locations $r > 0.9R$ compared to the number of combinations resulting in $r < 0.9R$ where R is the radius of the Moon. It is then more likely to have Voronoi nuclei in layers 2-10 than in layer 1.

Increasing the number of allowed Voronoi regions and using a higher resolution tesseroïd grid would result in small Voronoi regions but running an inversion with a higher resolution grid would require a higher memory and computation time since it is necessary to save the location of each Voronoi region and the density value of each tesseroïd, for each density model.

The density profiles of 28 lunar basins of varying diameter were plotted and a relationship between the size of the diameter and the depth of these basins was not

found. Largest basins do not necessarily have the thickest distribution of positive density anomaly which would generate a broader gravity feature and match the input gravity data. There is no clear relationship between the size of the basins and how the density in its center is distributed with depth.

The boundary given by the correlation length divides the volume of the sphere into two parts, shallow and deep. Clustering of the shallow density anomalies shows great agreement with the location of surface features of the Moon and allow us to analyze how the density changes per depth in each feature individually. As expected, clustering of deep density anomalies do not show an agreement with surface features, instead, the clustering shows large scale positive and negative density anomalies that are not correlated to surface features.

The Apollo seismic stations have detected very few deep moonquakes in the far side and there is still a region of the far side within 40° of Earth's antipode where no deep moonquakes have been detected. This has led to two ideas: moonquakes occur in the same frequency in the far side and near side but the ones in the far side are not detected by the Apollo seismic stations or moonquakes occur in the near side only because of the particular conditions of that region [21].

We find positive and negative density anomalies in the depth range of 507 to 1141 km but the density structure at those depths is not clearly different between the near and far side. Our results do not support the idea that the material in the far side of the Moon, specifically the density of this material, is different from the one in the near side. The location of moonquakes do not coincide exclusively with a positive or negative density anomaly, therefore, it not possible to link their

occurrence to a mechanism producing a negative or positive density anomaly. Our work suggests that deep moonquakes may occur in the far side too and seismic waves were attenuated before reaching the Apollo seismic stations in the near side.

The existence of positive and negative density anomalies in the depth range of 507 to 1141 km is consistent with previous studies proposing a heterogeneous lunar mantle [103, for example]. The positive density anomalies might be related to inefficient overturn of ilmenite cumulates while the negative anomalies to water reservoirs. The estimates of the bulk water content in the Moon is low (300 ppm) [104], however, that is a lower limit for the content of water in these reservoirs. There is no additional constraint on the lateral location of these reservoirs and the depth of the low density anomalies confidently resolved in this work are slightly shallower than the proposed water reservoirs (507-900 km compared to 1000-1300 km) as shown in Figure 5.15. The mean of cluster 1 in Figure 5.16 shows that there might be a negative anomaly from 1141 to the CMB although with increased uncertainty.

Further constraints on the location of the water reservoirs is needed together with an analysis of the water content needed to produce a negative density anomaly and the dynamics that allowed a low density region to maintain a stable location within the lunar mantle.

5.6 Conclusions

We present a group of density models that fit the Bouguer gravity acceleration of the Moon obtained using non-informative priors in a flexible gravity inversion method, THeBOOGIe. This group of density models is represented by a mean model and two measures of confidence on the mean value at each tesseroïd in the grid. The density anomalies in these models are not restricted to be located in the crust-mantle interface or above it in order to not bias the inversion result. The lateral distribution of density anomalies fit the lateral variations of crustal thickness which is a very positive result. The thickness of the anomalies is overestimated and is close to six times larger than the thickness inferred by other methods. This trade-off is expected because of the non-uniqueness of gravity inversions. The confidence measures on the density values obtained, provide information about how well-constrained each value is in light of the input gravity acceleration used and is an essential information since gravity inversions are non-unique. In general, the uncertainty on the density models inferred increases with increasing depth.

The correlation and cluster analysis done on the group of density models obtained provides a wealth of knowledge about the relationship between tesseroïds. It provides a way to identify density features other than visually inspecting maps of each layer of the mean model. The correlation length shows that there is a boundary between shallow and deep density anomalies. The clustering of shallow anomalies shows density features corresponding to surface features while the clustering of deep anomalies shows positive and negative density anomalies that are not correlated

with surface features. The density distribution on the far side is not significantly different from the distribution on the near side, supporting the idea that far side deep moonquakes might occur in the far side too and seismic waves were attenuated before reaching the Apollo seismic stations. The deep density anomalies might be related to a inefficient overturn of ilmenite cumulates or water reservoirs in the deep mantle.

Chapter 6: Summary and future work

6.1 Summary

A novel method to invert gravity acceleration data was developed with the aim of constraining the interior distribution of density within a planetary body. THEBOOGIE does not require informative priors for the location of density anomalies or any other parameter of interest. However, an informative prior can be provided if justified. This inversion method outputs a group of density models representative of a posterior probability distribution. From this group of models, the variation of parameter values that fit the data can be obtained and other measures of uncertainty can be calculated. Regions within a planetary body having density values with large uncertainties are not well constrained by the data while regions with a small uncertainty are. Using non-informative priors for the location, the density anomalies are not required to be located at the crust-mantle interface and deeper anomalies are not necessarily mapped to these depths.

The chosen parametrization of density anomalies is an important factor affecting the performance of THEBOOGIE. Point masses represent the simplest parametrization since they are defined as points in space with an associated mass and no shape. The calculation of the gravity field of density models using a point mass parametriza-

tion is very fast. When the input gravity data is produced by a group of point masses, the inversion algorithm outputs density models having point masses with locations and magnitudes matching the ones producing the data. When the input gravity data is produced by spherical caps, the algorithm finds the correct location of their center but cannot constrain their shape or density. For both cases, the inversion method find density models that fit the input gravity data very well.

Spherical caps have similar shapes as the density anomalies produced by impact craters where crust is removed by the impactor and the crust-mantle boundary might be shallower. The inversion of synthetic data showed that THEBOOGIE is able to find density models that fit the input gravity data very well and that most of the output density models match the one producing the input gravity data. The mean of the output models match the location of the latitude, longitude and aperture of the caps in the target model and their 1σ deviations is very small. The uncertainty is larger for the thickness, depth and density values, as expected. Using a spherical cap parametrization, however, increases the computing time of the gravity acceleration and the number of iterations needed for convergence compared to using point masses due to the increase of parameters to constrain.

A Voronoi region (VR) contains the volume close to a nucleus i than to other nuclei in a sphere. VRs can parametrize density anomalies of any shape with the right location and number of nuclei and the calculation of the gravity field of models using this parameterization is not as slow as with spherical caps. An inversion of synthetic gravity data resembling the Bouguer gravity field of the Moon shows that THEBOOGIE can find density models that fit the input data. These density models

match certain parameters of the density model producing the input data while having some differences in other parameters. The lateral distribution of density is retrieved correctly, with the lunar crustal dichotomy and impact basins in the right latitudes and longitudes. The thickness of shallow features is overestimated while the density anomalies related to them is underestimated. This is an expected tradeoff in gravity inversions where the same signal can be produced by a thin dense feature and by a thick, less dense one.

The shape of a mid-mantle anomaly is retrieved correctly by THeBOOGIe using a VR parametrization. Density anomalies at this depth in the Moon had not been previously reported in the literature but it is useful to assess if the algorithm would be able to detect it in case they do exist and the algorithm does. The 1σ variations and another measure of uncertainty called the Kullback-Liebler divergence show that this anomaly is significant and is not part of the noise of the density distribution. The recovery of such a deep anomaly is very promising since it shows that a mantle anomaly could be recovered with gravity data.

The Bouguer gravity field of the Moon was inverted using a VR parametrization. Density anomalies from the surface to a depth of 350 km are linked to surface features. THeBOOGIe clearly identifies density anomalies related to the South-Pole Aitken basin, the crustal dichotomy and near side impact basins. The thickness of these shallow anomalies is much larger than the one inferred by other methods while their magnitude is smaller. This is due to the non-uniqueness of gravity inversions. Anomalies deeper than 350 km are not related to surface features. The algorithm finds two regions with a negative density anomaly in the depth range 507-1141 km.

Some near side deep moonquakes coincide with the location of one of the low density regions and some of them not. A clear relationship between the location of near side deep moonquakes and density anomalies is not found. The deep positive density anomalies might be related to an inefficient overturn of ilmenite cumulates while the deep negative anomalies might be related to water reservoirs in the deep mantle.

6.2 Future work

The thickness of shallow lunar density anomalies are currently overestimated by THeBOOGIe, compared to estimations of crustal thickness. Although a trade-off between the thickness and magnitude of anomalies is expected in gravity inversions, it is important to explore if the trade-off can be reduced with updates to the inversion algorithm. If the prior distribution of the depth of nuclei is uniform, then very shallow Voronoi regions would be just as likely as deeper ones. Currently, the prior distribution of the nuclei location is uniform in the volume of the sphere which do not necessarily mean they are uniform in the radial direction.

Density anomalies can be as small as the size of the tesseroids in the grid. If a Voronoi region is smaller than the size of one tesseroid, then this small region would be mapped in a region the size of the tesseroid. Reducing the size of the tesseroids would allow smaller anomalies to exist. This would mean increasing the resolution of the grid and increasing the number of tesseroids. Having smaller anomalies might reduce the overestimation of the thickness of shallow anomalies but would

increase the memory requirements of the inversion since the density value of each tesseroïd, at each iteration, is saved. The computation time of each iteration would also increase but not necessarily in a significant way. In the mapping of density anomalies from Voronoi regions to the tesseroïd grid, it is necessary to do a nearest neighbor analysis and locate the tesseroïd that is closer to a nuclei. If the number of tesseroïds increases, then the calculations of the distances between nuclei and tesseroïds needed would increase too but this process currently occupies less than 5% of the computation time of each iteration.

Running more iterations of THEBOOGIE algorithm would provide a larger sampling of the posterior which might result in a more clear image of the interior. The number of additional iterations to run, however, is not clear since there is no way to predict the number of iterations needed for an efficient sampling. Even if more iterations are ran, the algorithm might get stuck in a local minimum and sample only a small region of the posterior.

Gravity data is not sensitive to different layered models of the interior. Concentric layers of constant density produce the same gravity field as a sphere of uniform density, as long as the total mass is the same in both cases. Therefore, it is not possible to combine a radial density distribution of the Moon with the 3-D density anomalies inferred in this work just using gravity data as constraint. It would very interesting to estimate, instead, the size and magnitude of 3-D low-density anomalies that might exist in the depth range 500-1141 km while fitting laser ranging data of the Moon. It is also necessary to calculate the flow stress produced by the lateral variations of density caused by these anomaly regions. If the size and magnitude

of these regions produce realistic tidal Love numbers, moment of inertia and stress, then the confidence on the existence of these anomalies would increase.

Finally, the deployment of seismometers in the lunar far side would bring a wealth of knowledge about the deep interior of the Moon. Far side seismic stations could detect far side deep moonquakes and clarify if they occur as frequently as they do in the near side or not. Far side seismic stations could also map the similarities and differences of the deep near and far seismic velocity structures which can be related to density.

Appendix A: A Bayesian approach to infer interior mass anomalies from the gravity data of celestial bodies

A.1 Proposal distributions

The general proposal distribution used to generate a new member of the Markov chain Monte Carlo is $q(\{p'_m\}|\{p_m\}) = q(n', \{m'\}, \{x'\}, \{y'\}, \{z'\}, \sigma_g^{2'}|\{n\}, \{m\}, \{x\}, \{y\}, \{z\})$. As can be seen in Figure 2.1, the model $\{p'_m\}$ is chosen by making one of four possible changes in model $\{p_m\}$. Therefore, depending on the change chosen, the proposal distribution simplifies in one of several ways.

1. Add a new anomaly. The location of the new anomaly is chosen from the prior distribution.
2. Change the coordinates of an existing anomaly. This proposal distribution is the same for x , y and z . The magnitude of the standard deviation represents how far or close can be the new location of the anomaly and s is the number of data points in the input gravity data. In the inversions shown in this paper, $\sigma_x = \sigma_y = \sigma_z = 5$ km.

$$q(x'|x) = \frac{1}{\sqrt{(2\pi^n(\sigma_g^2)^s)}} \exp\left(-\frac{(x' - x)^2}{2\sigma_x^2}\right) \quad (\text{A.1})$$

3. Delete an existing point mass: uniform probability of choosing any of the existing ones.
4. Change the variance of noise on input data. The standard deviation of this distribution is $\sigma_{\sigma_g^2}$. For the inversions shown in this paper, $\sigma_{\sigma_g^2} = 4.9 \times 10^{-12} \text{ (m/s}^2\text{)}$.

$$q(\sigma_g^{2'}|\sigma_g^2) = \frac{1}{\sqrt{(2\pi^n(\sigma_g^2)^s)}} \exp\left(-\frac{(\sigma_g^{2'} - \sigma_g^2)^2}{2\sigma_{\sigma_g^2}^2}\right) \quad (\text{A.2})$$

A.2 Location of anomalies of target model III

The location and magnitude of the anomalies were chosen randomly.

Anomaly	Latitude	Longitude	Radius	Mass (kg)
1	-42.1	-25.9	0.9	7.4879×10^{17}
2	75.3	-58.5	0.49	0.4125×10^{17}
3	-7	11.6	0.94	0.6318×10^{17}
4	66.7	59.1	0.87	0.2002×10^{17}
5	54.9	76.5	0.56	0.3022×10^{17}
6	53.7	52.5	0.62	0.6162×10^{17}
7	-44.1	38.4	0.84	1.9651×10^{17}
8	-21.4	73.5	0.74	0.1294×10^{17}
9	-48.5	-64.8	0.73	4.5031×10^{17}
10	-67.7	41.8	0.82	0.2986×10^{17}
11	60.6	157.5	0.91	3.1491×10^{17}
12	-46.2	123.2	0.85	4.4993×10^{17}
13	22.4	-2.5	0.58	0.2314×10^{17}
14	12.2	170.2	0.87	3.582×10^{17}
15	4.1	-64	0.8	3.0992×10^{17}
16	7.1	-171	0.7	1.9576×10^{17}
17	34.2	26.9	0.89	0.1286×10^{17}
18	-18.4	-92.2	0.9	7.8446×10^{17}
19	-8.4	-20.1	0.8	0.397×10^{17}
20	-39.5	-146.9	0.76	8.8032×10^{17}
21	8.8	-26	0.32	0.1749×10^{17}
22	-40.9	173.5	0.75	0.9531×10^{17}
23	38.8	-14.5	0.65	0.4445×10^{17}
24	-35.8	-169.8	0.99	5.0659×10^{17}
25	48.1	117.6	0.76	0.4204×10^{17}

Table A.1: Location of anomalies 1-25 of the target model III

Anomaly	Latitude	Longitude	Radius	Mass (kg)
26	12	-37	0.71	2.0249×10^{17}
27	-16.7	-0.5	0.63	4.1305×10^{17}
28	16.5	128	0.59	8.5556×10^{17}
29	-61.2	50.9	0.59	3.3633×10^{17}
30	-46.9	-131.1	0.79	0.1691×10^{17}
31	-70.3	177.2	0.71	1.3994×10^{17}
32	29.8	-179.1	0.91	0.4983×10^{17}
33	-11.1	53.5	0.77	0.8389×10^{17}
34	-39.6	35.5	0.89	8.8763×10^{17}
35	36.9	-34.5	0.44	0.1471×10^{17}
36	11.7	91.4	0.65	0.3964×10^{17}
37	16.7	-93.4	0.49	0.7331×10^{17}
38	-9.1	-116.2	0.67	0.2973×10^{17}
39	4.9	-30.6	0.73	0.9013×10^{17}
40	-39.3	-119.2	0.8	3.9532×10^{17}
41	38.7	-100.3	0.92	1.3488×10^{17}
42	-38.8	97.3	0.87	1.0252×10^{17}
43	-31.1	-19.7	0.93	2.4992×10^{17}
44	-37.4	57.8	0.75	1.1489×10^{17}
45	-52.9	-24.8	0.68	0.3238×10^{17}
46	17.9	179.7	0.79	0.2273×10^{17}
47	-10.9	-115	0.86	1.33×10^{17}
48	24.3	93	0.29	0.6577×10^{17}
49	55.5	128.7	0.23	0.7973×10^{17}
50	-26.1	105.1	0.65	2.4374×10^{17}

Table A.2: Location of anomalies 26-50 of the target model III

Appendix B: Bayesian gravity inversion algorithm for inferring finite size density anomalies in planetary interiors

B.1 Mean density anomaly of the output models at all layers

Figure B.1 shows the mean density anomaly of the output models. There is an increase in density anomaly near point a) where the Imbrium basin is, next to Serenitatis. The dichotomy between the near and far side is also visible by a density difference between negative values of the far side and positive values of the near side. The boundary of this far side anomaly has the right location. The SPA basin has also the right center location and size. There is increase in density near point d) in layer 7 and 8. This corresponds to the right lateral location of the deep feature in the target density model but in the target model, it only exists in layer 7. The magnitude of the anomalies in layers 8-10 is very large compared to the ones in shallower layers. These anomalies do not correspond to any density anomaly in the target model and are, most likely, a result of optimization of density performed in THEBOOGIE at each iteration. If the gravity acceleration of the model is not sensitive to the density anomaly at these depths, an optimization of the density values at these depths results in very large values. Layers 8-10 also show a reversal

of the magnitude of density anomalies between the far and near side. The far side has a positive anomaly while the near side a negative one. This can be explained by the fact that the anomalies related to the mascons, SPA and dichotomy are much thicker than in the target model, creating an excess or deficit of mass that is compensated by the anomalies in layers 8-10. The mascons, SPA and dichotomy features in the mean model are thicker than in the target model because the location of the nuclei is chosen with uniform probability inside the sphere and it is less likely to have nuclei so close to the surface.

B.2 Kullback-Liebler divergence of the output models at all layers

Figure B.2 shows the normalized Kullback-Liebler divergence $D_{KL}/\max(D_{KL})$ of the output models per layer. $D_{KL}/\max(D_{KL})$ decreases with depth. The locations with values $D_{KL}/\max(D_{KL}) > 0.5$ are significantly different from the prior distribution of density values (uniform distribution with limits -500 kg/m^3 to 500 kg/m^3) which means that density values in these locations depend on the input data and are constrained by it. Most tesseroids in the first six layers are well constrained by the input data. Tesseroids near location d) in layer 7 are well constrained too while most of the rest of the tesseroids in that layer are not. In layers 8-10, most tesseroids are below the limit $D_{KL}/\max(D_{KL}) < 0.5$ which means they are not significantly different from the prior distribution. There is only a small region that is above the limit $D_{KL}/\max(D_{KL}) > 0.5$ near point d) in layer 8. The area near point d) is the location of the deep feature of the target density model.

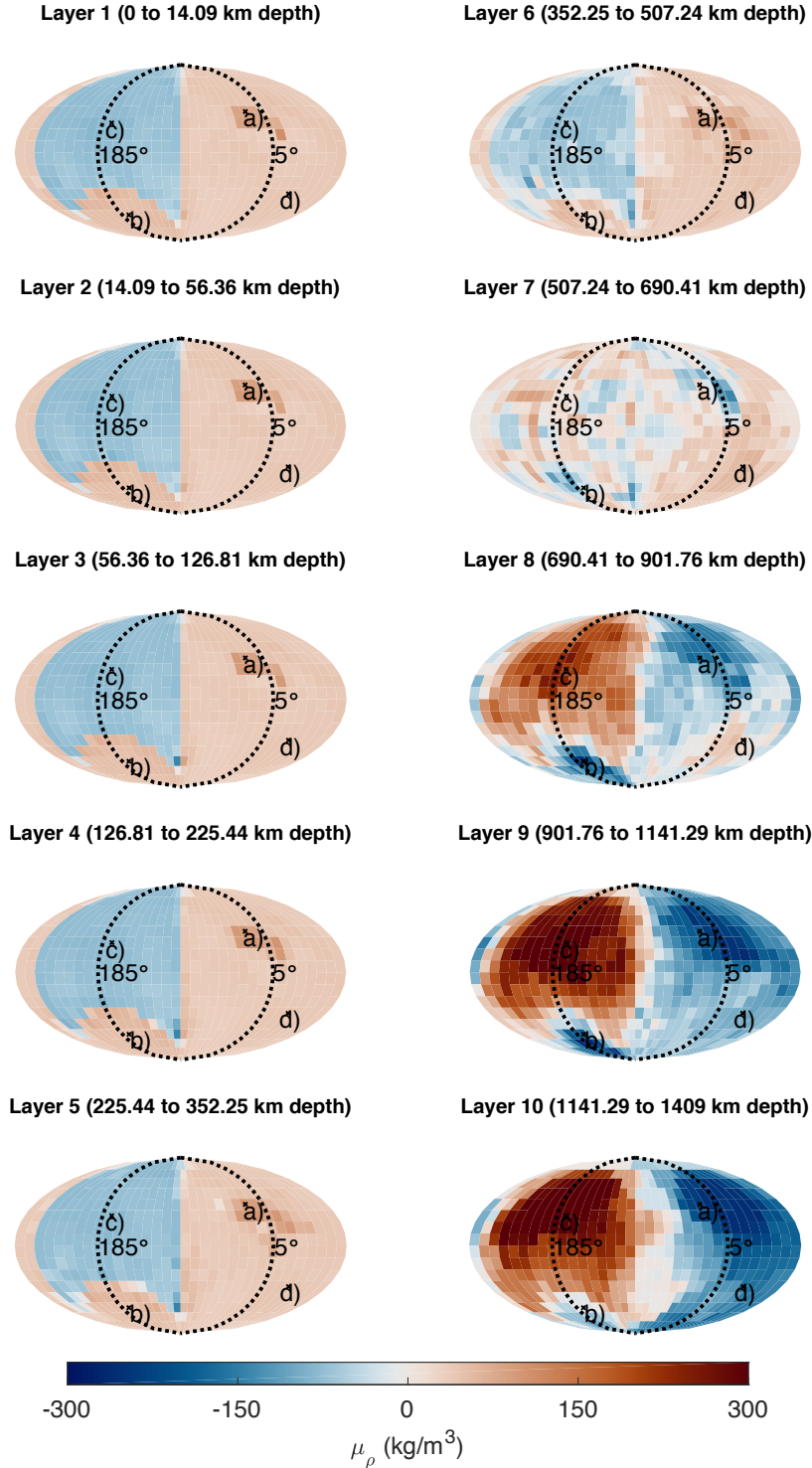


Figure B.1: Maps of mean density anomalies of the output models at all layers. The first six layer have a similar lateral distribution of density with features resembling the mascons, SPA and far side crust of the target density model. There is an increase in density anomaly near point d) in layers 7 and 8. The deep anomaly near d) in the target model is located in layer 7 only. There is a sudden increase and reversal of the density anomalies in layers 8-10 compared to the shallower layers.

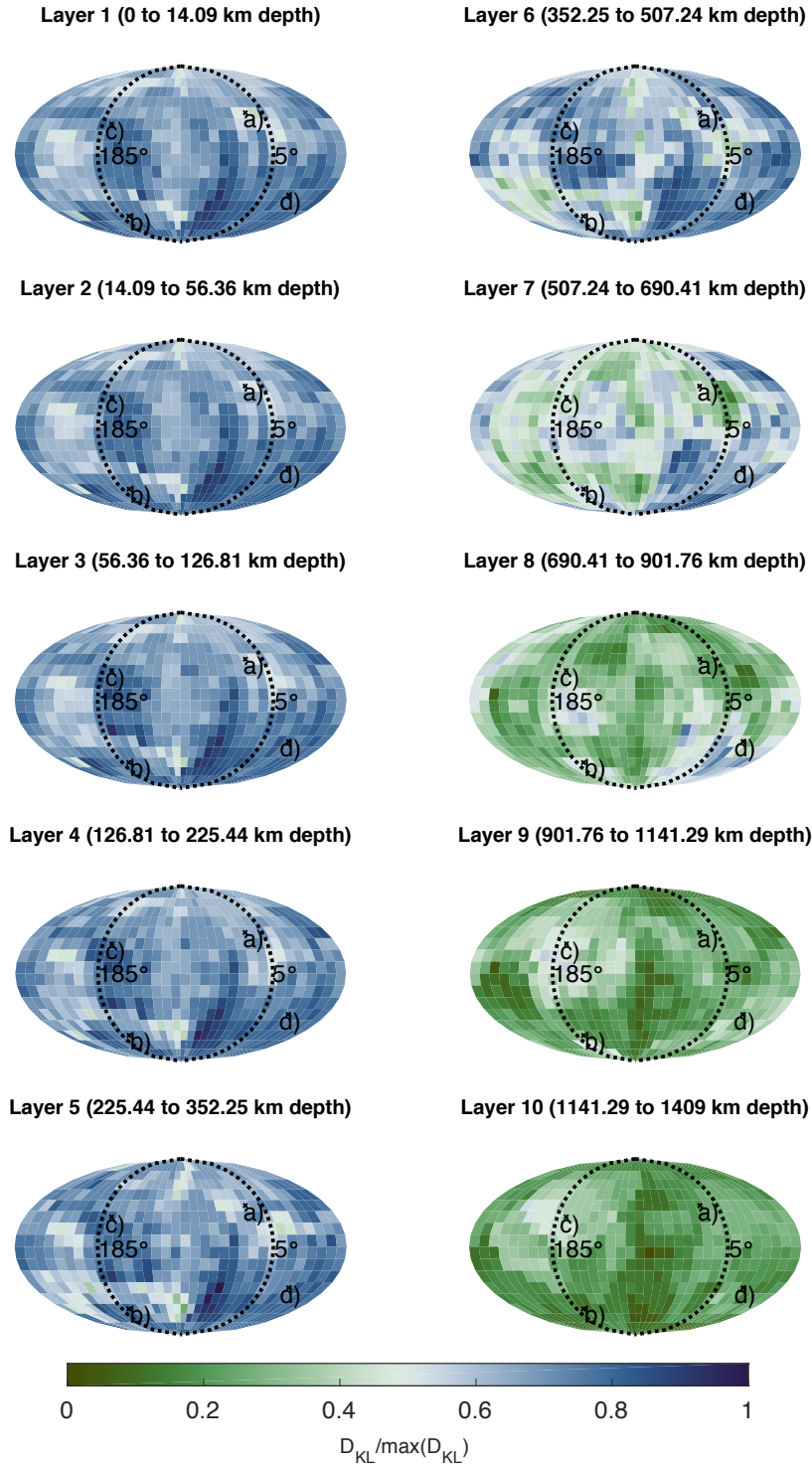


Figure B.2: Maps of normalized Kullback-Liebler divergence ($D_{KL}/\max(D_{KL})$) of output models at all layers. Most tesseroids in layers 1-6 are well constrained by the input gravity data because they have a value of $D_{KL}/\max(D_{KL}) > 0.5$. The region near point d) in layer 7 and 8 is well constrained too while most of the tesseroids in layers 8-10 are not.

B.3 Standard deviation of the output models at all layers

Figure B.3 shows the standard deviation of the output models per layer. The standard deviation increases with depth showing that very different values can fit the input gravity data at deep locations compared to shallow locations. Layers 1-6 have a low standard deviation with the highest values being located near the boundaries of the far and near side crust, SPA basin and mascons. Layers 7 and 8 show interesting values near point d). In layer 7, there is a region of uniform standard deviation near this point but the values are slightly higher than the surrounding area. In layer 8, there is a region with a lower standard deviation than the surrounding area near this point also. Just by using the standard deviation is difficult to assess what this means. The criterion used to assess significance using the standard deviation values also depends on the mean density of the tesseroids. $\sigma_\rho/\mu_\rho < 1$. Using the quantity σ_ρ/μ_ρ allows to see the 1σ range of tesseroids that fit the input data.

B.4 Standard deviation of the output models divided the mean density anomaly at all layers

Figure B.4 shows the standard deviations values of the output models divided by their mean density anomalies. Tesseroids with $\sigma_\rho/\mu_\rho > 1$ are well constrained by the input data while tesseroids with $\sigma_\rho/\mu_\rho < 1$ are not. Regions near the boundary of the far and near side crust, SPA basin and mascons in layers 1-6 are not well constrained while the rest of the tesseroids in these layers are. The area near point

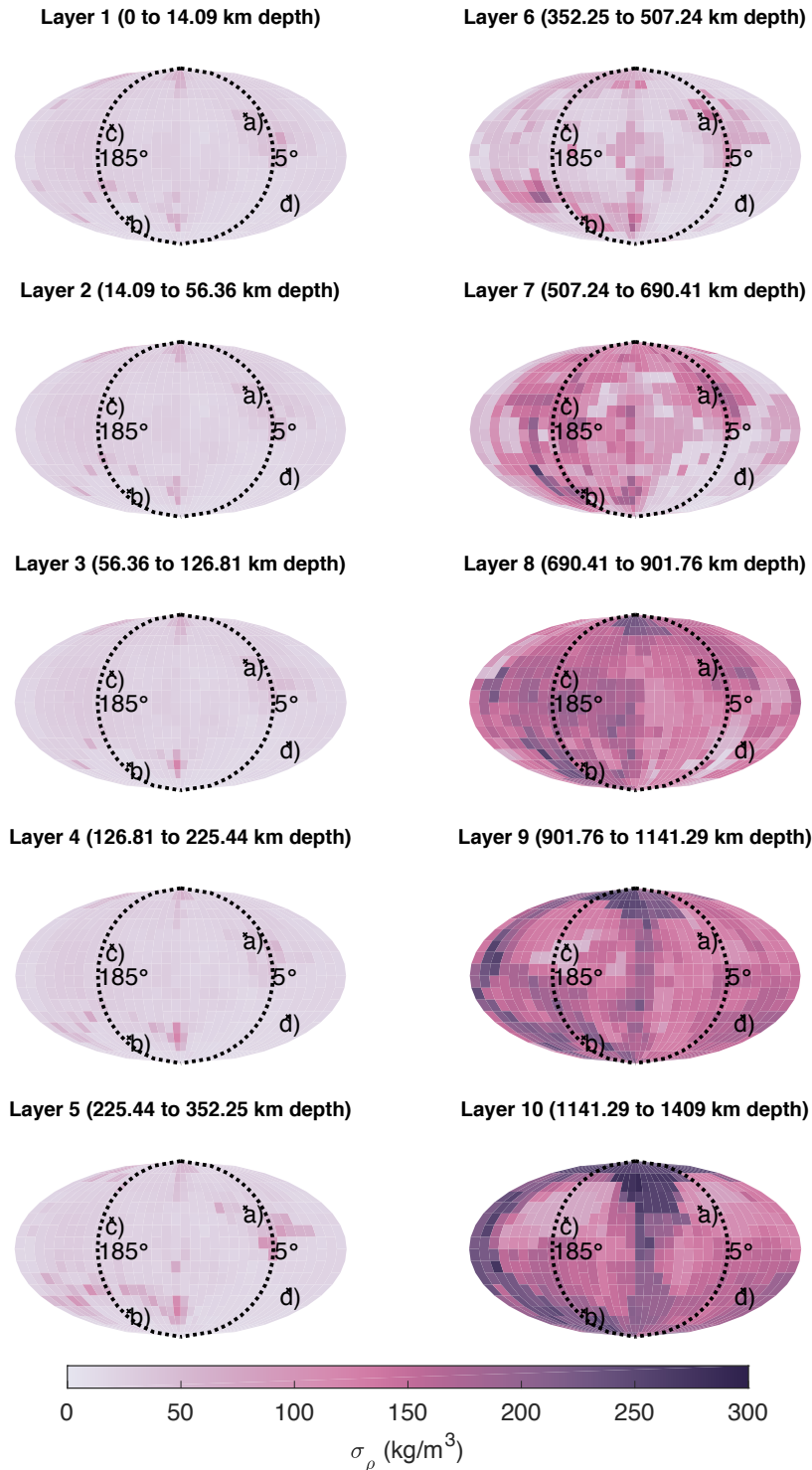


Figure B.3: Maps of standard deviation (σ_ρ) for all layers. The standard deviation increases with depth at most locations. The standard deviation is slightly higher near the boundaries of the far side and near side crust, SPA basin and mascons in layers 1-6. There is a region of uniform standard deviation near point d) in layer 7 and a region of low standard deviation near point d) in layer 8.

d) in layer 7 is well constrained too while the corresponding location in layer 8 is not.

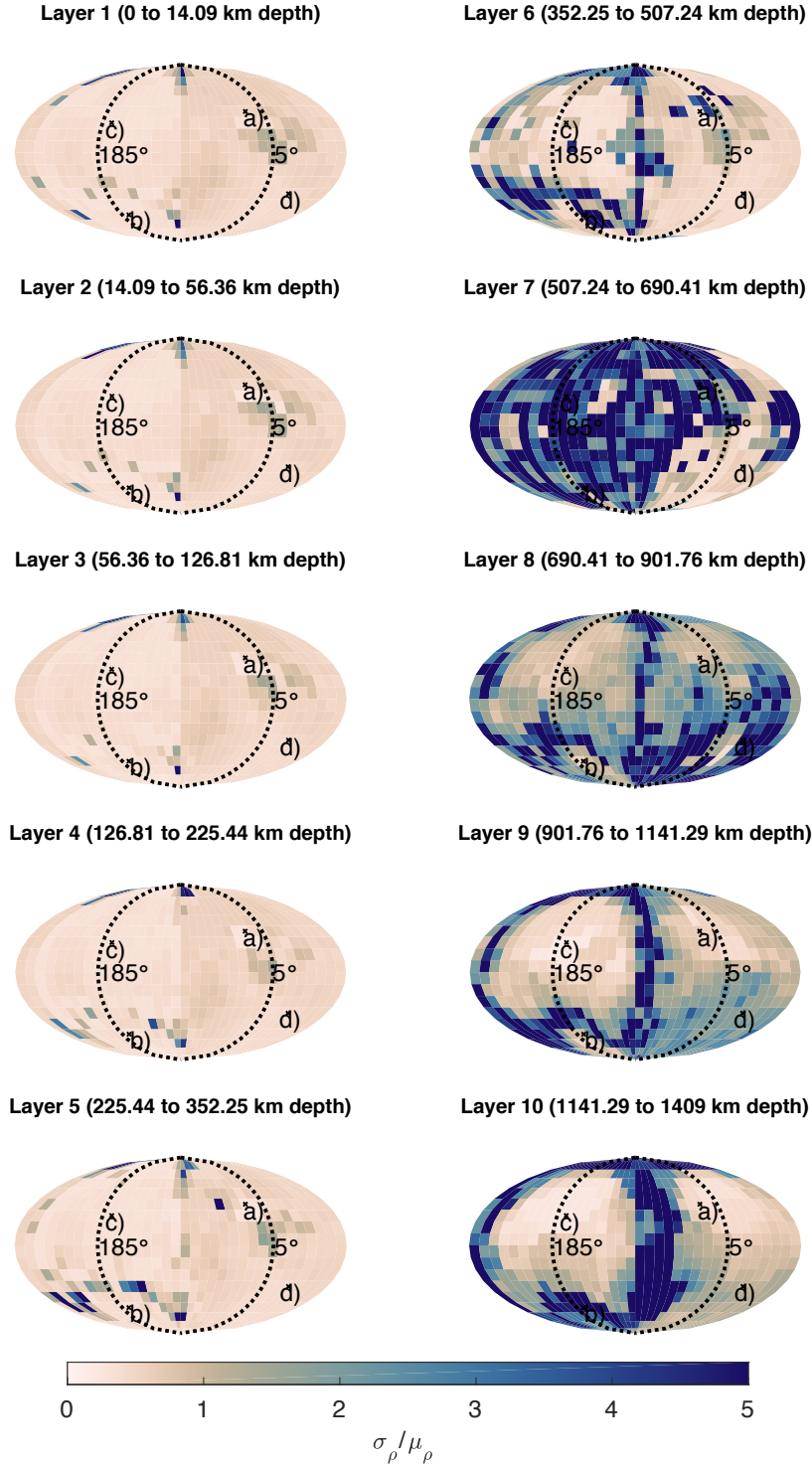


Figure B.4: Maps of standard deviation divided by the mean density anomaly of the tesseroids at each layer. Tesseroids with values smaller than 1 have density anomalies well constrained by the input gravity data. Regions near the boundary of the far and near side crust, SPA basin and mascons in layers 1-6 are not well constrained while the rest of the tesseroids in these layers are. The area near point d) in layer 7 is well constrained too.

Bibliography

- [1] A. Khan, J. A. D. Connolly, A. Pommier, and J. Noir. Geophysical evidence for melt in the deep lunar interior and implications for lunar evolution. *Journal of Geophysical Research: Planets*, 119(10):2197–2221, 2014. [10.1002/2014JE004661](https://doi.org/10.1002/2014JE004661).
- [2] Claus Muller. *Spherical Harmonics*, volume 17. Springer, 1966. <https://doi.org/10.1007/BFb0094775>.
- [3] David E. Smith, Maria T. Zuber, Gregory A. Neumann, Frank G. Lemoine, Erwan Mazarico, Mark H. Torrence, Jan F. McGarry, David D. Rowlands, James W. Head III, Thomas H. Duxbury, Oded Aharonson, Paul G. Lucey, Mark S. Robinson, Olivier S. Barnouin, John F. Cavanaugh, Xiaoli Sun, Peter Liiva, Dan-dan Mao, James C. Smith, and Arlin E. Bartels. Initial observations from the Lunar Orbiter Laser Altimeter (LOLA). *Geophysical Research Letters*, 37(18), 2010. [10.1029/2010GL043751](https://doi.org/10.1029/2010GL043751).
- [4] Gordon Chin, Scott Brylow, Marc Foote, James Garvin, Justin Kasper, John Keller, Maxim Litvak, Igor Mitrofanov, David Paige, Keith Raney, Mark Robinson, Anton Sanin, David Smith, Harlan Spence, Paul Spudis, S Alan Stern, and Maria Zuber. Lunar Reconnaissance Orbiter Overview: The Instrument Suite and Mission. *Space Science Reviews*, 129:391419, 2007. <https://doi.org/10.1007/s11214-007-9153-y>.
- [5] M.K. Barker, E. Mazarico, G.A. Neumann, M.T. Zuber, J. Haruyama, and D.E. Smith. A new lunar digital elevation model from the Lunar Orbiter Laser Altimeter and SELENE Terrain Camera. *Icarus*, 273:346 – 355, 2016. <https://doi.org/10.1016/j.icarus.2015.07.039>.
- [6] M.T. Zuber, D.E. Smith, D.H. Lehman, and et al. Gravity Recovery and Interior Laboratory (GRAIL): Mapping the Lunar Interior from Crust to Core. *Space Sci Rev*, 178:324, 2013. <https://doi.org/10.1007/s11214-012-9952-7>.

- [7] S. Goossens, T. J. Sabaka, M. A. Wieczorek, G. A. Neumann, E. Mazarico, F. G. Lemoine, J. B. Nicholas, D. E. Smith, and M. T. Zuber. High-Resolution Gravity Field Models from GRAIL Data and Implications for Models of the Density Structure of the Moon’s Crust. *Journal of Geophysical Research: Planets*, 125(2):e2019JE006086, 2020. 10.1029/2019JE006086.
- [8] Mark A. Wieczorek, Bradley L. Jolliff, Amir Khan, Matthew E. Pritchard, Benjamin P. Weiss, James G. Williams, Lon L. Hood, Kevin Righter, Clive R. Neal, Charles K. Shearer, I. Stewart McCallum, Stephanie Tompkins, B. Ray Hawke, Chris Peterson, Jeffrey J. Gillis, and Ben Bussey. The Constitution and Structure of the Lunar Interior. *Reviews in Mineralogy and Geochemistry*, 60(1):221–364, 01 2006. 10.2138/rmg.2006.60.3.
- [9] M. Wieczorek. Gravity and Topography of the Terrestrial Planets. In Gerald Schubert, editor, *Treatise on Geophysics (Second Edition)*, pages 153 – 193. Elsevier, Oxford, second edition edition, 2015. <https://doi.org/10.1016/B978-0-444-53802-4.00169-X>.
- [10] Mark A. Wieczorek, Gregory A. Neumann, Francis Nimmo, Walter S. Kiefer, G. Jeffrey Taylor, H. Jay Melosh, Roger J. Phillips, Sean C. Solomon, Jeffrey C. Andrews-Hanna, Sami W. Asmar, Alexander S. Konopliv, Frank G. Lemoine, David E. Smith, Michael M. Watkins, James G. Williams, and Maria T. Zuber. The Crust of the Moon as Seen by GRAIL . *Science*, 339(6120):671–675, 2013. doi:10.1126/science.1231530.
- [11] Philippe Lognonné, Jeannine Gagnepain-Beyneix, and Hugues Chenet. A new seismic model of the Moon: implications for structure, thermal evolution and formation of the Moon. *Earth and Planetary Science Letters*, 211(1):27 – 44, 2003. [https://doi.org/10.1016/S0012-821X\(03\)00172-9](https://doi.org/10.1016/S0012-821X(03)00172-9).
- [12] M. Laneuville, M. A. Wieczorek, D. Breuer, and N. Tosi. Asymmetric thermal evolution of the Moon. *Journal of Geophysical Research: Planets*, 118(7):1435–1452, 2013. 10.1002/jgre.20103.
- [13] H. J. Melosh, Andrew M. Freed, Brandon C. Johnson, David M. Blair, Jeffrey C. Andrews-Hanna, Gregory A. Neumann, Roger J. Phillips, David E. Smith, Sean C. Solomon, Mark A. Wieczorek, and Maria T. Zuber. The origin of Lunar mascon basins . *Science*, 340(6140):1552–1555, 2013. 10.1126/science.1235768.
- [14] C. Nunn, R.F. Garcia, Y Nakamura, and et al. Lunar Seismology: A Data and Instrumentation Review. *Space Science Reviews*, 216(86), 2020. <https://doi.org/10.1007/s11214-020-00709-3>.
- [15] Renee C. Weber, Pei-Ying Lin, Edward J. Garnero, Quentin Williams, and Philippe Lognonné. Seismic Detection of the Lunar Core. *Science*, 331(6015):309–312, 2011. 10.1126/science.1199375.

- [16] Raphal F. Garcia, Jeannine Gagnepain-Beyneix, Sbastien Chevrot, and Philippe Lognonn. Very preliminary reference Moon model. *Physics of the Earth and Planetary Interiors*, 188(1):96 – 113, 2011. <https://doi.org/10.1016/j.pepi.2011.06.015>.
- [17] Jeannine Gagnepain-Beyneix, Philippe Lognonn, Hugues Chenet, Denis Lombardi, and Tilman Spohn. A seismic model of the lunar mantle and constraints on temperature and mineralogy. *Physics of the Earth and Planetary Interiors*, 159(3):140 – 166, 2006. <https://doi.org/10.1016/j.pepi.2006.05.009>.
- [18] A. Khan and K. Mosegaard. An inquiry into the lunar interior: A nonlinear inversion of the Apollo lunar seismic data. *Journal of Geophysical Research: Planets*, 107(E6):3–1–3–23, 2002. 10.1029/2001JE001658.
- [19] Yosio Nakamura. Seismic velocity structure of the lunar mantle. *Journal of Geophysical Research: Solid Earth*, 88(B1):677–686, 1983. 10.1029/JB088iB01p00677.
- [20] A. Khan, J. MacLennan, S. R. Taylor, and J. A. D. Connolly. Are the Earth and the Moon compositionally alike? Inferences on lunar composition and implications for lunar origin and evolution from geophysical modeling. *Journal of Geophysical Research: Planets*, 111(E5), 2006. 10.1029/2005JE002608.
- [21] Yosio Nakamura. Farside deep moonquakes and deep interior of the Moon. *Journal of Geophysical Research: Planets*, 110(E1), 2005. 10.1029/2004JE002332.
- [22] Okabe Atsuyuki, Boots Barry, Sugihara Kokichi, Nok Chiu Sung, and Kendall D. G. *Spatial Tessellations: Concepts and Applications of Voronoi Diagrams*. John Wiley, 2000. ISBN: 978-0-471-98635-5.
- [23] Wolfgang von der Linden, Volker Dose, and Udo von Toussaint. *Bayesian Probability Theory: Applications in the Physical Sciences*. Cambridge University Press, 2014. <https://doi.org/10.1017/CBO9781139565608>.
- [24] James G. Williams, Alexander S. Konopliv, Dale H. Boggs, Ryan S. Park, Dah-Ning Yuan, Frank G. Lemoine, Sander Goossens, Erwan Mazarico, Francis Nimmo, Renee C. Weber, Sami W. Asmar, H. Jay Melosh, Gregory A. Neumann, Roger J. Phillips, David E. Smith, Sean C. Solomon, Michael M. Watkins, Mark A. Wieczorek, Jeffrey C. Andrews-Hanna, James W. Head, Walter S. Kiefer, Isamu Matsuyama, Patrick J. McGovern, G. Jeffrey Taylor, and Maria T. Zuber. Lunar interior properties from the GRAIL mission. *Journal of Geophysical Research: Planets*, 119(7):1546–1578. <https://doi.org/10.1002/2013JE004559>.
- [25] Albert Tarantola. *Inverse problem Theory and Methods for Model Parameter Estimation*. Siam, 2005. doi:10.1137/1.9780898717921.

- [26] W. K. Hastings. Monte Carlo sampling methods using Markov chains and their Applications . *Biometrika*, 57(1):97–109, 1970. doi:10.2307/2334940.
- [27] P. J. Green. Reversible jump Markov Chain Monte Carlo computation and Bayesian model determination . *Biometrika*, 4:711–732, 1995. <https://doi.org/10.1093/biomet/82.4.711>.
- [28] Xiaolin Luo. Constraining the shape of a gravity anomalous body using reversible jump Markov chain Monte Carlo . *Geophysical Journal International*, 180:1067–1079, 2010. doi:10.1111/j.1365-246X.2009.04479.x.
- [29] William J. Titus, Sarah J. Titus, and Joshua R. Davis. A Bayesian approach to modeling 2D gravity data using polygons . *Geophysics*, 82:1942–2156, 2017. doi:10.1190/geo2016-0153.1.
- [30] P. J. Green. Reversible jump Markov Chain Monte Carlo computation and Bayesian model determination . *Biometrika*, 4:711–732, 1995. <https://doi.org/10.1093/biomet/82.4.711>.
- [31] W. K. Hastings. Monte Carlo sampling methods using Markov chains and their Applications . *Biometrika*, 57(1):97–109, 1970. doi:10.2307/2334940.
- [32] Alberto Malinverno and Victoria A Briggs. Expanded uncertainty quantification in inverse problems: Hierarchical Bayes and empirical Bayes. *Geophysics*, 69(4):1005–1016, 2004. 10.1190/1.1778243.
- [33] T. Bodin, M. Sambridge, K. Gallagher, and N. Rawlinson. Trans-dimensional inversion of receiver functions and surface wave dispersion. *Journal of Geophysical Research: Solid Earth*, 117(B2):1–24, 2012. <https://doi.org/10.1029/2011JB008560>.
- [34] T. M. Olugboji, V. Lekic, and W. McDonough. A statistical assessment of seismic models of the U.S. continental crust using Bayesian inversion of ambient noise surface wave dispersion data . *Tectonics*, 36(7):1232–1253, 2017. doi:10.1002/2017TC004468.
- [35] Chao Gao and Vedran Lekić. Consequences of parametrization choices in surface wave inversion: insights from transdimensional Bayesian methods. *Geophysical Journal International*, 215(2):1037–1063, 2018. <https://doi.org/10.1093/gji/ggy310>.
- [36] H. J. Melosh, Andrew M. Freed, Brandon C. Johnson, David M. Blair, Jeffrey C. Andrews-Hanna, Gregory A. Neumann, Roger J. Phillips, David E. Smith, Sean C. Solomon, Mark A. Wieczorek, and Maria T. Zuber. The Origin of Lunar Mascon Basins. *Science*, 340(6140):1552–1555, 2013. 10.1126/science.1235768.

- [37] Frank G. Lemoine, Sander Goossens, Terence J. Sabaka, Joseph B. Nicholas, Erwan Mazarico, David D. Rowlands, Bryant D. Loomis, Douglas S. Chinn, Douglas S. Caprette, Gregory A. Neumann, David E. Smith, and Maria T. Zuber. High-degree gravity models from GRAIL primary mission data. *Journal of Geophysical Research: Planets*, 118(8):1676–1698, 2013. 10.1002/jgre.20118.
- [38] P. M. Muller and W. L. Sjogren. Mascons: Lunar Mass Concentrations. *Science*, 161(3842):680–684, 1968. doi:10.1126/science.161.3842.680.
- [39] Gregory A. Neumann, Maria T. Zuber, David E. Smith, and Frank G. Lemoine. The lunar crust: Global structure and signature of major basins. *Journal of Geophysical Research: Planets*, 101(E7):16841–16863, 1996. doi:10.1029/96JE01246.
- [40] Gregory A. Neumann, Maria T. Zuber, Mark A. Wieczorek, James W. Head, David M. H. Baker, Sean C. Solomon, David E. Smith, Frank G. Lemoine, Erwan Mazarico, Terence J. Sabaka, Sander J. Goossens, H. Jay Melosh, Roger J. Phillips, Sami W. Asmar, Alexander S. Konopliv, James G. Williams, Michael M. Sori, Jason M. Soderblom, Katarina Miljković, Jeffrey C. Andrews-Hanna, Francis Nimmo, and Walter S. Kiefer. Lunar impact basins revealed by Gravity Recovery and Interior Laboratory measurements. *Science Advances*, 1(9), 2015. 10.1126/sciadv.1500852.
- [41] Kristel Izquierdo, Vedran Leki, and Laurent G J Montsi. A Bayesian approach to infer interior mass anomalies from the gravity data of celestial bodies. *Geophysical Journal International*, 220(3):1687–1699, 12 2019. 10.1093/gji/ggz544.
- [42] Yoshiaki Ishihara, Sander Goossens, Koji Matsumoto, Hiroto Noda, Hiroshi Araki, Noriyuki Namiki, Hideo Hanada, Takahiro Iwata, Seiichi Tazawa, and Sho Sasaki. Crustal thickness of the Moon: Implications for farside basin structures. *Geophysical Research Letters*, 36(19), 2009. <https://doi.org/10.1029/2009GL039708>.
- [43] William J. Hinze, Ralph R. B. von Frese, and Afif H. Saad. *Gravity and Magnetic Exploration: Principles, Practices, and Applications*. Cambridge University Press, 2013. 10.1017/CBO9780511843129.
- [44] Frank G. Lemoine, Sander Goossens, Terence J. Sabaka, Joseph B. Nicholas, Erwan Mazarico, David D. Rowlands, Bryant D. Loomis, Douglas S. Chinn, Gregory A. Neumann, David E. Smith, and Maria T. Zuber. GRGM900C: A degree 900 lunar gravity model from GRAIL primary and extended mission data. *Geophysical Research Letters*, 41(10):3382–3389, 2014. 10.1002/2014GL060027.
- [45] Maria T. Zuber, David E. Smith, Frank G. Lemoine, and Gregory A. Neumann. The Shape and Internal Structure of the Moon from the Clementine Mission. *Science*, 266(5192):1839–1843, 1994. 10.1126/science.266.5192.1839.

- [46] H. J. Melosh, Andrew M. Freed, Brandon C. Johnson, David M. Blair, Jeffrey C. Andrews-Hanna, Gregory A. Neumann, Roger J. Phillips, David E. Smith, Sean C. Solomon, Mark A. Wieczorek, and Maria T. Zuber. The origin of Lunar mascon basins . *Science*, 340(6140):1552–1555, 2013. 10.1126/science.1235768.
- [47] Frank G. Lemoine, Sander Goossens, Terence J. Sabaka, Joseph B. Nicholas, Erwan Mazarico, David D. Rowlands, Bryant D. Loomis, Douglas S. Chinn, Gregory A. Neumann, David E. Smith, and Maria T. Zuber. GRGM900C: A degree 900 lunar gravity model from GRAIL primary and extended mission data. *Geophysical Research Letters*, 41(10):3382–3389, 2014. 10.1002/2014GL060027.
- [48] Richard J. Blakely. *Potential Theory in Gravity and Magnetic Applications*. Cambridge University Press, 1995. 10.1017/CBO9780511549816.
- [49] John David Jackson. *Classical electrodynamics*. Wiley, New York, NY, 3rd ed. edition, 1999. ISBN:9780471309321.
- [50] Allen K. McNamara. A review of large low shear velocity provinces and ultra low velocity zones. *Tectonophysics*, 760:199 – 220, 2019. <https://doi.org/10.1016/j.tecto.2018.04.015>.
- [51] Trond H. Torsvik, Rob van der Voo, Pavel V. Doubrovine, Kevin Burke, Bernhard Steinberger, Lewis D. Ashwal, Reidar G. Trønnes, Susan J. Webb, and Abigail L. Bull. Deep mantle structure as a reference frame for movements in and on the Earth. *Proceedings of the National Academy of Sciences*, 111(24):8735–8740, 2014. 10.1073/pnas.1318135111.
- [52] Adam M. Dziewonski, Vedran Lekic, and Barbara A. Romanowicz. Mantle anchor structure: An argument for bottom up tectonics. *Earth and Planetary Science Letters*, 299(1):69 – 79, 2010. <https://doi.org/10.1016/j.epsl.2010.08.013>.
- [53] Edward J. Garnero, Brian Kennett, and David E. Loper. Studies of the Earth’s Deep Interior-Eighth Symposium. *Physics of the Earth and Planetary Interiors*, 153(1):1 – 2, 2005. <https://doi.org/10.1016/j.pepi.2005.08.003>.
- [54] A. Mark Jellinek and Michael Manga. Links between long-lived hot spots, mantle plumes D” and plate tectonics. *Reviews of Geophysics*, 42(3), 2004. 10.1029/2003RG000144.
- [55] Vincent Courtillot, Anne Davaille, Jean Besse, and Joann Stock. Three distinct types of hotspots in the Earth’s mantle. *Earth and Planetary Science Letters*, 205(3):295 – 308, 2003. [https://doi.org/10.1016/S0012-821X\(02\)01048-8](https://doi.org/10.1016/S0012-821X(02)01048-8).
- [56] Louise H. Kellogg, Bradford H. Hager, and Rob D. van der Hilst. Compositional stratification in the deep mantle. *Science*, 283(5409):1881–1884, 1999. 10.1126/science.283.5409.1881.

- [57] Bernhard Steinberger, Stephanie C. Werner, and Trond H. Torsvik. Deep versus shallow origin of gravity anomalies, topography and volcanism on Earth, Venus and Mars. *Icarus*, 207(2):564 – 577, 2010. <https://doi.org/10.1016/j.icarus.2009.12.025>.
- [58] J.R. Bates, W.W. Lauderdale, and H. Kernaghan. ALSEP Termination Report. Technical report, NASA Reference Publication Series, 1979.
- [59] W. Bruce Banerdt, Suzanne E. Smrekar, Don Banfield, Domenico Giardini, Matthew Golombek, Catherine L Johnson, Philippe Lognonne, Aymeric Spiga, Tilman Spohn, Clement Perrin, Simon C. Stahler, Daniele Antonangeli, Sami Asmar, Caroline Beghein, Neil Bowles, Ebru Bozdogan, Peter Chi, Ulrich Christensen, John Clinton, Gareth S. Collins, Ingrid Daubar, Veronique Dehant, Melanie Drilleau, Matthew Fillingim, William Folkner, Raphael F. Garcia, Jim Garvin, John Grant, Matthias Grott, Jerzy Grygorczuk, Troy Hudson, Jessica C. E. Irving, Gunter Kargl, Taichi Kawamura, Sharon Kedar, Scott King, Brigitte Knapmeyer-Endrun, Martin Knapmeyer, Mark Lemmon, Ralph Lorenz, Justin N Maki, Ludovic Margerin, Scott M McLennan, Chloe Michaut, David Mimoun, Anna Mittelholz, Antoine Mocquet, Paul Morgan, Nils T. Mueller, Naomi Murdoch, Seiichi Nagihara, Claire Newman, Francis Nimmo, Mark Panning, W Thomas Pike, Ana-Catalina Plesa, Sebastien Rodriguez, Jose Antonio Rodriguez-Manfredi, Christopher T. Russell, Nicholas Schmerr, Matt Siegler, Sabine Stanley, Elanore Stutzmann, Nicholas Teanby, Jeroen Tromp, Martin van Driel, Nicholas Warner, Renee Weber, and Mark Wieczorek. Initial results from the InSight mission on Mars. *Nature Geoscience*, 2020. <https://doi.org/10.1038/s41561-020-0544-y>.
- [60] Christoph Reigber. Gravity field recovery from satellite tracking data. In Fernando Sansò and Reiner Rummel, editors, *Theory of Satellite Geodesy and Gravity Field Determination*, pages 197–234, Berlin, Heidelberg, 1989. Springer Berlin Heidelberg. ISBN:978-3-540-48223-9.
- [61] Qian Huang and Mark A. Wieczorek. Density and porosity of the lunar crust from gravity and topography. *Journal of Geophysical Research: Planets*, 117(E5), 2012. 10.1029/2012JE004062.
- [62] Peter B. James, David E. Smith, Paul K. Byrne, Jordan D. Kendall, H. Jay Melosh, and Maria T. Zuber. Deep Structure of the Lunar South Pole-Aitken Basin. *Geophysical Research Letters*, 46(10):5100–5106, 2019. 10.1029/2019GL082252.
- [63] M. Sambridge, K. Gallagher, A. Jackson, and P. Rickwood. Trans-dimensional inverse problems, model comparison and the evidence. *Geophysical Journal International*, 167(2):528–542, 2006. 10.1111/j.1365-246X.2006.03155.x.
- [64] Masoumeh Dashti and Andrew M. Stuart. *The Bayesian Approach to Inverse Problems*, pages 311–428. Springer International Publishing, Cham, 2017. 978-3-319-12385-1.

- [65] William J. Titus, Sarah J. Titus, and Joshua R. Davis. A Bayesian approach to modeling 2D gravity data using polygons . *Geophysics*, 82:1942–2156, 2017. doi:10.1190/geo2016-0153.1.
- [66] Malcolm Sambridge, Thomas Bodin, Kerry Gallagher, and H Tkalčić. Transdimensional inference in the geosciences. *Philosophical Transactions of the Royal Society A: Mathematical, Physical and Engineering Sciences*, 371(1984):1–17, 2013. 10.1098/rsta.2011.0547.
- [67] Xiaolin Luo. Constraining the shape of a gravity anomalous body using reversible jump Markov chain Monte Carlo . *Geophysical Journal International*, 180:1067–1079, 2010. doi:10.1111/j.1365-246X.2009.04479.x.
- [68] L. Uieda, V. Barbosa, and C. Braitenberg. Tesseroids: Forward-modeling gravitational fields in spherical coordinates. *GEOPHYSICS*, pages F41–F48, July 2016. 10.1190/geo2015-0204.1.
- [69] T. M. Olugboji, V. Lekic, and W. McDonough. A statistical assessment of seismic models of the U.S. continental crust using Bayesian inversion of ambient noise surface wave dispersion data . *Tectonics*, 36(7):1232–1253, 2017. doi:10.1002/2017TC004468.
- [70] Alex S. Konopliv, Ryan S. Park, Dah-Ning Yuan, Sami W. Asmar, Michael M. Watkins, James G. Williams, Eugene Fahnestock, Gerhard Kruizinga, Mee-gyeong Paik, Dmitry Strelakov, Nate Harvey, David E. Smith, and Maria T. Zuber. The JPL lunar gravity field to spherical harmonic degree 660 from the GRAIL Primary Mission. *Journal of Geophysical Research: Planets*, 118(7):1415–1434, 2013. doi:10.1002/jgre.20097.
- [71] P. M. Muller and W. L. Sjogren. Mascons: Lunar Mass Concentrations. *Science*, 161(3842):680–684, 1968. doi:10.1126/science.161.3842.680.
- [72] Solomon Kullback. *Information Theory and Statistics*. Wiley, New York, 1959. ISBN:978-0486696843.
- [73] Mary Kathryn Cowles and Bradley P. Carlin. Markov Chain Monte Carlo Convergence Diagnostics: A Comparative Review. *Journal of the American Statistical Association*, 91(434):883–904, 1996. 10.1080/01621459.1996.10476956.
- [74] Stephen P. Brooks and Andrew Gelman. General methods for monitoring convergence of iterative simulations. *Journal of Computational and Graphical Statistics*, 7(4):434–455, 1998. 10.1080/10618600.1998.10474787.
- [75] Sandip Sinharay. Assessing convergence of the Markov Chain Monte Carlo algorithms: a review. *ETS Research Report Series*, 2003(1):i–52, 2003. 10.1002/j.2333-8504.2003.tb01899.x.

- [76] Nan Zhang, Shijie Zhong, Wei Leng, and Zheng-Xiang Li. A model for the evolution of the Earth's mantle structure since the Early Paleozoic. *Journal of Geophysical Research: Solid Earth*, 115(B6), 2018/09/23 2010. doi: 10.1029/2009JB006896.
- [77] Qing Liang, Chao Chen, and Yaoguo Li. 3-D inversion of gravity data in spherical coordinates with application to the GRAIL data. *Journal of Geophysical Research: Planets*, 119(6):1359–1373, 2014. 10.1002/2014JE004626.
- [78] Ian Garrick-Bethell, Francis Nimmo, and Mark A. Wieczorek. Structure and Formation of the Lunar Farside Highlands. *Science*, 330(6006):949–951, 2010. 10.1126/science.1193424.
- [79] D. E. Loper and C. L. Werner. On lunar asymmetries 1. Tilted convection and crustal asymmetry. *Journal of Geophysical Research: Planets*, 107(E6):13–1–13–7, 2002. <https://doi.org/10.1029/2000JE001441>.
- [80] John T. Wasson and Paul H. Warren. Contribution of the mantle to the lunar asymmetry. *Icarus*, 44(3):752 – 771, 1980. [https://doi.org/10.1016/0019-1035\(80\)90142-6](https://doi.org/10.1016/0019-1035(80)90142-6).
- [81] A. Khan, A. Pommier, G.A. Neumann, and K. Mosegaard. The lunar moho and the internal structure of the Moon: A geophysical perspective. *Tectonophysics*, 609:331 – 352, 2013. <https://doi.org/10.1016/j.tecto.2013.02.024>.
- [82] N. R. Goins, A. M. Dainty, and M. N. Toksz. Lunar seismology: The internal structure of the Moon. *Journal of Geophysical Research: Solid Earth*, 86(B6):5061–5074, 1981. 10.1029/JB086iB06p05061.
- [83] Yosio Nakamura, Gary V. Latham, and H. James Dorman. How we processed Apollo lunar seismic data. *Physics of the Earth and Planetary Interiors*, 21(2):218 – 224, 1980. [https://doi.org/10.1016/0031-9201\(80\)90071-0](https://doi.org/10.1016/0031-9201(80)90071-0).
- [84] Riccardo Borghi. On Newton's shell theorem. *European Journal of Physics*, 35(2):028003, jan 2014. 10.1088/0143-0807/35/2/028003.
- [85] G. E. Backus and J. F. Gilbert. Numerical Applications of a Formalism for Geophysical Inverse Problems. *Geophysical Journal of the Royal Astronomical Society*, 13:247–276, 1967. 10.1111/j.1365-246X.1967.tb02159.x.
- [86] Richard Saltus and Richard Blakely. Unique geologic insights from non-unique gravity and magnetic interpretation. *GSA TODAY*, 21:4–10, dec 2011. <https://doi.org/10.1130/G136A.1>.
- [87] Carlos Alberto Moreno Chaves and Naomi Ussami. Modeling 3-D density distribution in the mantle from inversion of geoid anomalies: Application to the Yellowstone Province. *Journal of Geophysical Research: Solid Earth*, 118(12):6328–6351, 2013. 10.1002/2013JB010168.

- [88] M. Herceg, I.M. Artemieva, and H. Thybo. Sensitivity analysis of crustal correction for calculation of lithospheric mantle density from gravity data. *Geophysical Journal International*, 204(2):687–696, 12 2015. 10.1093/gji/ggv431.
- [89] Yanick Ricard, Mark Richards, Carolina Lithgow-Bertelloni, and Yves Le Stunff. A geodynamic model of mantle density heterogeneity. *Journal of Geophysical Research: Solid Earth*, 98(B12):21895–21909, 1993. 10.1029/93JB02216.
- [90] Pejman Shamsipour, Denis Marcotte, and Michel Chouteau. 3D stochastic joint inversion of gravity and magnetic data. *Journal of Applied Geophysics*, 79:27 – 37, 2012. <https://doi.org/10.1016/j.jappgeo.2011.12.012>.
- [91] James G Williams, Slava G Turyshev, and Dale H Boggs. Lunar laser ranging tests of the equivalence principle. *Classical and Quantum Gravity*, 29(18):184004, aug 2012. 10.1088/0264-9381/29/18/184004.
- [92] W. Benz, W.L. Slattery, and A.G.W. Cameron. The origin of the moon and the single-impact hypothesis i. *Icarus*, 66(3):515 – 535, 1986. [https://doi.org/10.1016/0019-1035\(86\)90088-6](https://doi.org/10.1016/0019-1035(86)90088-6).
- [93] A. G. W. Cameron and W. R. Ward. The Origin of the Moon. In *Lunar and Planetary Science Conference*, volume 7 of *Lunar and Planetary Science Conference*, page 120, March 1976.
- [94] William K. Hartmann and Donald R. Davis. Satellite-sized planetesimals and lunar origin. *Icarus*, 24(4):504 – 515, 1975. [https://doi.org/10.1016/0019-1035\(75\)90070-6](https://doi.org/10.1016/0019-1035(75)90070-6).
- [95] Paul H. Warren and John T. Wasson. The origin of KREEP. *Reviews of Geophysics*, 17(1):73–88, 1979. <https://doi.org/10.1029/RG017i001p00073>.
- [96] Linda T. Elkins-Tanton, Seth Burgess, and Qing-Zhu Yin. The lunar magma ocean: Reconciling the solidification process with lunar petrology and geochronology. *Earth and Planetary Science Letters*, 304(3):326 – 336, 2011. <https://doi.org/10.1016/j.epsl.2011.02.004>.
- [97] William M. Kaula. Thermal evolution of Earth and Moon growing by planetesimal impacts. *Journal of Geophysical Research*, 84(B3):999–1008, 1979. 10.1029/jb084ib03p00999.
- [98] Ananya Mallik, Tariq Ejaz, Svyatoslav Shcheka, and Gordana Garapic. A petrologic study on the effect of mantle overturn: Implications for evolution of the lunar interior. *Geochimica et Cosmochimica Acta*, 250:238 – 250, 2019. <https://doi.org/10.1016/j.gca.2019.02.014>.

- [99] Y. Zhao, J. de Vries, A.P. van den Berg, M.H.G. Jacobs, and W. van Westrenen. The participation of ilmenite-bearing cumulates in lunar mantle overturn. *Earth and Planetary Science Letters*, 511:1 – 11, 2019. <https://doi.org/10.1016/j.epsl.2019.01.022>.
- [100] S.M. Brown and T.L. Grove. Origin of the Apollo 14, 15, and 17 yellow ultramafic glasses by mixing of deep cumulate remelts. *Geochimica et Cosmochimica Acta*, 171:201 – 215, 2015. <https://doi.org/10.1016/j.gca.2015.09.001>.
- [101] Aaron L. Scheinberg, Krista M. Soderlund, and Linda T. Elkins-Tanton. A basal magma ocean dynamo to explain the early lunar magnetic field. *Earth and Planetary Science Letters*, 492:144 – 151, 2018. <https://doi.org/10.1016/j.epsl.2018.04.015>.
- [102] Alexander J. Evans, Sonia M. Tikoo, and Jeffrey C. Andrews-Hanna. The case against an early lunar dynamo powered by core convection. *Geophysical Research Letters*, 45(1):98–107, 2018. <https://doi.org/10.1002/2017GL075441>.
- [103] A. J. Evans, M. T. Zuber, B. P. Weiss, and S. M. Tikoo. A wet, heterogeneous lunar interior: Lower mantle and core dynamo evolution. *Journal of Geophysical Research: Planets*, 119(5):1061–1077, 2014. <https://doi.org/10.1002/2013JE004494>.
- [104] Alberto E. Saal, Erik H. Hauri, Mauro L. Cascio, James A. Van Orman, Malcolm C. Rutherford, and Reid F Cooper. Volatile content of lunar volcanic glasses and the presence of water in the Moons interior. *Nature*, 454:192–195, 2008. <https://doi.org/10.1038/nature07047>.
- [105] Dave R. Stegman, A. Mark Jellinek, Stephen A. Zatman, John R. Baumgardner, and Mark A. Richards. An early lunar core dynamo driven by thermochemical mantle convection. *Nature*, 421:143–146, 2003. <https://doi.org/10.1038/nature01267>.
- [106] M. Le Bars, M. A. Wieczorek, . Karatekin, D. Cbron, and M. Laneuville. An impact-driven dynamo for the early Moon. *Nature*, 479:2015–2018, 2011. <https://doi.org/10.1038/nature10565>.
- [107] Christopher Stys and Mathieu Dumberry. A Past Lunar Dynamo Thermally Driven by the Precession of Its Inner Core. *Journal of Geophysical Research: Planets*, 125(7):e2020JE006396, 2020. <https://doi.org/10.1029/2020JE006396>.
- [108] Alberto Malinverno and Victoria A Briggs. Expanded uncertainty quantification in inverse problems: Hierarchical Bayes and empirical Bayes. *Geophysics*, 69(4):1005–1016, 2004. 10.1190/1.1778243.
- [109] Scott Burdick and Vedran Lekić. Velocity variations and uncertainty from transdimensional P-wave tomography of North America . *Geophysical Journal International*, 209(2), 2017. doi:10.1093/gji/ggx091.

- [110] Maxwell L. Rudolph, Vedran Lekić, and Carolina Lithgow-Bertelloni. Viscosity jump in Earth's mid-mantle. *Science*, 350(6266):1349–1352, 2015. 10.1126/science.aad1929.
- [111] Peter Puster and Thomas H. Jordan. How stratified is mantle convection? *Journal of Geophysical Research: Solid Earth*, 102(B4):7625–7646, 1997. 10.1029/96JB03625.
- [112] Thomas H. Jordan, Peter Puster, Gary A. Glatzmaier, and Paul J. Tackley. Comparisons Between Seismic Earth Structures and Mantle Flow Models Based on Radial Correlation Functions. *Science*, 261(5127):1427–1431, 1993. 10.1126/science.261.5127.1427.
- [113] S. Lloyd. Least squares quantization in PCM. *IEEE Transactions on Information Theory*, 28(2):129–137, 1982. 10.1109/TIT.1982.1056489.